UNIVERSITY OF TWENTE.

Master Thesis Mechanical Engineering

Towards the Characterisation and Development of Shape-Stabilised Phase Changing Materials for Tunable Material Properties

Author T.H. de Ruiter
University Supervisor Dr. D. Di Maio
External Supervisor E. Habtour

University of Twente,
Faculty of Engineering Technology,
Department Mechanics of Solids, Surfaces and Systems,
Research Chair of Dynamics Based Maintenance

02.12.2025

Backside of the title page

Summary

This study examines shape-stabilised phase changing materials (SSPCMs) for enabling temperature-dependent tuning of stiffness and damping. While literature and a reassessment of previous work showed a proof of concept between a decrease in stiffness due to chain mobility and an increase in stiffness due to thermal wax expansion, it did not provide sufficient accuracy. To obtain more reliable insight, in-house SSPCMs were designed, manufactured and characterized using a DMA machine. Small, well-controlled specimens allowed direct measurement of viscoelastic properties revealing clear tunable behaviour linked to the wax transition. The results demonstrate that SSPCM tunability becomes evident only when the wax content exceeds a certain threshold.

Contents

Nomenclature

α	Linear coefficient of thermal expansion	[ppm/K]
$\alpha(\omega)$	Receptance	[m/N]
α_p	Packing factor	[-]
α_v	Volumetric coefficient of thermal expansion	[ppm/K]
β	Wave number	[1/m]
δ	Phase angle	[°]
ϵ	Strain	[-]
ϵ_{dyn}	Dynamic strain amplitude	[-]
ϵ_{stat}	Static preload strain	[-]
η	Loss factor (structural damping)	[-]
γ^2	Coherence function	[-]
λ	Thermal conductivity	[W/(m K)]
ω	Angular frequency	[rad/s]
ω_n	Eigenfrequency (natural frequency)	[rad/s] or [Hz]
Φ	Mass normalized mode shape vector	[-]
Ψ	Unscaled mode shape vector	[-]
ρ	Density	[kg/m^3]
$\tan(\delta)$	Loss factor (viscoelastic)	[-]
ζ	Damping ratio	[-]
$A(\omega)$	Accelerance / Inertance	[m/Ns^2] or [1/kg]
a_T	Shift factor	[-]
A_{jk}	Modal constant / Residue	[-]
c	Viscous damping coefficient	[Ns/m]
C_1, C_2	WLF model constants	[-, K]
D	Hysteretic damping matrix	[N/m]
E	Young's modulus	[MPa]
E'	Storage modulus	[MPa]
E''	Loss modulus	[MPa]
E_a	Activation energy	[kJ/mol]
f	Frequency	[Hz]
$F(t)$	Excitation force vector	[N]
$H(\omega)$	Frequency Response Function (FRF)	[varies]

I	Second moment of area	[m^4]
K	Stiffness matrix	[N/m]
k	Stiffness	[N/m]
k_r	Modal stiffness	[N/m]
L	Length	[m]
M	Mass matrix	[kg]
m	Mass	[kg]
m_r	Modal mass	[kg]
M_w	Molar mass	[g/mol]
R	Universal gas constant	[J/(mol K)]
R^2	Coefficient of determination	[-]
T	Temperature	[°C]
T_g	Glass transition temperature	[°C]
T_{ref}	Reference temperature	[°C]
V_w	van der Waals volume	[cm^3/mol]
v_w	Specific van der Waals volume	[cm^3/g]
V_{oc}	Occupied volume	[cm^3/g]
V_{sp}	Specific volume	[cm^3/g]
X	Displacement amplitude vector	[m]
$x(t)$	Displacement vector (time domain)	[m]
$Y(\omega)$	Mobility	[m/Ns]
Z	Impedance matrix	[Ns/m]

List of Abbreviations

CFS	Closed-Form Shifting
CTE	Coefficient of Thermal Expansion
DAQ	Data Acquisition
DMA	Dynamic Mechanical Analysis
EMA	Experimental Modal Analysis
FBD	Free Body Diagram
FFT	Fast Fourier Transform
FRF	Frequency Response Function
LVE	Linear Viscoelastic
MDOF	Multi Degree of Freedom
PCMs	Phase Changing Materials
RMSE	Root Mean Square Error
SDOF	Single Degree of Freedom
SSPCMs	Shape-Stabilised Phase Changing Materials
TMA	Thermomechanical Analysis
TTSP	Time–Temperature Superposition Principle
WLF	Williams–Landel–Ferry

1 Introduction

In the aerospace industry, there is a continuous drive to develop innovative materials that are lighter, stronger and more cost-efficient. In the current design process, the evaluation of a structure's dynamic properties is typically conducted at the final stage. As a result, implementing design changes at that point often becomes impractical and costly.

Shape-Stabilised Phase Changing Materials (SSPCMs) offer a potential solution. These materials can transition between phases, for example from liquid to gas or from solid to liquid, when exposed to external stimuli such as temperature or pressure. The phase transition alters the material properties, which provides a unique advantage: instead of being restricted to one material with fixed characteristics, the properties can be adapted after manufacturing. The key advantage is that any material parameter, within a specified range, can be tailored to its application. This makes the design process easier and it can be implemented in many applications.

An example of a potential implementation is in aircraft wings or wind turbine blades to prevent flutter. Flutter is a dynamic instability of a structure in fluid flow. It occurs when the aerodynamic forces exerted on a structure result in a positive feedback loop for the deflection of the wing or blade, which in turn will excite the eigenfrequency of the wing [17].

An example of flutter in an aircraft wing is displayed in Figure 1.1. This figure shows two coupled mode shapes, the bending and torsion mode. At low speeds flutter is not a problem, as the eigenfrequency of two different modes are far away from each other. However, at higher speeds, the aerodynamic forces change, modifying the effective stiffness, damping and the eigenfrequency of the wing. As a consequence, when two different eigenfrequencies move close together, they become aerodynamically coupled. The result is that beyond a certain speed, these modes start to vibrate simultaneously and the system becomes self-excited and oscillation amplitudes grow rapidly. An increased amplitude or in other words a large displacement is typically undesired since it reduces the lifetime of the wing or blade.

Figure 1.1: *A schematic representation of aircraft wing flutter [45]*

There are two possible solutions to counteract uncontrolled vibrations, the first one is to increase the stiffness. This results in a greater separation of the eigenfrequencies of the wing. This is advantageous because the chance of two eigenfrequency coinciding, resulting in flutter, is reduced. To achieve a stiffer wing the most simple option is to add more material to the wing but this increases weight and thus reduces efficiency. However, a stiffer wing also has some drawbacks as it increases high-cycle fatigue. Additionally, an excessively stiff wing reduces the aircraft capability of natural flexing, which is needed to improve passenger comfort by reducing the vibrations induced by turbulence.

The second solution is to change the damping. The damping is defined as the sum of the contribution of the positive damping ratio due to the damping of the material and the contribution of the negative damping ratio caused by the aerodynamic forces. This means the net damping can have three values. First, positive net damping, this is the controlled situation, where the oscillations in the wing the damp out and do not cause any problems. Second, zero net damping, the vibrations of the structure stay harmonic and do not damp out. In practice this case rarely happens as the net damping changes constantly. Lastly, the net damping turns negative. The vibrations grow unbounded and the wing starts to oscillate. The result is damaging or even

breakage of the wing or blade. This situation arises because, at higher airspeeds, aerodynamic forces increase quadratically with velocity. When this growth exceeds the structural damping capacity, the total damping can no longer remain positive, meaning the structural damping ratio is insufficient to counter the aerodynamic contribution [46]. To resolve this issue, the damping could be increased, but this introduces several drawbacks. The most substantial one is that excessive damping reduces the responsiveness of control surfaces. This weakens the aircraft's ability to perform rapid and precise manoeuvres, which may be required in fighter aircraft. Moreover, high damping disrupts the balance by absorbing energy that would otherwise facilitate the necessary deformations for optimal lift and drag distribution [91].

This reveals the central challenge: flutter prevention requires precise control of both stiffness and damping, yet traditional materials offer no means of tuning these properties during operation. SSPCMs, however, introduce that capability. By using temperature as a trigger, SSPCMs can shift from low- to high-damping behaviour, allowing the material to act as a temperature-dependent viscoelastic damper. Such tunability offers three major benefits: design freedom after fabrication, structural optimisation for varying load cases, and reduced reliance on conservative worst-case design assumptions.

This establishes the basis for the objective of the present work. Although tuning stiffness and damping simultaneously is challenging due to competing physical mechanisms, SSPCMs provide a pathway to achieve such behaviour. *The goal of this study is therefore, to characterize, design and develop state-of-the-art SSPCMs capable of adjusting stiffness and damping through controlled temperature changes*. This is achieved by examining different silicone rubber–wax compositions and analysing how their combined thermomechanical behaviour enables controlled tuning.

To achieve this goal, the report is structured into five main sections. Section 2 presents the literature study, which examines in detail the fundamental behaviour of SSPCMs. It discusses the material properties of the constituents of SSPCM: silicone rubber and paraffin wax in Sections 2.1 and 2.2. It will identify the key factors that govern the thermomechanical response and integrates this knowledge to establish a solid foundation for understanding SSPCMs as a combined system from a material science point of view. It will also provide the necessary background information about polymers in Section 2.3 and how the viscoelastic material properties can be assessed using a dynamic mechanical analyser (DMA) machine in Section 2.4. The chapter concludes with a general summary of SSPCMs in Section 2.5.

Section 3 provides the fundamental principles of modal analysis. Section 3.1 first examines the concept of damping. This is followed by a more sophisticated analysis method for determining the modal properties of MDOF systems. The discussion begins with an undamped free vibration SDOF model in Section 3.2 and progresses to a forced vibration MDOF model with hysteretic damping in Section 3.3. These models are subsequently applied in the Experimental Modal Analysis described in Section 3.4, after which the modal parameters are determined using the methods outlined in Section 3.5.

This is followed by Section 4, which applies the previously established knowledge to perform a theoretical review of the SSPCMs developed by Flint in Section 4.1. Next, these same SSPCMs are experimentally evaluated using a modal shaker and hammer test, the corresponding stiffness and damping properties are reported in Section 4.2 focusing more on a structural dynamics perspective.

Section 5 combines the obtained knowledge from the theoretical and experimental test of the SSPCMs to design, develop and manufacture in house SSPCMs with the capability of tuning the stiffness and damping. The materials used in SSPCMs will be reconsidered in Sections 5.1 and 5.2. The newly made SSPCMs will be manufactured in Section 5.3 and tested using a DMA machine in Section 5.4. In Section 5.5 the results of these in house samples are evaluated and concluded in Section 5.6.

Finally, Section 6 presents the overall conclusions drawn from this work. It also outlines several directions for future research that could further advance the understanding and development of the tunability of SSPCMs.

2 Literature study

SSPCMs are hybrid materials composed of two constituents: a matrix material and a phase-changing filler. They can be seen as composite materials in which the matrix provides structural support and keeps the filler contained, even when the filler becomes liquid at higher temperatures. Typical matrix materials include polyurethane, polypropylene, epoxy and silicone rubber. The filler commonly consists of phase changing materials (PCMs) such as paraffin wax, which undergoes significant volumetric expansion during melting. It is essential to first examine the properties of the individual constituents, before the overall behaviour of SSPCMs can be understood. Therefore, the literature study is divided into five sections. Starting with Section 2.1, which discusses the classification and composition of PCMs, followed by their key material properties. Section 2.2 presents the same structure for the matrix material. Section 2.3 then provides an extensive overview of how temperature, frequency, strain and preload affect the viscoelastic behaviour of polymers. Section 2.4 explains the working principles of DMA testing and lastly, Section 2.5 presents state of the art research on the material properties of SSPCMs.

2.1 Phase Changing Materials

PCMs are compounds that release or absorb a large amount of heat during a phase transition. This latent heat is stored within the material and can be used for temperature regulation, since the temperature remains nearly constant during the phase transition. Furthermore, PCMs such as paraffin waxes are chemically inert, non-corrosive and are safe to handle, which makes them suitable for both research and industrial applications.

2.1.1 Classification

Figure 2.1 shows the main categories of PCMs: organic, eutectic and inorganic. Within the organic group, non-paraffin PCMs such as fatty acids and glycols are excluded from the research because they are flammable, have low thermal conductivity, are more expensive than paraffins and may be mildly corrosive [97]. Organic paraffins are included due to their suitable melting range, high volumetric expansion and low cost. On the inorganic side, only metallic PCMs are considered. Salt hydrates are excluded because they suffer from phase separation, supercooling and poor long-term stability [97]. Eutectic PCMs are shown for completeness but are not investigated further.

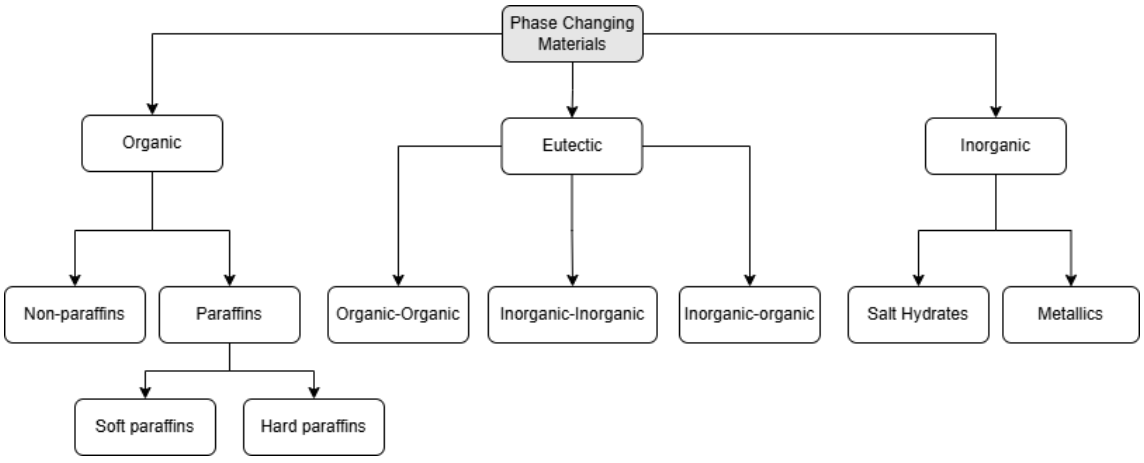

Figure 2.1: *Classification of PCMs*

2.1.2 Composition

Paraffin compounds are manufactured from petroleum. This is refined and de-waxed and the resulting product is paraffin wax. Paraffin waxes are mixtures of saturated hydrocarbons with typical chain lengths ranging from 20 to 50 carbon atoms. Their molecular structure is dominated by carbon carbon backbones bond with methyl groups at both ends. Although they are primarily composed of linear n-alkanes, they also contain iso-paraffins, cycloparaffins and small amounts of benzene rings. In general, they follow the chemical formula C_nH_{2n+2}, where n denotes the number of carbon atoms in the chain. Paraffin waxes are often categorised by chain length, with soft waxes containing approximately 20 to 30 carbon atoms and hard waxes containing roughly 30 to 40 carbon atoms. The distribution of chain lengths, together with the presence of linear, branched and cyclic hydrocarbons, ultimately determines the final material properties. Hard waxes typically contain very little oil and are composed mainly of linear paraffin chains. These chains can pack efficiently, creating a dense crystalline structure. This dense packing increases the cumulative van der Waals forces, which contributes to a harder material with a higher melting area. The longer the carbon chains the stronger the intermolecular forces and as a result, hard waxes display higher crystallinity and stiffness. In contrast, soft waxes contain more oil and a larger proportion of iso-paraffins, cycloparaffins and benzene rings. These irregular and branched structures prevent efficient packing, producing a less dense and more amorphous structure with a lower melting point.

2.1.3 Applications

Typical applications of general PCMs include their use in buildings to passively manage indoor temperatures in a more sustainable way, eliminating the need for active heating or cooling [103]. They are also commonly applied in heat sinks, solar energy storage systems, and even in textiles to create thermally adaptive clothing [80]. In most of these applications the intrinsic property of high coefficient of thermal expansion (CTE) in wax is undesirable. In this research, however, this property is deliberately exploited to enhance make the tunability of the material properties possible. Typical applications of hard paraffin waxes include coatings, adhesives and, most notably, candles. Soft waxes, on the other hand, are more commonly used in cosmetics and as lubricants [79].

2.1.4 Melting area

The melting area of soft and hard paraffins waxes depend on the exact composition of the wax. Waxes always contain different length of hydrocarbons each with a different melting point, therefore, it is more common to talk about a melting area [2]. For pure hydrocarbons each increase in carbon atom adds around 3 °C to the melting temperature, starting from 17 carbon atoms at 22 °C up to 50 carbon atoms and 120 °C [114].

2.1.5 Thermal conductivity

Thermal conductivity, denoted by λ, expresses how much heat per second flows through a material per unit area and per unit temperature gradient, meaning that materials with a high value conduct heat efficiently, whereas those with a low value do not and act as insulators. Paraffin waxes fall into the latter category. They have a very low thermal conductivity of only 0.2-0.4 W/(mK) [92], which is roughly a factor of 1000 lower than that of standard aluminium. A common approach to increases the thermal conductivity often necessitates the addition of conductive fillers like graphite powder. This enhances the thermal conductivity by a factor 10 [12, 118].

Several studies have shown that the thermal conductivity of paraffin waxes increase at the onset of melting area and reaches its maximum near the melting point of the most dominant hydrocarbon. Once the phase transition is complete and the material is fully liquefied, the thermal conductivity decreases again to its initial value [58, 103].

Most research do not specify the difference between soft and hard wax therefore, it is assumed that the thermal conductivity is the same for both. However, in reality, paraffins with a

more branched structure (like soft wax) should show a reduction in the thermal conductivity in the solid phase as branching hinders neat alignment and crystallization which enhance thermal conductivity [15]. Therefore, it is expected that in practice hard paraffin wax has a higher thermal conductivity than soft paraffin wax.

2.1.6 Coefficient of thermal expansion

The coefficient of thermal expansion, denoted by α for linear CTE and α_v for volumetric CTE, is an important property as it will be used as the primary mechanism to change the material properties. It says something about how much a material expands per unit temperature. Paraffins undergo large volume expansion during the solid-to-liquid transition. For a hydrocarbon with a chain length of 24 carbon atoms, this expansion can be up to 22.9 % over a 50 °C temperature range (α_v = 4580 ppm/K) [116]. However, most paraffins are mixtures of different length of hydrocarbons. Research showed that high purity of the paraffin wax is important to achieve high CTE. Just as the thermal conductivity the maximum thermal expansion occurs in the melting area. Paraffins waxes are a mixture of different hydrocarbons, so the melting area is very broad and as a result the CTE is lower when compared with pure hydrocarbons [108].

A pivot in most reports is that only a single CTE value is provided, even though waxes exhibit strong temperature dependence and ideally a full CTE curve over the relevant temperature range should be reported. An schematic of such a curve is presented in Figure 2.2. It shows that when the wax is in solid phase the volume change is little however, when the temperature approaches the melting area the volume change increases significantly. The slope of the temperature-volumetric expansion graph is directly related to the CTE. A steep slope indicates a great volume change so an increase CTE. The highest CTE is thus present in the melting range.

Several studies have reported volumetric CTE values for paraffin waxes ranging from 400 to 2000 ppm/K [58, 71, 108], which is one to two orders of magnitude higher than typical values for metals [110]. Manufacturers also report volume changes of approximately 10 to 15 percent during melting [37, 38, 39, 71].

Lastly, it is also important to characterize the CTE. Several techniques can be used to determine the CTE, including dilatometry, thermo-mechanical analysis (TMA), X-ray diffraction, laser interferometry and digital image correlation (DIC). For PCMs, the most common approaches are TMA and dilatometry, the latter often relying on using a pycnometer to determine density changes [58, 71].

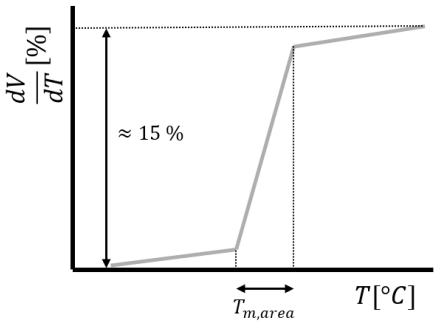

Figure 2.2: *Typical temperature-volumetric expansion curve of paraffin wax*

2.1.7 Limitations

Paraffin waxes also present certain limitations. They are flammable, meaning that any contact with flames must be avoided. In addition, hard paraffin waxes are often brittle at room temperature and should therefore be handled with care. Next, reaching temperature above 200 °C, decomposes the wax. This makes the phase transition process irreversible and the PCM unusable [104, 119]. The final element that should be assessed is the solid to liquid phase change. When

the wax is tested above the melting temperature it turns liquid and will lose its shape and, if not enclosed, it will leak. A possible solution is to combine the wax with a second material called the matrix. This material will act as encapsulation and keeps the wax contained and will be discussed in the next section.

2.2 Matrix materials

Several materials can serve as a matrix for PCMs. Although alternatives such as polyurethane and epoxy are discussed in Sections 5.1.2 and 5.1.1, silicone rubber is discussed in this section. It focuses on silicone rubber by outlining its composition and common applications, followed by the key material properties relevant to SSPCMs.

2.2.1 Composition

Silicone rubber is a synthetic viscoelastic elastomer compound composed of a main backbone of Si-O bonds connected by organic side groups such as methyl ($-CH_3$) or vinyl ($= CH_2$). Therefore, Silicone rubbers are also commonly denoted as polysiloxane. Most silicone rubbers consist of two components. The first component is the base polymer and consists of silicone with methyl en vinyl side groups on each and an additional catalyst. The second component is the crossing agent and contains silicone hydride ($Si - H$). To create silicone rubber, the two components are mixed and then the catalysis or cure starts. The silicone rubbers used within this research are all platinum-cured compounds. This is a basic addition reaction where a vinyl group reacts with the hydrogen atom in the curing agent in the presence of a platinum catalyst to form a cross-linked 3D network. The formation of this network takes place under ambient conditions because the silicone rubber is a room-temperature-vulcanizing (RTV) system. Its vulcanization is irreversible, meaning the material cannot be reshaped once cured, which classifies it as a thermoset [5, 7]. This provides excellent thermal stability but limits recyclability.

2.2.2 Applications

Silicone rubber is used in a wide variety of applications. From automotive applications utilized for gaskets and seals to the food industry where it is used for flexible baking ware and storage containers due to its high temperature resistance and flexibility. It is also commonly used in medical industry to create implants or prosthetics [115].

2.2.3 Thermal conductivity

The thermal conductivity of silicone rubber is comparable to that of paraffin wax. Silicone rubbers act as insulators, with typical values ranging from approximately 0.2 to 0.8 W/(mK) [5, 54, 99, 109]. Although this can be improved by incorporating thermally conductive fillers such as aluminium oxide or boron nitride [57], doing so increases the complexity of the SSPCM system. To maintain simplicity, fillers are therefore, not considered further in this work. Unlike paraffin wax, the thermal conductivity of silicone rubber shows only slight variation with temperature and remains roughly constant throughout the rubbery region [62].

2.2.4 Coefficient of thermal expansion

The Free Volume Fraction, or Fractional Free Volume (FFV), plays a central role in determining the CTE. It is a dimensionless parameter that indicates how much of the polymer's volume is not occupied by material and therefore reflects how much "empty" space is present. This concept forms the basis for several important material relations. A more detailed explanation of FFV is provided in Section 2.5.4.

The CTE of polymers can be understood as the combined result of two molecular mechanisms influencing the FFV: a vibrational contribution and a configurational contribution. Below the glass transition temperature, thermal expansion is governed almost entirely by anharmonic

molecular vibrations. In this regime, the free volume remains constant because polymer mobility is restricted. These local vibrations create only small changes in intermolecular spacing and therefore, contribute minimally to the CTE. Above the glass transition temperature, the situation changes. While the vibrational contribution remains approximately constant, the configurational contribution becomes active [69]. In this state, polymer chains have sufficient mobility to shift into new configurations which generate additional free volume. This configurational mechanism is the dominant driver of thermal expansion in the rubbery state and is typically two to three times larger than the vibrational contribution [69]. The combined effect can be expressed by Equation 2.1, where the configurational term is zero when the temperature is below the glass transition temperature.

Reported CTE values in the rubbery state ($\alpha_{T>T_g}$)) are widely available. For example, Adams et al. [3] measured a linear CTE of approximately 250 ppm/K for DC745 silicone rubber between -30 °C and 60 °C using a TMA machine. Other studies state similar values in the range of 200 to 400 ppm/K [5, 6, 61, 63, 93]

$$\alpha_{T>T_g} = \alpha_{vibrational} + \alpha_{configurational} \approx 3\alpha_{T<T_g} \tag{2.1}$$

2.2.5 Castability

Soft silicone rubbers are well known for their ability to accurately replicate the shape of the mould in which they are cast. This property makes it easy to produce a wide variety of geometries using silicone rubber materials.

2.3 Influence of different factors on the viscoelastic properties of polymers

To tune the dynamic properties of an SSPCM, it is essential to identify which parameters most strongly influence the stiffness and damping behaviour. These parameters can be grouped into factors that modify the polymers composition at microscopic (compositional) level and those that affect the behaviour at macroscopic (operational) level. Microscopic factors include cross-link density, molecular weight, the ratio between base polymer and curing agent and the presence or number of fillers. Macroscopic factors include the temperature, excitation frequency, strain amplitude and the static or dynamic (pre)load. Since this study adopts a macroscopic perspective, only the influence of these operational parameters will be examined in the sections below. In polymer science the stiffness and damping are not often used to describe the material behaviour, as a results three new material properties are introduced: storage modulus, loss modulus and loss factor.

The storage modulus, denoted by E', is the elastic part of the materials response, it indicates how much of the stored energy is returned during a cycle of deformation. It is a measure for the stiffness of the material. A high storage modulus indicates a high stiffness and means that the material acts more as a solid.

The loss modulus, denoted by E'', is the viscous part of the material response. It says something about how much energy dissipated during once cycle of deformation. A high loss modulus indicates a greater capacity for energy dissipation.

The loss factor, denoted by $\tan(\delta)$, describes the damping behaviour of a polymer and is defined as the ratio of the loss modulus to the storage modulus, as shown in Equation 2.2. A high loss factor indicates strong damping capacity, whereas a low value reflects limited damping.

$$\tan(\delta) = \frac{E''}{E'} \tag{2.2}$$

2.3.1 Temperature dependence

Temperature is arguably the most dominant parameter influencing the damping properties of viscoelastic materials. The viscoelastic behaviour is not a simple linear function of temperature but instead is characterized by the behaviour of different regions which are connected to molecular mobility. The influence of temperature in different regions on the storage modulus, loss modulus and loss factor is discussed using Figure 2.3. Starting at the glassy region and ending beyond the terminal zone.

Silicone rubber does not exhibit a melting temperature like semi-crystalline paraffin wax because it is an amorphous polymer. These types of polymers only contain a glass transition temperature. This temperature marks the range where the polymer transition from rigid, hard, glassy state to a soft, elastic rubbery state. This is represented by a peak in the viscoelastic properties in the glass transition region in Figure 2.3.

In the region below the glass transition temperature, molecular mobility is highly restricted and the polymer chains are effectively frozen in place. As a result, the material resists deformation well, which leads to a high stiffness and therefore, a high storage modulus. The loss modulus is low in this range but increases slightly as the temperature approaches T_g, mainly due to secondary relaxation mechanisms where localized motions of side groups become active and can dissipate energy. The loss factor remains very low because the storage modulus is dominant over the loss modulus, yet it increases slightly as these secondary relaxations introduce additional energy dissipation increasing the loss modulus [8]. This is all shown in the glassy region of Figure 2.3.

As the material enters the glass transition region, the α-relaxation is activated. When the temperature increases, the polymer backbone gains mobility and segmental motion begins, leading to a gradual softening of the material. The glass transition does not occur at a single temperature but over a range in which molecular mobility progressively increases. This allows the chains to rearrange more easily, causing the storage modulus to decrease. The α-relaxation also increases internal friction, which produces a peak in the loss modulus. Immediately after, at higher temperatures, the mobility of the polymer chains become fully activated, allowing them to respond rapidly to deformation. This dissipates less energy and reduce the modulus because the chains can move past each other with greater ease. The loss factor reaches its maximum because the storage modulus decreases more rapidly than the loss modulus in this region. For applications where maximum damping is desired, the material should be tested in the vicinity of the glass transition temperature. For silicone rubber, this is between approximately -120 and -100 °C [56, 81, 113].

The rubber plateau is the third region in Figure 2.3. Above T_g, the material is very soft and flexible as the molecular chains gained large scale mobility. However, the material is still able to provide elasticity due to the formed cross-links and chain entanglements, those are weaker than molecular restriction in the previous two region but can still provide some resistance against deformation resulting in a moderate storage modulus. The loss modulus remains constant throughout this region, because of the chain mobility. The loss factor decreases drastically after T_g and stabilizes on a low constant value. The applicability to silicone rubber is as follows. Having a T_g

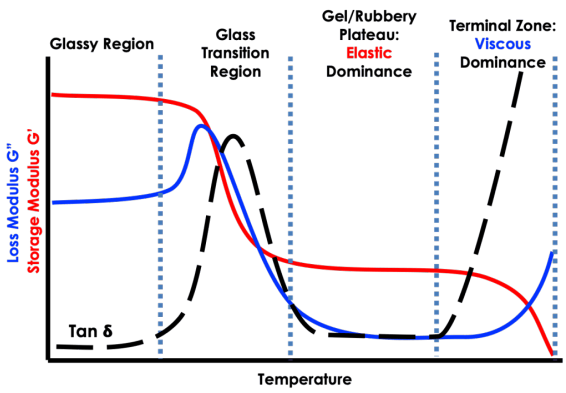

Figure 2.3: *Temperature influence of an amorphous polymer on viscoelastic properties [59]*

between -120 and -50 °C and usage scenario between -25 and 60 °C, means the silicone rubber is used in the rubbery plateau region, where the damping capacity of the polymer is significantly lower than at the glass transition temperature. Typical values between 0.05 to 0.4 are encountered for room temperature [18, 41, 42]

The terminal zone marks the transition from a rubbery, elastic response to a viscous state. In this region, the molecular chains have sufficient mobility to flow freely, the only force keeping the polymer together, are the entanglements. As a result, the storage modulus drops to nearly zero. The behaviour becomes dominated by viscous flow, allowing the material to dissipate large amounts of energy, which is reflected by an increase in the loss modulus. Due to a decrease in storage modulus and an increases in loss modulus, the loss factor rises, as can be seen in Figure 2.3. Since the polymer behaves essentially as a liquid, this region is avoided in engineering applications that require structural integrity [41]. For silicone rubbers, the terminal zone typically occurs around 200–230 °C [101, 102].

At even higher temperatures the material enters the thermal degradation zone, where chemical bonds begin to break. This process is irreversible and leads to a loss of all functional properties. For paraffin wax, degradation typically starts around 200–250 °C [94], while silicone rubbers degrade between roughly 250-400 °C [113]. These temperatures lie far beyond the range shown in Figure 2.3.

2.3.2 Frequency dependence

The viscoelastic properties of silicone rubbers are also highly dependent on the frequency of the applied load. This dependency is due to the relaxation time of the polymer chains. At low frequencies, the polymer chains have the time to adapt to the applied deformation. The chains can easily rearrange and flow past each another, resulting in viscous like behaviour. When the frequency is increased the chains do not have sufficient time to rearrange and will act more like springs resulting in a stiffer response.

When the loading frequency increases, both the storage modulus and the loss modulus rise as well. Because these two quantities increase simultaneously, it is not known beforehand whether the loss factor will increase or decrease. What is certain however, is that the loss factor eventually reaches a maximum. This peak occurs when the excitation frequency matches the characteristic frequency of the polymer's primary relaxation process, the α-relaxation, at which the material dissipates the greatest amount of energy.

For silicone rubber at room temperature, the situation is different. Because the material is far above its T_g, the α-relaxation cannot be reached within accessible frequency ranges. According to the Time-Temperature Superposition Principle (TTSP), which is explained in more detail in Section 2.4.2, the large temperature distance above T_g must be compensated by an enormous upward shift in frequency. As a result, the α-relaxation peak for silicone rubber lies at extremely high frequencies, far beyond the range of standard testing equipment and practical applications [68].

2.3.3 Strain amplitude dependence

Material behaviour is often assumed to be linear viscoelastic, meaning that stress and strain are proportional and independent of the strain amplitude. In reality, this linearity only holds for small deformations. As the applied strain increases, the material response becomes non-linear. The strain range in which the material still behaves linearly is known as the linear viscoelastic (LVE) regime. Identifying this regime is essential to test the material properties. To find this region a DMA test is executed where the temperature and frequency are kept constant and the dynamic strain amplitude is changed in a logarithmic way from very low dynamic strain amplitude (0.001 %) to high dynamic strain amplitude (100 %). The next step is to plot the storage against the dynamic strain, the point where the modulus deviation is around 5 % of the initial value, is defined as the critical dynamic strain and all measurement hereafter must be performed below this critical strain to stay in the LVE regime [51].

2.3.4 Static and dynamic preload dependence

The next parameter influencing the viscoelastic response is the static preload. The primary purpose of this preload is to prevent slippage during testing and to maintain a consistent geometry, thereby ensuring that the specimen initial length remains constant throughout the measurement. Applying a static preload to an elastomer deforms its polymer network. If the preload is small, the effect is negligible, which is desirable. However, when the preload is large, it can change the molecular orientation and increase the stiffness of the material [78]. A study of Cortazar showed that the storage modulus is bigger for lower preloads in the glassy region, while in the rubbery region the opposite is true. A frequency sweep test in the rubbery region was performed and showed for different prestress levels, ranging from 2 to 12 N, an increase in storage modulus of 58 %, while the influence on the loss factor was negligible. The work also revealed that T_g increases, with increasing preload [25].

The last parameter is closely related to the static preload and is the dynamic preload. This is the oscillatory component of the total applied load. Mathematically they are related as shown in Equation 2.3. This equation reveals that the static preload must always be greater than the dynamic preload to ensure that sample is always in tension. If this is not the case the total load would become negative and the sample would go from tension to compression.

The final parameter is the dynamic preload, which represents the oscillatory part of the total applied load and is directly related to the static preload, as shown in Equation 2.3. This relationship shows that the static preload must always exceed the dynamic preload to keep the sample in tension. Otherwise, the total load would become negative and the measurement invalid.

$$\epsilon(t) = \epsilon_{static} + \epsilon_{dynamic}\, sin(\omega t) \tag{2.3}$$

2.4 Dynamic Mechanical Analysis

The viscoelastic material properties described above can be measured using a Dynamic Mechanical Analysis (DMA) machine. This section introduces what a DMA machine is and the basic working principles. When the viscoelastic materials are determined the TTSP is discussed and the shift factors to construct the master curves.

2.4.1 Working Principle

DMA is a technique to characterise the viscoelastic properties of a polymer or rubber compound. The working principle is that a sinusoidal stress or strain is applied to the material. The response of the material is measured and tells something about the material properties. When the material is fully elastic the response will be in phase with excitation, indicating the stress and strain are proportional by the Young's modulus. At the other end of the spectrum, the material is completely viscous and the phase lags exactly 90° behind the excitation, meaning that the stress and viscosity are proportional by the strain rate. For viscoelastic materials the response is a combination of the elastic and viscous behaviour, resulting in a phase angle between 0 and 90°. Using this this the storage modulus, loss modulus and loss factor can be determined [52].

The DMA machine used in this research is shown in Figure 2.4b and a simplified schematic of its internal components is presented in Figure 2.4a. It shows that the sample is driven by a linear motor that imposes a small oscillatory deformation. When the furnace heats up, the sample expands. This is directly linked to the displacement of the probe which is recorded by a Linear Variable Differential Transformer (LVDT). When the measured displacement is compared to the applied force of the linear motor the phase lag can be determined, from this relationship the storage modulus, loss modulus and loss factor are computed.

In a stress-controlled measurement the force is controlled. This approach is often used for stiff materials and in creep or relaxation tests. When the DMA tries to maintain the target force, it keeps applying the force even though the material can no longer sustain it. This can cause the strain to grow rapidly resulting in excessive deformation. To avoid this, a strain-controlled measurement is introduced, where the deformation is controlled. Silicone rubber is a very soft

material, Since silicone rubber is very soft, strain-controlled testing is the appropriate choice [84].

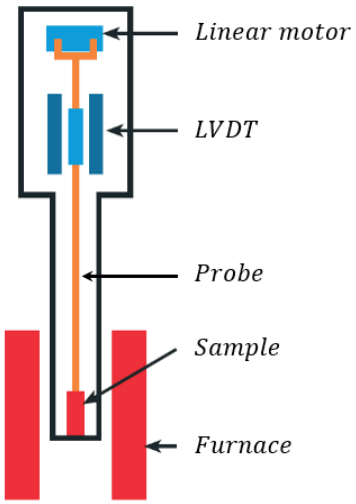

(a) *Schematic representation of a DMA machine*

(b) *The DMA 523 Eplexor (middle), the liquid nitrogen tank (left) and the computer (right)*

Figure 2.4: *Overview of the DMA setup and instrumentation*

2.4.2 Time-Temperature Superposition principle

The TTSP states that the influence of frequency and temperature on the viscoelastic properties of a polymer are equivalent. This implies that increasing the temperature has the same effect as decreasing the frequency and vice versa. This equivalence allows data taken at different isotherms to be horizontally shifted along the frequency axis until the curves overlap. These shifts create a single, continuous master curve, which shows the viscoelastic properties over several decades of frequency. A schematic master curve is shown by the bolt line T_0, in Figure 2.5a.

However, there are some limitations to when the TTSP holds. First the material must remain intact and must not change morphology. This means no additional molecular transitions such as crystallization, melting or phase change can occur. Next, it is important that each isotherm covers the same range. Also, the material should be excited within the LVE region. However, The most important one is that the material must be thermorheological simple, this means that a measurement can only be shifted horizontally along the frequency axis without altering the shape of the isotherm. To achieve this an isothermal curve is moved an arbitrary amount determined by the shift factor. Mathematically this is shown in Equation 2.4, where the viscoelastic properties (Υ) are a function of f and f_{ref}, the measured frequency range and scaled frequency, T and T_{ref} the environmental temperature and reference temperature and lastly the horizontal shift factor a_T [68]. The shape of the master curve is governed by these shift factors, which are examined further in the next section.

$$\Upsilon(f,T) = \Upsilon\left(\frac{f_{ref}}{a_T}, T_{ref}\right) \tag{2.4}$$

2.4.3 Shift factors

The shift factor is the amount of translation needed to transform the isothermal curve at temperature T to the reference temperature T_{ref}. There are several ways to calculate the shift factors, the easiest one is to manually adjust all the shift factors such that the data of a isotherm corresponds with the reference isotherm. This is very tedious and operator dependent process. An improved method is to use the Root Mean Square error (RMSE) method which minimizes the horizontal distance between adjacent isotherms by means of extrapolation of the current curve. A drawback

of this method, is that the extrapolation method is highly sensitive to the input data before and to the type of extrapolation.

The final method that resolves this limitation is the closed form shifting (CFS) method, which provides a deterministic and fully automated procedure for computing the shift factors. The method operates by minimizing the area between two isothermal measurements. Any pair of isotherms contains a region where their modulus values overlap, known as the overlapping window and is illustrated in Figure2.5b. The objective is to horizontally translate the isotherm at temperature T_1 onto the reference isotherm at T_0 such that the area enclosed within this overlapping window becomes zero. The x-axis is logarithmic, this means that the found shift factors for minimizing the area are linear in $log(a_T)$. This linearity enables the derivation of an explicit closed form expression, removing operator-dependent bias and eliminating the need for complex interpolation functions [68]. Both the RMSE method and the CFS method are used in this work to determine the shift factors for each isotherm and use these to construct the master curves.

A different way to interpret the shift factors is to examine the trend as a function of temperature. Several models can describe this behaviour, including the Williams–Landel–Ferry (WLF) model, the Arrhenius model, the Vogel–Fulcher model and the Doolittle model [13]. Each model introduces its own correction terms and assumptions, making it applicable to specific temperature regions of the polymer. Despite these differences, they all originate from the Arrhenius relation. In this work, only the WLF and Arrhenius models are considered.

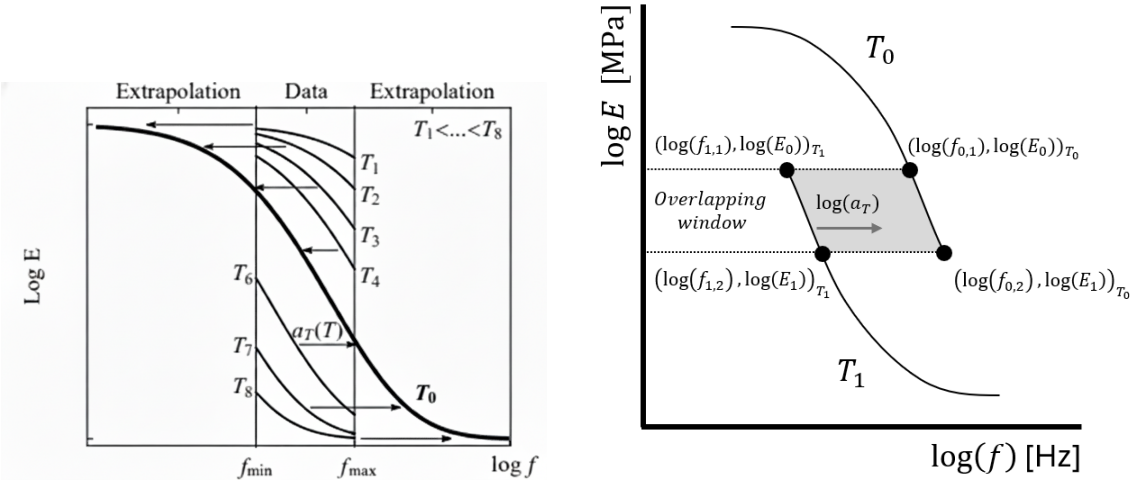

(a) *A simplified representation of the TTSP [9] (modified)*

(b) *Schematic explanation of the CFS algorithm*

Figure 2.5: *Overview of the TTSP and schematic of the CFS method*

Williams-Landel-Ferry model

The WLF model is an empirical relation based on free-volume theory, which states that the FFV increases linearly with temperature above T_g. Below T_g however, the free volume is essentially frozen, its contribution to segmental mobility becomes negligible and it remains constant with temperature. Above T_g, the free volume begins to increase, making the WLF model applicable only within the range from approximately T_g to T_g + 100 °C [60]. An additional assumption is that the polymer must be fully amorphous and that the same assumptions as for the TTSP hold.

The WLF model is defined in Equation 2.5. It shows the logarithmic shift factor depends on the two free volume constants, called C_1 and C_2, and the temperature difference between the selected and reference temperature. The WLF constants are determined by plotting the logarithmic shift factor versus the absolute temperature, by iterative procedure the best fits for the free volume constants are found. The constants are dependent on the reference temperature chosen and do not tell anything about the material properties. Fortunately, WLF invariants have been defined, which are independent of the reference temperate. The first WLF-invariant tells something about when all motion within a polymer is completely restricted for that polymer ($T_\infty = T_{ref} - C_2$), the

second and more important invariant is the product of the free volume constants ($C_1 \cdot C_2$). For amorphous polymers this should be in range between 900 K and 1500 K [13].

$$log(a_T) = \frac{C_1(T - T_{ref})}{C_2 + (T - T_{ref}}) \tag{2.5}$$

Arrhenius model

The WLF model has the limitation that it is not valid at temperatures below T_g, because the relation between free volume and thermal expansion breaks down. As a result, the temperature dependence of relaxation is no longer governed by free-volume expansion but instead dominated by surpassing an energy threshold. The Arrhenius model remains applicable under these conditions because it does not rely on free-volume concepts and instead characterises the relaxation process through an activation energy (E_a) [68]. The Arrhenius law expresses this behaviour through an exponential temperature dependence, as shown in the first part of Equation 2.6, where τ is the relaxation time, R is the universal gas constant and A the Arrhenius factor. When the ratio of relaxation times is taken of the working temperature and the reference temperature, it results in the last part of Equation 2.6. The activation energy becomes the only unknown and is used as an invariant to characterize the material.

$$\tau(T) = Ae^{-E_a/RT} \rightarrow log(a_T(T)) = log\frac{\tau(T)}{\tau(T_{ref})} = \frac{E_a}{R\,ln(10)}\left(\frac{1}{T} - \frac{1}{T_{ref}}\right) \tag{2.6}$$

2.5 Shape-stabilised Phase Changing Materials

The material characteristics of the individual constituents of SSPCMs have been identified together with viscoelastic properties of polymers. This section of the literature review integrates the information on the matrix and filler materials to explain how SSPCMs change with increasing wax content and how this can be used to tune their material properties. The goal of this section is to elaborate on different types of SSPCM, cover dominant material characteristics and discuss the concept of Free Fractional Volume for different wax contents.

SSPCMs is a two-component system where the PCM is encapsulated within a supporting matrix. This matrix is designed to be solid at all operating temperatures and provides the mechanical integrity to retain shape, even when the PCM component is fully molten. To achieve this a variety of encapsulation techniques can be used, for example micro encapsulation, metallic support, carbon-based support, polymer matrix or metal organic framework. The scope of this research is limited to only polymer matrix encapsulations. These are divided into polyolefins, epoxies and silicone rubbers.

Early studies used mainly polyolefins like HPDE, LDPE, LLDPE as a matrix materialsin combination with paraffin wax as a filler material. They showed good encapsulation and prevented leakage. However, they showed very limited thermal conductivity of 0.33 - 0.43 W/mk for LDPE and 0.42 - 0.51 W/mK for HDPE. To solve this a filler like graphite can be added, graphite is miscible with polyolefin/wax blends. It turns out that the thermal conductivity of the blends increases almost linearly with the addition and increase in the content of the conductive filler irrespective of the conductive particle used [79].

2.5.1 Viscoelastic properties

More recent works have turned to silicone rubber matrices to create SSPCMs. A study of Shi et al. [98] showed the influence of wax content on silicone rubber-wax compounds. They performed a DMA test to find the viscoelastic properties of the different composition ranging from 0 % wax to 30 % wax. They found that at temperatures below the wax melting area (around 50 °C), adding wax increases the storage modulus. Once the temperature is within the melting area, the storage modulus dropped by a factor of 10, see Figure 2.6a. For compounds with a high wax content this drop was even more significant. This result is consistent with the theory: at low temperatures, the wax is a solid and is dispersed within the silicone rubber matrix, as semi-crystalline paraffin wax

has a higher modulus than the silicone rubber, the net modulus increases. When the temperature is outside the melting area, the wax has turned into a liquid no longer acting as a reinforcement. Instead, it functions as a plasticizer for the silicone rubber polymer chains. A plasticizer increases the chain mobility and reduces the modulus. The higher the wax content the more profound this effect is [98].

The loss factor for the different wax compositions is shown in Figure 2.6b. The highest loss factor is observed in the SSPCMs with the highest wax content, demonstrating that damping capacity increases with wax content in the melting area. Notably, the temperature at which the peak loss factor occurs does not shift with wax composition. All mixtures exhibit their maximum damping at the same temperature where the storage modulus drops. This indicates that the melting area of the wax governs the peak position of the loss factor, independent of the wax composition. Beyond this melting area, the loss factor decreases as the material transitions into the rubbery state, as explained in Section 2.3.1. Shi et al. also reported that the amplification of the loss-factor peak becomes significant only when the wax content exceeds approximately 20 wt%. Furthermore, the study found that the elongation at break decreases with increasing wax content. The presence of solid wax makes the SSPCM more brittle, resulting in lower strain at failure [98].

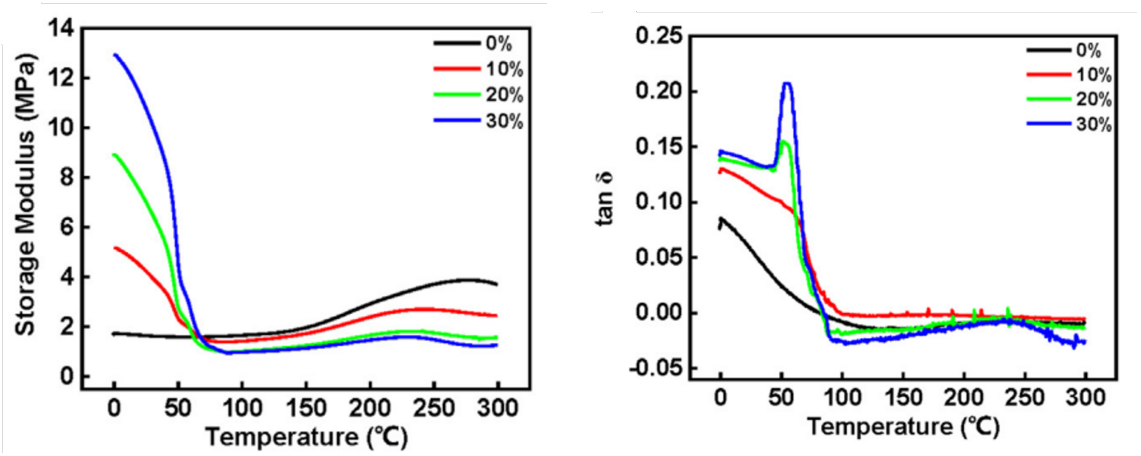

(a) *E' for various silicone rubber–wax compositions* **(b)** *$tan(\delta)$ for different silicone rubber–wax compositions*

Figure 2.6: *The viscoelastic properties of the silicone rubber–wax compositions, as determined from DMA measurements [98]*

2.5.2 Coefficient of thermal expansion

In silicone rubber–wax SSPCMs, the wax content largely determines the overall thermal expansion, as the PCM undergoes the most significant volumetric change during melting of the wax. The silicone rubber matrix, characterised by high flexibility and a large elongation at break, can stretch and deform to accommodate this expansion without losing structural integrity. This elastic behaviour makes silicone rubber a suitable matrix material. The CTE of silicone rubber is expected to remain nearly constant over the measured temperature area (discussed in Section 2.2.4), whereas the wax shows a sharp increase in the melting area (discussed in Section 2.1.6). The highest CTE therefore, occurs at the wax melting area.

2.5.3 Thermal conductivity

As mentioned in Section 2.1.5 and 2.2.3, the thermal conductivity of silicone rubber and wax are very low, both acting as an insulator. The results is that increasing the wax content does not result in a significant change to the total thermal conductivity [98].

2.5.4 Fractional Free Volume

The Free Volume Fraction (FFV) is a parameter that defines how much unoccupied space there is within the material. It is defined by Equation 2.7 and can be interpreted as the ratio of the free volume over the occupied volume, where the specific volume (V_{sp}) is the inverse of the materials' density [117]. It shows that the material properties are not governed by the total volume but by the free volume. Moreover, a low FFV is associated with higher viscosity and modulus due to decreased molecular mobility, as shown by Lee et al. [63]. In contrast, when the FFV is high the chains have more space to move and as a results viscosity and modulus are low.

The FFV can be estimated in three ways: the Bondi method, the PVT method and the PALS method. The last two require expensive machines and long testing procedures, fortunately the first method is based on empirical formulation and can be evaluated by Equation 2.7.

$$FFV = \frac{V_{sp} - V_{oc}}{V_{sp}} \tag{2.7}$$

To determine the FFV, the occupied volume (V_{oc}) must first be defined, as shown in Equation 2.8. This expression uses the dimensionless packing factor (α_p), a semi-empirical constant typically between 1.2 and 1.4, which corrects the idealised assumptions of the specific van der Waals volume (v_w). The correction is needed because the van der Waals volume assumes perfectly spherical molecular packing at 0 K, whereas real molecules require additional space to form bonds and are measured at much higher temperatures [117].

$$V_{oc} = \alpha_p v_w \tag{2.8}$$

The next step is to determine the specific van der Waals volume, as defined in Equation 2.9. This quantity represents the ratio of the van der Waals volume (V_w) per unit of molar mass (M_w), both depending on the chosen material.

$$v_w = \frac{V_w}{M_w} \tag{2.9}$$

To determine these properties, first a unit cell size is chosen, which is a sort of repeating unit for the chosen material. For silicone rubber, this unit is dimethylsiloxane ($Si(CH_3)_2$–O), while for paraffin wax it is a small hydrocarbon group (CH_2). Literature values for these molecular units, together with density measurements obtained via the Archimedes principle, are listed in Table 2.1, where 'SR' denotes silicone rubber and 'PW' denotes paraffin wax properties. With these parameters, the FFV of the pure constituents can be calculated. However, determining the FFV of a SSPCMs requires combining the properties of silicone rubber and wax. Using the rule of mixtures based on the volume fraction of each component Equations 2.7 to 2.9 can be adjusted. The resulting FFV for various compositions are summarised in Table 2.2.

Based on the results in Table 2.2, the FFV increases approximately linearly with rising wax content. This implies that the CTE increases with higher wax fractions, which is consistent with the temperature-dependent expansion behaviour described in Section 2.2.4. The link between composition, FFV and CTE becomes clearer when considering how FFV evolves with temperature.

Table 2.1: *Material properties required for calculating the fractional free volume*

Variables	Value	Unit
ρ_{SR}	1.08	g/cm^3
$V_{w,SR}$	50.6 [120]	cm^3/mol
$M_{w,SR}$	74.1 [76]	g/mol
ρ_{PW}	0.864	g/cm^3
$V_{w,PW}$	10.2 [70]	cm^3/mol
$M_{w,PW}$	14.03 [76]	g/mol
α_p	1.30 [47]	-

Table 2.2: *Calculated fractional free volume for different silicone rubber–wax composition using the Bondi method*

Composition (si/wax vol%)	FFV [%]
100/0	4.39
85/15	6.45
70/30	8.51
50/50	11.3
30/70	14.0
15/85	16.1
0/100	18.1

To evaluate FFV over a temperature range, the occupied volume is assumed to remain constant. As temperature increases, the specific volume of the material grows due to a reduction in density, causing FFV to increase proportionally. Combined with the compositional trend, this means that both higher wax content and higher temperatures lead to increased FFV, and therefore, to a higher CTE.

3 | Modal analysis basics

To find the material properties of a dynamic system, one of the simplest yet most instructive models is the single degree of freedom (SDOF) mass–spring–damper system. Although its direct applicability to real structures is limited, it provides essential insight in how a system can be modelled and will form the basis for analysing multi degree of freedom (MDOF) systems. Before introducing these models, it is important to address one of the most challenging aspects of structural dynamics: damping. While the mass and stiffness matrices can be derived directly from the geometry and material properties, damping is far more complex to characterise and typically requires experimental testing. Therefore, Section 3.1 first introduces the main damping concepts and models that will be used throughout this work.

Building on this foundation, Section 3.2 describes the free and forced vibration response of an SDOF system and introduces the concept of the Frequency Response Function (FRF). Section 3.3 then generalises these ideas to MDOF systems by deriving the free and forced vibration response, first without damping and subsequently including structural damping in the most general case. Section 3.4 presents the experimental modal analysis (EMA). It explains how FRF matrices are obtained using impact hammer and shaker excitation testing and discusses key concepts such as reciprocity and linearity. Finally, Section 3.5 describes the post-processing required to extract the modal parameters using the peak picking, line fit and logarithmic decrement method.

3.1 Damping

Damping is characterised by how mechanical energy is dissipated via heat. When a structure vibrates, a part of the energy is lost due to for example fluid friction, (internal) friction or air resistance. This causes the vibration response to decay over time, even in the absence of external forces.

Mathematically, damping is defined as a force opposing the motion of an object. To describe this force, three different damping models are used: viscous damping, hysteretic damping (or structural damping) and viscoelastic damping. The first two types are covered in this section and the viscoelastic damping was already covered in Section 2.3. In practice the damping is often a combination of multiple models because, these are purely theoretical.

Viscous damping is typically used in mechanical and structural systems, because it provides a simple expression. It dissipates energy through fluid friction which creates shear stresses. It is modelled by a dashpot element where the damping force is proportional to the velocity, expressed by $F_d = c\dot{x}$. The damping coefficient is defined by c in units of Ns/m and $\dot{x}$ represents the velocity. It becomes apparent that in this formulation the damping is always in phase with the velocity. The velocity is frequency dependent and consequently the damping force varies with frequency as well. This becomes problematic if a SDOF model over a wide range of frequencies is required, as a high frequency results in a higher damping. This is not realistic because most structures behave independent from frequency [30].

An alternative model that solves this problem is hysteretic damping. This is caused by (internal) friction within the material during cyclic loading. The damping force is velocity independent and appears as phase lag in the stiffness. Mathematically, it is often incorporated via a complex stiffness $F_d = (k(1 + i\eta)x$, where η is the dimensionless loss factor and x the displacement. When this formulation is used, a constant damping can be defined independent of the velocity and frequency.

3.2 Single Degree Of Freedom systems

First, the standard SDOF mass–spring–damper system is analysed for its free vibration response, after which the corresponding forced vibration response is derived.

3.2.1 Free vibration response of a SDOF system

The Equation Of Motion (EOM) for the standard SDOF mass–spring–damper system is shown in Figure 3.1. The displacement ($x(t)$) depends on the stiffness of the spring (k), the damping coefficient of the damper (c) and the weight of the mass (m). Each element applies a force, such that when a Free Body Diagram (FBD) is constructed and the sum of forces in the x-direction is considered, the EOM of the system can be derived. It takes the form of a second-order linear homogeneous Ordinary Differential Equation (ODE) as displayed in Section 3.1. For the free vibration response, no external forces are assumed. The corresponding mass-normalised form, obtained by dividing the entire equation by the mass, is also presented in Equation 3.1.

$$\Sigma F_x = m\ddot{x} = -kx - c\dot{x} \rightarrow m\ddot{x} + c\dot{x} + kx = \ddot{x} + \frac{c}{m}\dot{x} + \frac{k}{m}x = 0 \tag{3.1}$$

When also the damping is neglected the definition for the eigenfrequency can be derived. The EOM reduces to just $m\ddot{x} + kx = 0$. It is straightforward to derive the expression for the eigenfrequency when a harmonic trial function is used, as shown in Equation 3.2.

$$x = Xsin(\omega t) \rightarrow m(-X\omega^2 sin(\omega t)) + k(Xsin(\omega t)) \rightarrow \omega_n = \sqrt{\frac{k}{m}} \tag{3.2}$$

When revisiting Equation 3.1, it is common practice in dynamics to express it in an alternative form, as shown in Equation 3.3.

$$\ddot{x} + 2\zeta\omega_n + \omega_n^2 x = 0 \tag{3.3}$$

This form is often used because it provides a simple expression for the eigenfrequency, as shown in Equation 3.2 and defines the damping ratio, as shown in Equation 3.4 [95].

$$\zeta = \frac{c}{2m\omega_n} \tag{3.4}$$

3.2.2 Forced vibration response of an SDOF system

To find the forced vibration response of a SDOF system, the standard mass-spring-damper model is considered again. This time an arbitrary excitation force ($F(t)$) is applied, resulting in an arbitrary excitation displacement ($X(t)$). This adds an additional component to the force balance as shown in Equation 3.5.

$$\Sigma F_x = m\ddot{x} = -kx - c\dot{x} + F(t) \rightarrow F(t) = m\ddot{x} + c\dot{x} + kx \tag{3.5}$$

In Equation 3.5, the objective is to determine the displacement response of the system from the EOM. To facilitate this, an exponential trial function is introduced for both the displacement and the external excitation, as expressed in Equation 3.6. The equation is transformed from the time domain to the frequency domain.

$$x = Xe^{i\omega t} \rightarrow \dot{x} = Xi\omega e^{i\omega t} \rightarrow \ddot{x} = -X\omega^2 e^{i\omega t}, F(t) = Fe^{i\omega t} \tag{3.6}$$

Upon substitution this yields the EOM shown in Equation 3.7.

$$(-\omega^2 m + i\omega c + k)Xe^{i\omega t} = Fe^{i\omega t} \tag{3.7}$$

Next the response model can be extracted in terms of the FRF. This functions describes how the output of a system is related to the input. It characterizes both the magnitude and phase of the response, showing how the system amplifies or attenuates vibrations at different frequencies.

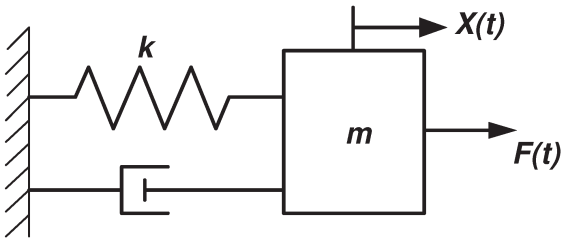

Figure 3.1: *Schematic of a SDOF mass-spring-damper system*

Using the FRF several modal parameters can be extracted like eigenfrequencies, mode shapes and damping ratios. Mathematically, the FRF is obtained by dividing output over the input, applied to Equation 3.7, this yields the expression shown in Equation 3.8. It is called the receptance and is denoted by $\alpha(\omega)$.

$$H(\omega) = \alpha(\omega) = \frac{X(\omega)}{F(\omega)} = \frac{1}{-\omega^2 m + i\omega c + k} \tag{3.8}$$

3.2.3 Mobility and accelerance

The output however, is not always a displacement. It depends on the measurement sensor and can also be a velocity or acceleration. For example, if the output is the velocity, the mobility can be defined by $Y(\omega)$ as shown in Equation 3.9.

$$H(\omega) = Y(\omega) = \frac{v}{F} = i\omega\frac{X}{F} = i\omega\alpha(\omega) \tag{3.9}$$

Similarly, the acceleration can be used, which is very common in modal testing. The acceleration over the input force is called the inertance or accelerance ($A(\omega)$) and is related to the receptance according to Equation 3.10. It emphasizes high-frequency modes and reduces the influence of rigid-body motions [96].

$$H(\omega) = A(\omega) = \frac{a}{F} = -\omega^2\frac{X}{F} = -\omega^2\alpha(\omega) \tag{3.10}$$

3.3 Multi Degree Of Freedom systems

In real structures, a SDOF model cannot accurately represent the dynamic behaviour of a system therefore, a MDOF system is introduced. While an SDOF system requires only one EOM and has one FRF, a MDOF system with N degrees of freedom requires N EOMs and N^2 entries for the FRF to be fully defined. As a result, the system dynamics are expressed using vectors and matrices instead of scalars. To illustrate the concept, a N DOF model is presented. First, the free vibration of a MDOF system without damping is derived, secondly the forced vibration without damping and lastly the most complex model which includes damping of a forced vibration response is derived.

3.3.1 Free vibration response of MDOF system excluding damping

The EOM of a MDOF system without damping is shown in Equation 3.11, where $\mathbf{M}$ and $\mathbf{K}$ are N by N mass and stiffness matrices and $\mathbf{x}(t)$ is a N by one displacement vectors as a function of time. For clarity the time is not shown in the equations hereafter.

$$\mathbf{M}\ddot{\mathbf{x}}(t) + \mathbf{K}\mathbf{x}(t) = \mathbf{0} \tag{3.11}$$

In a MDOF system, similarly to the SDOF system, the solution for displacement must be found. To solve for this, the free vibration response is considered as this reveals the eigenfrequencies and mode shapes of the system. If a freely vibrating system is assumed, no external

forces act on it and the governing equation reduces to a coupled, second-order, linear, homogeneous differential equation. In that case the general trial solution is known to be very similar to the SDOF solution (Equation 3.6). The only difference is that the displacement is now a vector instead of scalar.

When the trial solution is substituted in the EOM of Equation 3.11, it yields Equation 3.12. To solve this equation, it is recognised that the exponential function can never be zero. Another solution occurs when $\mathbf{X} = 0$. This is the trivial solution and indicates that the system is not in motion. Therefore, the only non-trivial solution occurs when the term in brackets is zero. In this case the non-trivial solution exists if the determinant of the term between brackets is zero, because this means that the matrix is not singular and that there are non-zero solutions.

$$(\mathbf{K} - \mathbf{M}\omega^2)\mathbf{X}e^{i\omega t} = \mathbf{0} \tag{3.12}$$

When Equation 3.12 is rewritten to Equation 3.13 it is in the form of the generalized eigenvalue problem. In standard form it looks like $\mathbf{Ax} = \lambda\mathbf{Bx}$, where λ are the eigenvalues and $\mathbf{x}$ the eigenvectors. When the determinant is found it results in a characteristic equation for ω^2. This is a polynomial equation that can be solved analytically; the results are the eigenvalues or in this context the eigenfrequencies of the system. The number of eigenfrequencies is equal to NDOF and is often expressed as a diagonal eigenvalue matrix ($\boldsymbol{\omega_r^2}$). When the eigenvalues are back substituted in the eigenvalue problem the eigenvectors are obtained or in this context the mode shapes. This eigenvector matrix is denoted by $\mathbf{\Psi_r}$ and is a NDOF by NDOF matrix, where the columns represent each mode shape and the rows the relative movement of these mode shapes with respect to each other for each DOF.

$$det(\mathbf{K} - \omega^2\mathbf{M}) = 0 \rightarrow \mathbf{KX} = \omega^2\mathbf{MX} \tag{3.13}$$

A key observation is that the eigenvalue matrix contains the unique eigenfrequencies of the system, while the eigenvector matrix does not. The mode shapes are subjected to an arbitrary scaling factor, which does not affect the shape but only the amplitude. It is said that those mode shapes are linearly independent. How the modes shapes are normalised depends on which mathematical procedure is followed, but within structural dynamics mass normalisation is commonly used.

To define mass normalisation first the orthogonality of modes is considered. Equation 3.14 and 3.15 show that a pre and post multiplication of the relative eigenvector matrix with the mass and stiffness matrix result in diagonal modal mass (m_r) and stiffness matrix (k_r). These matrices are still subjected to arbitrary scaling and are not unique, the ratio however, is unique and is equal to the eigenvalue, $\omega_r^2 = k_r/m_r$.

$$\mathbf{\Psi^T M \Psi} = diag(m_r) \tag{3.14}$$

$$\mathbf{\Psi^T K \Psi} = diag(k_r) \tag{3.15}$$

The next step in mass normalisation is to use the modal mass and stiffness matrices to scale the mode shapes such that each mode has a unit modal mass. In Equation 3.14 this can be achieved by dividing by m_r, which yields an identity matrix. The Left Hand Side (LHS) contains $\mathbf{\Psi}$ twice, so to transform the unscaled modes to the scaled modes ($\mathbf{\Phi}$) a scaling factor equal to the square root of the modal mass is required, see Equation 3.16.

$$\mathbf{\Psi} = \mathbf{\Phi}\sqrt{m_r} \tag{3.16}$$

When Equation 3.16 is substituted in 3.14 and 3.15 it yields the reduced mass and stiffness matrix, shown in Equation 3.17 and 3.18.

$$\mathbf{\Phi}^T\sqrt{m_r}\mathbf{M}\mathbf{\Phi}\sqrt{m_r} = diag(m_r) \rightarrow M_{red} = \mathbf{\Phi}^T\mathbf{M}\,\mathbf{\Phi} = \mathbf{I} \tag{3.17}$$

$$\mathbf{\Phi}^T\sqrt{m_r}\mathbf{K}\,\mathbf{\Phi}\sqrt{m_r} = diag(k_r) \rightarrow \mathbf{\Phi}^T\mathbf{K}\,\mathbf{\Phi}\,m_r = diag(k_r) \rightarrow K_{red} = \mathbf{\Phi}^T\mathbf{K}\,\mathbf{\Phi} = diag(\omega_r^2) \tag{3.18}$$

The major advantage of mass normalisation is that it simplifies the mathematical formulation. The transformation to scaled modes enables the EOMs to be decoupled into SDOF systems, which can be solved in a more efficient manner than MDOF systems. Mass normalisation also helps to facilitate direct comparison between the modes.

3.3.2 Forced vibration response of MDOF system excluding damping

The forced vibration response describes how the structure behaves when subjected to external loads. It uses a similar expression asin Equation 3.11, the only difference is the force vector ($\mathbf{F}(t)$) is included at the RHS, see Equation 3.19.

$$\mathbf{M}\ddot{\mathbf{x}}(t) + \mathbf{K}\mathbf{x}(t) = \mathbf{F}(t) \tag{3.19}$$

To solve for the displacement a similar trial function is used as in Section 3.2, Upon substitution in 3.19, yields Equation 3.20

$$(\mathbf{K} - \mathbf{M}\omega^2)\mathbf{X}e^{i\omega t} = \mathbf{F}e^{i\omega t} \rightarrow (\mathbf{K} - \mathbf{M}\omega^2)\mathbf{X} = \mathbf{F} \tag{3.20}$$

A unique solution for the displacement response exists only when the term in brackets is non-singular, meaning that its determinant is non-zero and the matrix can be inverted, resulting in Equation 3.21. The matrix $\mathbf{Z}$ is referred to as the impedance matrix, while the inverse is the receptance as defined in Section 3.2.

$$\mathbf{X} = (\mathbf{K} - \mathbf{M}\omega^2)^{-1}\mathbf{F} \rightarrow \mathbf{X} = \mathbf{Z}^{-1}\mathbf{F} = \alpha\mathbf{F} \tag{3.21}$$

It is evident from Equation 3.21 that the system response can be evaluated by substituting the corresponding mass, stiffness and force matrices over a range of excitation frequencies. However, determining the displacement requires computing the inverse of the mass and stiffness matrix, which becomes computationally expensive for systems with a large number of DOF. Moreover, this approach is inefficient when only a limited number of FRFs are of interest. Therefore, an alternative formulation is often used, in which the receptance matrix is expressed as a summation of modal contributions, allowing the response to be efficiently computed through modal superposition. Modal superposition is a method used to determine the dynamic response of a MDOF system by expressing the dynamic response as a linear combination of its mode shapes.

Using the definition of the receptance in Equation 3.21, premultiplying by $\mathbf{\Phi}^T$ and postmultiplying by $\mathbf{\Phi}$, results in Equation 3.22.

$$\mathbf{\Phi}^T(\mathbf{K} - \omega^2\mathbf{M})\mathbf{\Phi} = \mathbf{\Phi}^T\alpha(\omega)^{-1}\mathbf{\Phi} \tag{3.22}$$

This can further be simplified by substituting Equation 3.17 and 3.18 in 3.22, this yields Equation 3.23.

$$diag(\omega_r^2) - \omega^2 = \mathbf{\Phi}^T\alpha(\omega)^{-1}\mathbf{\Phi} \tag{3.23}$$

When the receptance is isolated, it results in Equation 3.24

$$\alpha(\omega) = \mathbf{\Phi}[diag(\omega_r^2) - \omega^2]^{-1}\mathbf{\Phi}^T \tag{3.24}$$

From Equation 3.24, it follows that in the absence of damping, the receptance matrix is symmetric. This symmetry reflects the principle of reciprocity, which is further discussed in Section 3.4.1.

Equation 3.24 has eliminated the drawbacks mentioned before. Even though the inverse must still be computed; it is rather easy because the matrix is diagonal. The inverse is calculated as the individual components divided by one. Additionally, a single FRFs can now be calculated, further reducing computation time. Equation 3.24 can be rewritten even further. The goal was to express all possible FRFs as the sum of the contribution of all modes. In component form Equation 3.24 gives Equation 3.25. It shows a summation that starts at the first mode and ends at the last mode. To finalise the derivation, a new variable is introduced called the modal constant or residue ($A_{jk,r}$) and is referred to as the product of the mode shapes.

$$\alpha_{jk}(\omega) = \sum_{r=1}^{M} \frac{\Phi_{jr}\Phi_{kr}}{diag(\omega_r^2) - \omega^2} = \sum_{r=1}^{M} \frac{A_{jk,r}}{diag(\omega_r^2) - \omega^2} \tag{3.25}$$

3.3.3 Forced vibration response of MDOF system including damping

Until now all MDOF systems have been considered without any damping, to keep the derivation simple. However, the assumption of no damping does not hold in practice because all structures will exhibit some degree of damping. The viscous damping described before is not representative in real structures. Therefore, hysteretic damping will be used to describe the damping. When this term is implemented in the EOM it yields Equation 3.26.

$$(\mathbf{K} + i\mathbf{D} - \omega^2\mathbf{M})\mathbf{X}e^{i\omega t} = \mathbf{F}e^{i\omega t} \tag{3.26}$$

A similar procedure can be applied to mitigate the inefficient calculation of the FRFs. Therefore, the receptance will be premultiplied and post-multiplied by the mode shapes. This results in one additional term $\mathbf{\Phi^T} i\mathbf{D}\mathbf{\Phi}$, which is incorporated as the complex damping $(1 + i\eta_r)$. The result is shown in Equation 3.27, where the term in brackets is a diagonal matrix.

$$\alpha(\omega) = \mathbf{\Phi}(diag(\omega_r^2(1 + i\eta_r)) - \omega^2)\mathbf{\Phi^T} \tag{3.27}$$

Upon rewriting using index notation a similar expression is defined as in Equation 3.25. Equation 3.25 shows the final result and again this formulation enables calculating each FRF separately. This equation forms the basis for synthesising the FRFs. When the eigenfrequency (ω_r^2), loss factor (η_r) and modal constant (A_{jk}) are determined, the FRF can be synthesised. This research will cover the two methods to find the modal parameters to synthesise the FRF: the peak picking method explained in Section 3.5.1 and the line fit method explained in Section 3.5.2.

$$\alpha_{jk}(\omega) = \frac{x_j}{F_k} = \frac{Output}{Input} = \sum_{r=1}^{M} \frac{\Phi_{jr}\Phi_{kr}}{\omega_\mathbf{r}^2 - \omega^2 + i\eta_r\omega_r^2} = \sum_{r=1}^{M} \frac{A_{jk,r}}{\omega_\mathbf{r}^2 - \omega^2 + i\eta_r\omega_r^2} \tag{3.28}$$

3.4 Experimental modal testing

The theory presented above must be validated through experimental modal testing. This section introduces the FRF matrix and explains how it can be simplified using the principle of reciprocity. The assumption of linearity and coherence are also briefly addressed. Finally, the use of impact hammer and shaker excitation testing is discussed, showing how these techniques are used to fill the remaining entries of the FRF matrix.

3.4.1 FRF matrix

As shown by Equation 3.28 there are multiple FRFs in a MDOF system. Therefore, the FRF matrix allows capturing all excitation response relationships in one compact form. It has the dimensions of NDOF by NDOF with N^2 entries, see Equation 3.29. Each element $(H_{jk}(\omega))$ denotes the response at coordinate j resulting from an excitation force applied at coordinate k, with the columns corresponding to response locations and the rows to excitation locations.

$$\mathbf{H}(\omega) = H_{jk}(\omega) = \begin{bmatrix} H_{11} & H_{12} & \cdots & \cdots & H_{1k} \\ H_{21} & H_{22} & \cdots & \cdots & \vdots \\ \vdots & \vdots & \ddots & & \vdots \\ \vdots & \vdots & & \ddots & \vdots \\ H_{j1} & \cdots & \cdots & & H_{jk} \end{bmatrix} \tag{3.29}$$

When the excitation force and the measured response act at the same physical location and in the same direction, the measurement is referred to as a driving-point FRF. In the FRF matrix, these

correspond to the diagonal elements ($H_{ii}(\omega)$). Driving-point measurements are essential because they directly relate the applied force to the resulting response at that point, providing information about the absolute motion of the structure. These measurements are important for modal scaling, as it allows the determination of absolute mode shapes.

The off-diagonal elements of the FRF matrix represent the transfer FRFs, which describe the response at one coordinate due to an excitation at another. These functions show the coupling between different points and illustrate how vibrations propagate through the structure. In combination with the driving-point FRFs, the transfer FRFs enable the identification of the structure's relative mode shapes.

During a test, filling an entire FRF matrix is often labour-intensive, as each excitation location requires a separate set of measurements. A common approach to reduce testing time is to increase the number of response sensors (e.g. accelerometers), allowing multiple response points to be measured simultaneously for a single excitation. This approach fills the columns of the FRF matrix. However, excessive sensor mass can change the dynamic properties of the structure, leading to measurement errors.

It is often not required to measure the complete FRF matrix to accurately identify a systems dynamic properties. In most cases, one or two excitation points, combined with a larger number of response points, are sufficient. Among these, at least one should be a driving-point measurement to ensure proper modal scaling and one should be a transfer FRF. Even with a limited set of FRFs, it is possible to extract the key modal parameters including eigenfrequencies, damping ratios and mode shapes.

3.4.2 Reciprocity

Another possible way to reduce the number of entries to fill the FRF matrix is to assume principle of reciprocity. This principle applies when the response at point j due to a excitation in point k is the same as a response in point k due to an excitation in point j. This allows the FRF matrix to be symmetric, which indicates that only half of the number of measurements are needed. It also suggests symmetric mass, damping and stiffness matrix, as proven in Section 3.3.3. Mathematically a symmetric FRF matrix is expressed as $H_{jk} = H_{kj}$. However, in practice two FRFs never perfectly overlap, due to measurement uncertainties, improper sensor placement, varying boundary conditions, added mass of the sensor etc. As a consequence, reciprocity is often used a consistency check. When H_{jk} and H_{kj} differ significantly, it may suggest an incorrect measurement setup.

3.4.3 Linearity

Verifying if a system is linear is an important concept within structural dynamics. A system is linear when, first, the response is independent of the magnitude of the excitation. This means that when several soft and hard excitations are applied to the same points all results must be the same. The second criterion states that the deflection caused by two forces applied simultaneously must equal the sum of the deflections produced when each force is applied individually.

3.4.4 Impact hammer Testing

Impact hammer testing uses a calibrated force hammer to create a short, controlled impact on the structure, simultaneously an accelerometer is used to measure the response. Typical user cases are in lightweight structures with light to moderate damping, because the vibrations do not disappear too quickly after the impact. The biggest advantage of this method is that it is efficient and simple, while also being highly flexible due to the ease of changing of the excitation point.

3.4.5 Shaker excitation testing

In a shaker excitation test, an electrodynamic actuator is used to apply a controlled and continuous force over a defined frequency range. This method is typically used for larger or more heavily damped structures, where a stable and precisely controlled excitation is required and where an impact hammer cannot provide sufficient input force. Although the shaker setup is less flexible

and more time-consuming to configure compared to hammer testing, it offers the advantage of high consistency and repeatability

3.4.6 Coherence

In an ideal linear system the input and output are directly related, but in practice the measured response always contains some noise. Such noise may arise from poor excitation, non-linear behaviour, sensor errors or any disturbance not originating from the intended input. To quantify how much of the measured output can be explained by the applied input, the coherence function is introduced. It provides a direct indication of whether features in the FRF, such as resonance peaks or damping estimates, are physically meaningful or artefacts. Coherence is a dimensionless quantity obtained by combining the power spectral densities (S) of the input (I) and output (O) signals, as shown in Equation 3.30. Its value ranges from zero to one, where zero indicates that the input cannot explain the output and one reflects a perfect relationship. In this work, it is used to assess how reliably the hammer and shaker excitation predict the dynamic response of the system [30].

$$\gamma^2(f) = \frac{|S_{IO}(f)|^2}{S_{OO}(f)\, S_{II}(f)} \tag{3.30}$$

3.5 Modal parameter extraction methods

The most basic approach to modal analysis is the SDOF method, where it is assumed that each resonance peak is evaluated separately. When multiple modes are close in frequency, both magnitudes contribute to the response, which makes it difficult to isolate the modal properties of a single peak. In other words, for the SDOF approach to work, the behaviour of one peak should be dominating. Common SDOF techniques are the peak picking method, line fit method and logarithmic decrement method which will be discussed below, but also the circle fit method is a possibility.

3.5.1 Peak picking

The peak picking or peak amplitude method is an easy and powerful tool to quickly evaluate the modal properties of a system. In this method one peak is completely isolated from the rest and treated while ignoring all other modes. The method works as follows: the eigenfrequency (ω_r) of a mode is determined by finding a local optimum for this mode, H_{max}, shown in Figure 3.2. The next step is to determine the response level of the FRF. This can be found by $H_{max}/\sqrt{2}$ or if the response is converted to logarithmic and expressed in decibels the response level is 3 dB lower than H_{max}. The response level will intersect the FRF twice, called ω_a and ω_b and are shown in Figure 3.2. Now all frequencies are determined and using Equation 3.31 the loss factor can be determined.

$$\eta = \frac{\omega_a^2 - \omega_b^2}{2\omega_r^2} \tag{3.31}$$

The last unknown modal parameter in Equation 3.28 to completely synthesise the FRF, is the modal constant (A_r). Without further derivation, the modal constant can be calculated by applying the expression in Equation 3.32 [30]. There are, however, some limitations to this method, peak picking assumes a linear system. Additionally, the method works best for lightly damped modes, because peak picking requires the resonance peaks to be in a narrow range. Lastly, the peak picking method only results in real modal constants this implies that only real modes or proportionally damped structures can be described. In practice, this is often not the case and the modes are complex. A method that does include complex modes, is the line fit method, which is explained in the following section.

$$A_r = \mid H_{max} \mid \omega_r^2 \eta_r \tag{3.32}$$

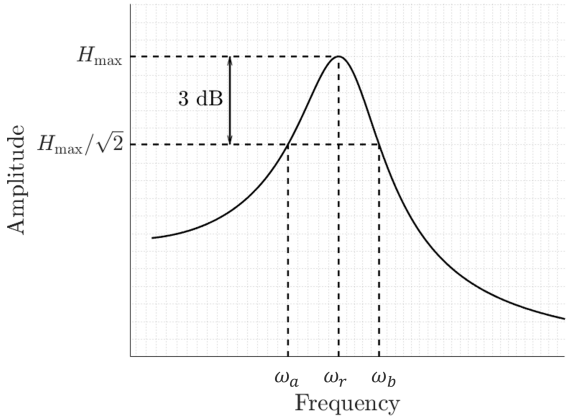

Figure 3.2: *Schematic representation of the peak picking method*

3.5.2 Line fit method

The line fit method, also known as the inverse method, provides an alternative approach for extracting modal parameters. It is based on the fact that when the reciprocal of the receptance is plotted (real and imaginary) for a narrow frequency band in the vicinity of the eigenfrequency, it traces out a straight line which can be fit with constants that describe the modal parameters. The method is best suited for real valued modes, because it assumes one single dominant mode, minimal interaction between modes and lastly a low damping. However, to still account for the imaginary part the modal constant is assumed to be complex. The goal is to find expression for the modal parameters similar to Section 3.5.1, such that the response can be synthesised.

The derivation starts with the reciprocal of the receptance corresponding to a single mode. For an SDOF system, this inverse FRF forms a perfect straight line when plotted in the complex plane against ω^2. In contrast, for real structures, the measured FRF represents the superposition of multiple modal contributions rather than a single isolated mode, as previously expressed in Equation 3.25. When this equation is inverted for MDOF systems it does not yield the same result as when each individual mode is summed and inverted. In other words, the inverse of a sum is not the same as the sum of inverses, Equation 3.33. Even though each single mode term individually would yield a straight line when inverted, their combined response cannot be separated by simply taking the reciprocal of the sum and as a result the line in the complex plane is not straight anymore.

$$\alpha_{jk}(\omega)^{-1} = \left(\sum_r \frac{A_{jk,r}}{\omega_r^2 - \omega^2 + i\omega_r^2\eta_r} \right)^{-1} \neq \sum_r \frac{\omega_r^2 - \omega^2 + i\omega_r^2\eta_r}{A_{jk,r}} \tag{3.33}$$

To restore the linear relationship a local modified inverse FRF is used. An new variable is introduced as a correction term (α'_{jk}) and is simply the difference between the actual FRF ($\alpha_{jk}(\omega)$) and the value of the FRF at one fixed frequency in the range of interest, this frequency is referred to as the fixing frequency and is represent by $\alpha_{jk}(\Omega)$. So the correction term is defined as Equation 3.34.

$$\alpha'_{jk}(\omega) = \alpha_{jk}(\omega) - \alpha_{jk}(\Omega) \tag{3.34}$$

The next step introduces the inverse FRF parameter ($\Delta(\omega)$), defined in Equation 3.35. This quantity scales the frequency-squared difference relative to the chosen fixing frequency, by dividing the corrected receptance term. In this formulation, the numerator represents the deviation from the fixing frequency, while the denominator ensures that the modal contributions of other modes are removed.

$$\Delta(\omega) = \frac{\omega^2 - \Omega^2}{\alpha'_{jk}(\omega)} \rightarrow \Delta(\omega) = Re(\Delta) + iIm(\Delta) \tag{3.35}$$

Advancing to the next step, the $\Delta(\omega)$ is split in a real part and imaginary part. For a fixed Ω, both the real and imaginary parts of $\Delta(\omega)$ vary almost linearly with ω^2, allowing them to be expressed as a Equation 3.36.

$$Re(\Delta) = m_R\omega^2 + c_r \ \wedge Im(\Delta) = m_I\omega^2 + c_I \tag{3.36}$$

The procedure involves two successive linearisation stages, first with respect to the measurement frequency ω and subsequently with respect to the fixing frequency Ω. In the first stage, a least-squares regression is applied to determine the coefficients m_r, m_I, c_R and c_I for a constant fixing frequency. These coefficients describe how the inverse FRF behaves locally around the resonance and thus represent the first-stage linearisation of the method. Because the results still depend on the chosen fixing frequency, a second-stage linearisation is introduced. When the slopes from the first stage slopes and intercepts are computed for several fixing frequencies, they also themselves exhibit a linear dependence on Ω^2, as shown in Equation 3.37. Similarly a least squares fit is applied to find the new constants n_r, n_I, d_r and d_I, these are directly related to the modal parameters as shown in Equation 3.38 for the eigenfrequency, the loss factor in 3.39 and the real and imaginary part of the modal constant in 3.40 and 3.41 related as $A_{jk,r} = A_r + iB_r$.

$$m_R = n_R\Omega^2 + d_R \ \wedge m_I = n_I\Omega^2 + d_I \tag{3.37}$$

$$\omega_r^2 = \frac{n_R d_R + n_I d_I}{n_R^2 + n_I^2} \tag{3.38}$$

$$\eta_r = \frac{n_R d_I - n_I d_R}{n_R d_R + n_I d_I}. \tag{3.39}$$

$$A_r = n_R \tag{3.40}$$

$$B_r = -n_I \tag{3.41}$$

One of the biggest advantages over other methods is that for most methods they rely on reliable measurements near the resonance region, while those points are also the most challenging to measure. In the line fit method however, the emphasis is more on the points further away from the eigenfrequency as they determine the slope of the real and imaginary graph. Therefore, this method is likely to be less sensitive to measurement errors. Secondly, the straight-line feature means that it is easier to spot discrepancies, when the data does not lay on the straight line it may indicate poor data capturing, inappropriate damping or non-linear behaviour [30] .

3.5.3 Logarithmic decrement method

The last method that is discussed can only be used in the time domain. This brings as an advantage that it requires less computational effort because no transformation to the frequency domain is needed, like the peak picking and line fit method. A disadvantage however, is that it is less accurate. It works best on systems that are slightly damped, also it relies on clear and well-defined peaks, without any rapid decay. The method takes the peak at each oscillation and finds the logarithmic decrement between two consecutive peaks. It is expressed as the natural log of the ratio between two consecutive peaks, as shown in Equation 3.42. The unit of ζ is dimensionless. The eigenfrequency is obtained by simply counting the number of periods and dividing by the total time length of the signal. A more robust method that can be applied is the Fast Fourier Transform (FFT). This method converts the time domain signal to the frequency domain signal by decomposing the signal into a series of sinusoidal components, it reveals which frequencies are present and how strongly they contribute to the overall response [1].

$$\zeta = \frac{1}{2\pi} ln(\frac{x_n}{x_n + 1}) \tag{3.42}$$

4 | Comparative case study of SSPCMs

The next part of this work will consist of two main sections. First a theoretical review of pre-manufactured SSPCMs is performed. Section 4.1 covers an in-depth discussion of the research performed by Spencer Flint from the University of Washington, Seattle. He showed a proof of concept where the material properties can be tuned using different composition of SSPCMs. Flint produced its own samples and tested them using experimental modal testing. His findings are discussed and the most important results are used as a knowledge foundation for the second section of the case study. Section 4.2 presents a re-evaluation and experimental validation of the samples manufactured by Flint using his recommended procedures. The tests were executed on the same samples that Flint originally tested. This reassessment provided a deeper understanding of the working mechanisms of SSPCMs and resulted in fundamental knowledge required to design and develop new SSPCMs.

4.1 Theoretical review of pre-manufactured SSPCMs

A direct implementation of SSPCMs is presented by the Master Thesis of Flint [33]. His study covered the testing of the eigenfrequency and damping for different compositions of SSPCMs. The sample manufacturing and method are discussed, whereafter the results are shown and concluded with a extensive discussion and reflection of the work of Flint.

4.1.1 Sample manufacturing

To find the material properties for different compositions of SSPCMs, two rectangular hollow carbon fibre beams were manufactured consisting of a pre-impregnated carbon fibre laminate with a 2×2 twill weave and a [-45/45/0/45/-45] layup, as shown in Figure 4.1a. The beams are filled with a combination of two different materials to create a SSPCM. The matrix material is a type of tin-catalysed silicone rubber: Mold wax 14 NV [102]. The filler material is a type paraffin wax with a melting temperature between 52 °C and 58 °C. The ratio between the wax and silicone rubber in the first beam is 100/0 % and in the second beam 85/15 %. Other than the two core materials and the carbon fibre shell, the beams also contained a heating strip made out of flexible kapton heaters powered by a DC power supply, as shown in Figure 4.1b. To measure the temperature of the heaters two thermocouples were implemented in the beams. Lastly, to seal of both ends, white plastic caps were added, which were screwed into the carbon fibre beam.

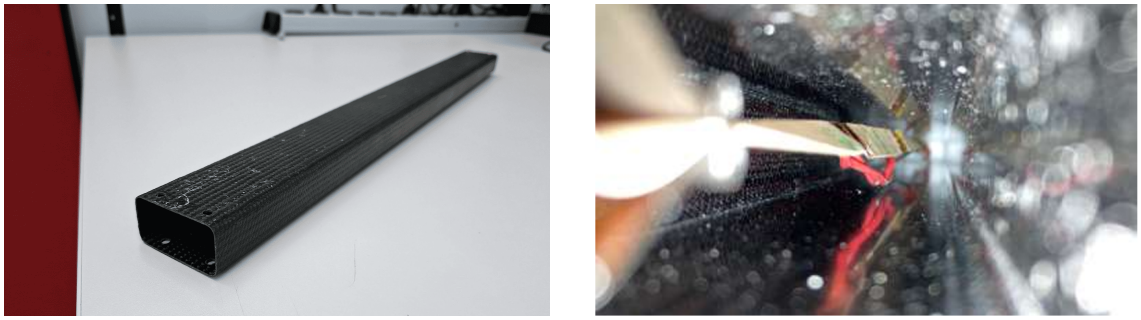

(a) *Close up of the outside of the beam. Shown are the small holes to attach the plastic cap (top and bottom) and the weave pattern of the carbon fibre*

(b) *Close up of the inside of the beam. Shown are the kapton heating elements (light yellow) and power supply (red cable) [33]*

Figure 4.1: *Out- and inside of the tested carbon fibre beams*

4.1.2 Method

The material properties of the SSPCMs were determined using modal testing. In Flints study [33] the structure was excited using an impact hammer test and the corresponding output was recorded using a single accelerometer. The beam was tested in a clamped–free configuration.

The response and excitation signal are measured in the time domain. To investigate the behaviour the signals were transformed to the frequency domain using a FFT, next to obtain the FRF the FFT of the output is divided by the FFT of the input. To extract the eigenfrequency and damping ratio from such measurement, two different methods were used. To find the eigenfrequency the 'modalfit' function from Matlab was used. It uses the Least-squares complex exponential method, which estimates a systems modal parameters by fitting a sum of decaying complex exponentials to a FRF. Using the least squares method, the complex poles are determined, from which the eigenfrequencies can be calculated. Additionally, the logarithmic decrement method was used to determine the damping ratio, as explained in Section 3.5.3.

To test the temperature dependent behaviour of the beams, the temperature was increased from 20 to 55 °C. It was monitored by the two thermocouples and averaged to get the mean temperature of the sample. Ideally, a steady state temperature is reached however, this task demanded significant time and effort. Therefore, only a few data points were obtained for each sample.

4.1.3 Results

The results are divided into two paragraphs the first one discussing the results of the eigenfrequency and the second one the damping ratio.

Eigenfrequency

The results for the eigenfrequency for the two beams are shown in Figure 4.2a. The temperature, ranging from 20 to 55 °C, is depicted on the x-axis, while the y-axis shows the normalized eigenfrequency with respect to the first measurement.

The first beam, with 100/0 % silicone rubber-wax composition and shown in blue, showed a downwards trend with increasing temperature. Over the complete temperature range the eigenfrequency had decreased with 10 %. For the second beam, with a 85/15 % composition and shown in orange, the eigenfrequency stayed within the $\pm$ 5% of the value at room temperature. When compared with the 100/0 % composition the eigenfrequency had increased, so the drop eigenfrequency which was initially created, is now compensated by the wax. The increase in frequency due to the increase in wax content can be explained by two opposing temperature-dependent mechanisms. First, at elevated temperatures, polymers exhibit enhanced chain mobility, which leads to a decrease in stiffness and eigenfrequency, as explained in Section 2.3.1. Second, the opposing mechanism increases the stiffness and is characterized by a high CTE at the melting area of the wax, which results in a significant volumetric expansion. This expansion generates additional internal pressure on the enclosing shell, resulting in an increase in the stiffness of the beam [33]. As these two effects counteract each other, the resulting eigenfrequency remains approximately constant across the examined temperature range.

Damping ratio

The results for the normalized damping ratio are presented in Figure 4.2b. The x-axis is identical to Figure 4.2a and also in this plot the y-axis is normalized. For both samples a clear increasing trend with temperature was observed. The damping for the 100/0 % composition beam had increased by 60 % at 55 °C which is more than the increase of the beam with 85/15 % composition which increased by 45 % at 55 °C. This trend is not only clearly visible at high temperatures but also at low temperatures, the damping of the 100/0 % composition beam is higher than the 85/15 % composition beam. This indicates that increasing the wax content reduces the damping ratio, while increase the temperature increases the damping ratio.

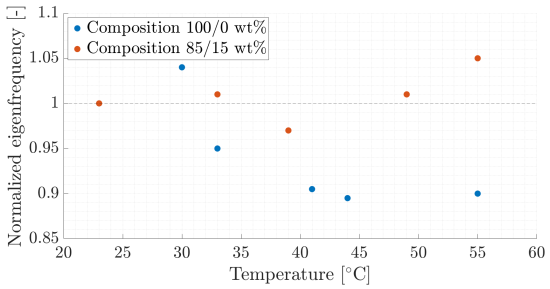

(a) *The normalized frequency of the first mode at different temperatures for different compositions*

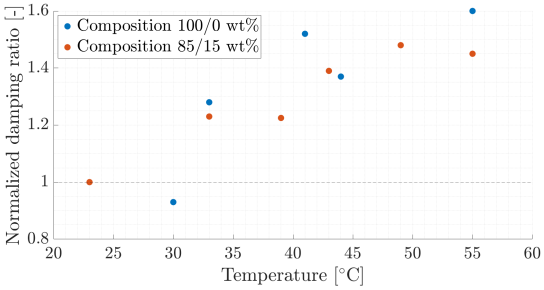

(b) *The normalized damping ratio of the first mode at different temperatures for different compositions*

Figure 4.2: *Comparison of modal parameters between different beam compositions for different temperatures*

4.1.4 Conclusion & Discussion

The study of Flint demonstrated a proof of concept for tunable dynamic behaviour of SSPCMs. Two samples were manufactured with a 100/0 % and 85/15 % silicone rubber-wax composition. A modal test was performed and the modal parameters were extracted using the modalfit and logarithmic decrement method and suggest that there may be a correlation between an increase in temperature and a decrease in the eigenfrequency for the 100/0 % composition. The eigenfrequency dropped by 10 % at elevated temperatures. This drop in eigenfrequency is directly related to a drop in stiffness and may be attributed to the increased chain mobility of the polymer. On the other hand, the stiffness drop is compensated by the thermal expansion of the wax in the 85/15 % beam. The expansion creates additional internal pressure increasing the stiffness. As a result, the eigenfrequency remains constant. The damping ratio showed similar behaviour for both beam compositions, as both damping ratios increase with increasing temperature. The influence of increasing the wax content turned out to work counter intuitive as the 85/15 % composition showed a lower damping ratio than the 100/0 % composition.

These results should be interpreted with caution, because the testing procedure revealed some limitations: First, the dataset was limited, as each measurement contained only 5 to 6 data points. This increases the likelihood of measurement errors and makes it difficult to capture the overall behaviour reliably. In addition, only two beam compositions were tested; to better understand how frequency and damping evolve with increasing wax content, more beams with higher wax fractions should be examined. Additionally, the measurement set up could be adjusted by increasing the number of accelerometers, which could increase the accuracy of the measurements. Furthermore, it was recommended by Flint [33] to change the boundary conditions from fixed–free to free–free, as the fixed–free configuration introduces two major disadvantages. First, clamping reduces the effective beam length and since the eigenfrequency scales with $\frac{1}{L^2}$ (Equation A.8), even a small change in effective length can produce a large shift in eigenfrequency [33]. Second, the clamping condition is inherently unreliable: the stiffness depends on the applied clamping force and the resulting friction, both of which can change during testing as vibrations can gradually loosen the clamp. This makes it difficult to obtain consistent and repeatable measurements.

besides, the improvements in the measurement set-up, also the post processing could be refined. The modal parameter extraction method is now limited to logarithmic decrement method for the damping. A proposed solution is to use a different method like peak picking, inverse method or circle fit method or more advanced methods like the Rational Fraction Polynomial (RFP) and Ibrahim Time Domain (ITD) method [30].

Fourthly, the thermal equilibrium was difficult to reach and maintain by the kapton heaters as no control system was applied to regulate the internal temperature. A solution would be to use a PID controller or a climate chamber that regulates the temperature. Flint proposed the solution to reduce the heating from 1.7 to less than 0.5 °C/min [33].Moreover, the temperature was measured at only two locations, leaving open the possibility that the beam had not reached full thermal equilibrium during testing. So, more thermocouples must be added or a thermal camera can be used.

Lastly, the variation introduced during sample manufacturing can also be reduced. Flint acknowledges that an insufficient mixing temperature leads to large wax clumps, compromising uniformity. The homogeneity of each sample should therefore be verified, for example using microscopy or DSC, to determine the exact composition.

Nonetheless, the findings indicate the potential of SSPCMs for temperature tunable dynamic applications. However, further validation with more controlled experiments is needed to exploit material properties of SSPCMs. The next section will cover the details of a more in-depth test to identify the material characteristics, considering all improvement points discussed above.

4.2 Experimental review of pre-manufactured SSPCMs

This chapter will explore in greater detail the research conducted by Flint. Although, it provided a valuable first exploration into the use of SSPCMs, it did not offer sufficient insight into how the material behaved with changing temperature. As outlined in Section 4.1.4, several limitations were present. Nevertheless, Flint's work forms an essential foundation for further investigation into the underlying physics of SSPCMs. Building on this groundwork, the present study introduces a refined testing approach that examines the same beam compositions while addressing the identified shortcomings. In particular, the limited number of test specimens was addressed by introducing an additional beam with a 80/20 % silicone rubber–wax composition.

First the method of the new test set-up will be presented in Section 4.2.1, followed by the results in Section 4.2.2, which cover various topics like the difference between impact hammer testing and shaker excitation testing on the eigenfrequency and loss factor, different modal identification methods, linearity, etc.

First, the new test set-up is described in Section 4.2.1, followed by the results in Section 4.2.2. These results cover several topics, including the differences between impact hammer and shaker excitation on the effects of eigenfrequency and loss factor, the performance of different modal identification methods and the assessment of linearity.

4.2.1 Method

To extract the material properties from the beam, a different experimental set-up is used compared with Flint's research [33]. A schematic of the setup is shown in Figure 4.3a. This flowchart consists of two main parts, the first part (outside the boxed area) shows the cable management for the signal analysis, the power supply and the sensors. Each sensor (accelerometer, thermocouple, modal hammer, force sensor and shaker) is first connected to a Data Acquisition (DAQ) module. From this module all data is transferred and visualized on the computer. Furthermore the shaker is connected in a loop to the DAQ module and amplifier. Lastly, the thermal camera is

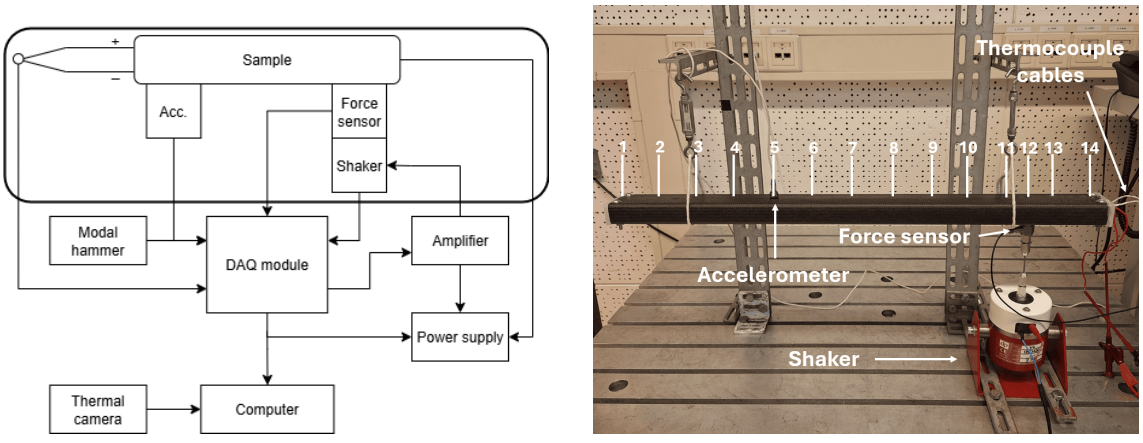

(a) *Schematic of the experimental setup combining*

(b) *Experimental free-free modal test setup with the shaker*

Figure 4.3: *The schematic and experimental setup of the modal test*

connected to the computer to visualize the temperature distribution of the beam, a more detailed explanation about the thermal camera is given in Section 4.2.1. The second part is all about the components inside the boxed area. This part is physically represented by Figure 4.3b. It shows the accelerometer, the force sensor and the cables of the thermocouples. Additionally, it can be seen that the whole structure is mounted on a solid piece of metal to mitigate external vibrations and that the beam is suspended by two strings, to simulate free-free behaviour. The beam was divided into 13 equal segments of 5 cm each, plus one additional node for the excitation location of the shaker.

A schematic representation of the beam is shown in Figure 4.4a, which is not to scale. The green and yellow dots indicate the positions of the thermocouples, with the green dot located near the edge of the beam and the yellow dot positioned at centre of the beam. The white strip represents the kapton heating element, which extends through the middle along the full length of the beam.

Frequency range

Based on the analytically derived EOM, the theoretical eigenfrequencies were calculated using Equation 4.1.

$$\omega_n = (\beta_n L)^2 \sqrt{\frac{EI}{mL^3}} \tag{4.1}$$

This formulation assumes a homogeneous material; therefore, the rule of mixtures is applied to determine the effective stiffness and inertia. The full derivation of Equation 4.1, together with the application of the rule of mixtures, is provided in Appendix A.3. The resulting analytical eigenfrequencies are summarised in Table 4.1.

Table 4.1: *Analytically calculated eigenfrequencies for different silicone rubber-wax compositions*

Sample	**si/wax [%]**	ω_1 **[Hz]**	ω_2 **[Hz]**
Beam 1	100/0	370	1020
Beam 2	85/15	379	1044
Beam 3	80/20	495	1365

The first eigenfrequency was determined between 370 and 495 Hz and the second eigenfrequency between 1020 and 1365 Hz. Since, the interest was only to capture the first eigenfrequency, it was decided to test up to 500 Hz. When the system is freely suspended, the structure will exhibit Rigid Body Modes (RBM). In theory, any structure contains six RBM each at a eigenfrequency of 0 Hz. However, in practice a structure is never completely freely suspended. The supports, albeit very thin strings, add stiffness and damping to the system which increase the eigenfrequencies of the RBM to marginal amount. There is no interest to capture the RBM modes of the system, therefore, the lower bound frequency is set to 50 Hz.

Temperature measurement

The temperature inside the beam is regulated by the kapton heaters. Kapton heaters are voltage controlled; therefore, it is not possible to set an exact temperature but rather a voltage that corresponds to a certain heating rate. The heating rate was set to around 0.10 to 0.15 °C/min, starting at room temperature and ending around 50 to 65 °C.

Flint used the thermocouples inside to monitor the temperature of the beam. However, in beam 1 and 2 the thermocouples malfunctioned and were not labelled, so it was unknown which thermocouple belonged to what temperature. Therefore, a different method was used to capture the temperature behaviour: a thermal camera. A thermal camera measures the infrared radiation, which is emitted by all objects, and transforms this into a temperature-dependent electrical signal and displays this as a thermal image. For this research the ThermalIMAGER TIM 160 from MicroEpsilon is used. This thermal camera has a frame rate of 120 Hz and a measurement range from

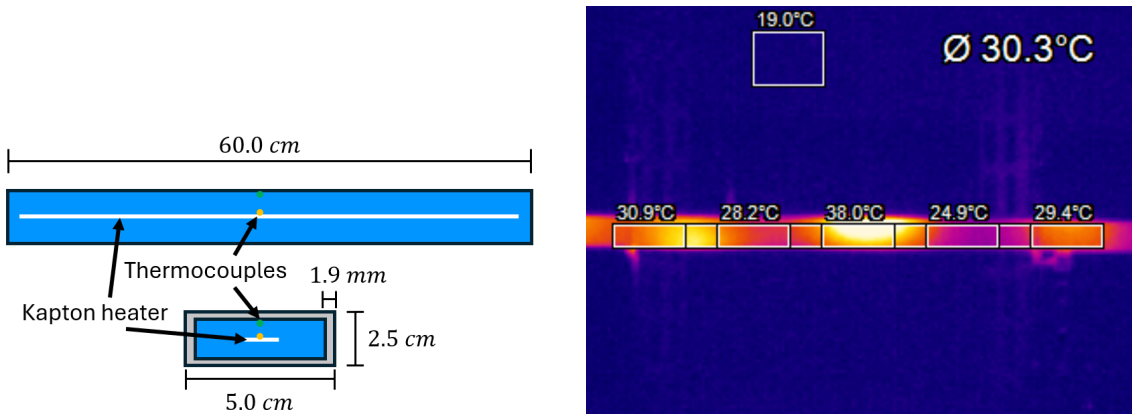

(a) *Schematic representation of the beam dimensions* **(b)** *Temperature distribution of the beam at 30.3 °C*

Figure 4.4: *Schematic representation and temperature distribution of the beam*

-20 °C to 100 °C. The camera was placed 4.5 meters away from the sample to ensure the complete temperature distribution of the beam was captured. An example of such a distribution is shown in Figure 4.4b. In this figure multiple things can be observed. First, the box in the top-middle of the figure indicates the reference temperature and was based on the current room temperature and regularly updated by measuring the room temperature with a pyrometer. Second, five small rectangles can be seen on the sample, each measuring the average temperature of that area. The number displayed in the upper-right corner corresponds to the average temperature across the five rectangles. This averaged value is considered the mean beam temperature for all subsequent analysis in this section. The room was not temperature-controlled and the beam was not placed in a climate chamber, meaning the temperature could not be fully regulated.

Sensors selection

To measure the in- and output signal several sensors were used. It is possible to measure the input force in two ways. The first option is to use a modal hammer, which contains a force sensor with a sensitivity of 21.12 mV/N. The second option is to use a shaker with a sensitivity is 2.5 N, as shown in Figure 4.3b. The output signal or response is measured by an accelerometer, with a sensitivity of 10.53 mV/(m/s^2) and was mounted on the beam at node 5. shown in Figure 4.3b. The sampling rate for the accelerometer and force sensor were both set to 25600 Hz.

Impact hammer testing procedure

The beam is excited using a modal hammer to extract the mode shapes. This is only possible with a hammer test, because exciting multiple points fills an entire row of the FRF matrix, which is necessary to define a mode shape. In contrast, a shaker excites the beam at a single point and therefore provides only one entry in the FRF matrix and cannot be used to extract the mode shapes. After each hit, the response is recorded and three consecutive hits are averaged to obtain the FRF at that node. The hammer is moved to the next node, and the procedure is repeated. Throughout the test, the response location remains fixed at node 5.

All measurements were collected using the in-house software program: sound and vibration measurement system, after which the analysis was carried out either in FEMtools or in Matlab, depending on the objective. Mode shape extraction was conducted in FEMtools, while all remaining analyses were executed in Matlab. To simplify the approach, the sample was not heated and all hammer tests were carried out at room temperature.

Shaker excitation testing procedure

The input for the shaker was set as a sine sweep with a frequency ranging from 50 to 500 Hz. The amplitude was measured in volts and normalized between -1 V to 1 V. This signal is sent to the amplifier, which increases the voltage. The final step is to send it to the shaker, which converts the voltage into a controlled vibration. To improve accuracy of the signal in the time domain, a smooth start stop signal is used. This prevents leakage, reduces noise and makes the signal smoother. The type of shaker used is the Bruel & Kjaer Mini Shaker Type 4810. The duration of the sine sweep, called sweep time, is very important to consider. It is important to check that the steady-state response conditions are reached before the measurement the next measurement is taken. An excessive or a too low sweep rate results in incorrect measurements which do not represent the system. A proper sweep time can be determined using the damping ratio. Theoretically, any sweep time is too fast because it takes an infinite amount of time to reach complete steady state. However, to reach 99 % amplitude, the sweep time can be significantly reduced. A guideline for the linear sweep time is defined in the book of Ewins. For a loss factor ranging from 0.05 to 0.2 and a starting frequency of 50 Hz and ending frequency of 500 Hz, the recommended sweep rate is between 20 and 100 seconds [30]. It was decided to take the middle which is a 60 seconds sweep time.

4.2.2 Results

This section provides an overview of the modal test results for the beams containing SSPCMs. It first compares the similarities and differences between impact hammer and shaker excitation, followed by the extracted eigenfrequencies and damping ratios for the three beams. The subsequent sections serve as validation steps to confirm that the measurements were performed correctly, addressing aspects such as sensor mounting, modal identification methods, antiresonance behaviour, linearity and reciprocity.

Impact hammer testing

The measurement at each node resulte in one FRF, resulting in a total of 14 FRFs. All these FRFs are combined into FEMtools and as a result the standard first bending mode shape could be identified for all three beams, as shown in Figure 4.5. The green arrow indicates the excitation point (node 12) and the blue arrow the response point (node 5). Figure 4.5a shows one irregularity at the response node and this is probably due to poor attachment of the accelerometer leading to a reduced amplitude response.

To compare the hammer test data with the shaker measurement data, only a single FRF from the 14 hammer-based FRFs is used: the FRF corresponding to the same FRF matrix entry as the shaker test, namely the entry at response node 5 and excitation node 12. The comparison of both FRFs is shown in Figure 4.6a. On the x-axis it displays the measured frequency range in Hz, on the left y-axis in blue the inertance and on the right y-axis in orange the coherence ranging from zero to one. It shows minor low-frequency peaks for both the hammer and shaker tests, while the shaker response additionally only shows high-frequency noise. This behaviour is likely related to the stinger, which is intended to operate mainly in axial tension and compression but in practice also bends and vibrates laterally, introducing extra noise.

The coherence plot in Figure 4.6a shows that the impact hammer test achieves consistently higher coherence than the shaker excitation test. This difference arises because the shaker is mechanically attached to the structure and therefore, becomes part of the dynamic system. Such

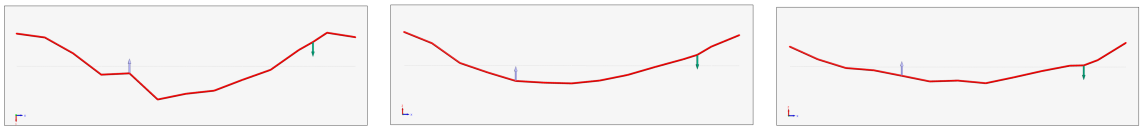

(a) *Beam 1* **(b)** *Beam 2* **(c)** *Beam 3*

Figure 4.5: *Mode shapes of beam 1, 2 and 3 obtained by hammer impact testing*

attachment introduces mass loading, meaning that the additional mass and stiffness modify the dynamics. As a result, the measured response no longer corresponds precisely to the expected response by the applied force, particularly near resonance where the shaker cannot fully follow the motion of the displacement. This mismatch reduces the input–output correlation and leads to lower coherence. In contrast, for hammer impact tests this effect is negligible, because the hammer is in contact with the structure only for a short period of time and therefore, introduces almost no mass loading. As a result, the coherence is very clean and approaches one across the full frequency range.

Further observing Figure 4.6a shows that the first eigenfrequency occurs around 160 Hz, which is why a cropped FRF and coherence over this range is presented in Figure 4.6b. This plot indicates that the shaker produces a slightly lower eigenfrequency and a reduced amplitude compared with the hammer test. This trend is consistent with the values in Table 4.2. This table shows the result of the peaking picking method (PP) for the beams 1, 2 and 3. The first beam shows a first eigenfrequency of 164 Hz for the hammer test and 160 Hz for the shaker test, with the second and third beams exhibiting the same pattern. This behaviour can also be attributed to mass loading: attaching the shaker adds mass to the system, which lowers the natural frequency according to Equation 3.2 and reduces the structural compliance at resonance. As a result, the shaker-based FRF lies lower in amplitude and shifts the eigenfrequency to the left relative to the Impact hammer test.

The experimental eigenfrequencies can also be compared to the analytical predictions, shown in Table 4.1. It reveals a substantial difference for all beams. The analytical predictions for each beam consistently overestimate the measured eigenfrequency by a factor of 2.2. This trend is correctly captured by the rule of mixtures however, it does not accurately predict the absolute material properties and thus eigenfrequencies. This may be caused by insufficient material uniformity inside the beam, leading to a violation of the homogeneous-material assumption.

The damping is now expressed using the loss factor rather than the damping ratio, since this is the standard convention in viscoelastic material characterization. The two quantities are related through Equation 4.2. As long as the damping ratio remains below 0.3, the difference between the two formulations is small and introduces less than 5 % error [31].

$$\eta = 2\zeta\sqrt{(1-\zeta^2)} \approx 2\zeta \tag{4.2}$$

The loss factors obtained from the hammer and shaker tests are summarised in Table 4.2. For beam 1, the shaker test produced a loss factor that is about 7 % higher than the hammer result. In beam 2, both methods yielded the same value and beam 3 showed the opposite behaviour, where the hammer test produced a loss factor approximately 50 % higher than that of the shaker.

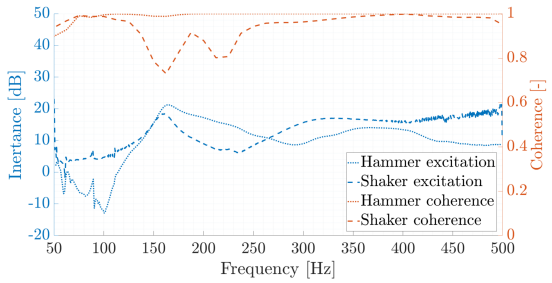

(a) *FRF comparison highlighting the difference between the hammer and shaker excitation measurement in terms of response of coherence*

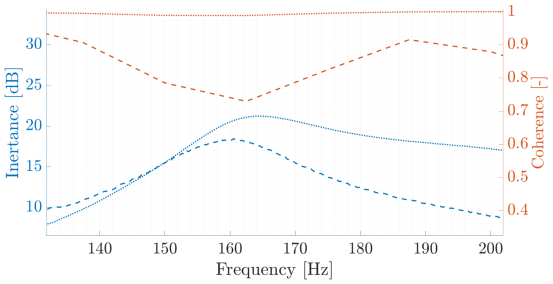

(b) *Cropped FRF around the first eigenfrequency, highlighting the difference between hammer and shaker excitation in terms of response of coherence*

Figure 4.6: *Comparison of the FRFs obtained from hammer and shaker excitation at node 12, measured at response node 5 for beam 1*

Shaker excitation testing

The shaker test involved increasing the temperature inside beam and measuring the temperature with the thermal camera, as explained in Section 4.2.1. To obtain a clearer trend of how the beams behave with changing temperature, measurements were taken at intervals of approximately 0.5 °C. For the first beam, this resulted in 76 FRFs between 20 and 51 °C. For each of the 76 FRF the following modal parameters were extracted: eigenfrequency, loss factor and modal constant. Using these parameters it was possible the synthesize the FRF in the vicinity of the eigenfrequency, as explained in Section 3.5. A similar procedure was used for beam 2 and 3, which have a total of 83 and 102 measurements, respectively.

From all these measurements of beam 1 four FRFs are selected and displayed Figure 4.7. The reference FRF is shown in blue at 20 °C with a clear peak around 160 Hz. Secondly, the FRF with the highest loss factor is shown in orange at 28.8 °C. When, using the peak picking method, the values for ω_a and ω_b are spaced far apart which increase the damping. Additionally, it was found that this FRF had a great antiresonance, shown by the black dots. A relation was observed between an increasing loss factor and a greater antiresonance. An elaborate explanation about antiresonances is given in section 4.2.2. The third and yellow FRF shows the response for 33.7 °C. This temperature showed the highest eigenfrequency at 172 Hz. The damping for this temperature is relatively low and the antiresonance has vanished. Lastly, the purple FRF at 50.5 °C shows the strongest response but not the highest eigenfrequency, this means that the amplitude of the vibration was the highest but the frequency was lower in comparison with the other FRFs. When examining the evolution of the FRFs with increasing temperature, the response amplitude continues to grow.

Table 4.2: *Results of the hammer and shaker test for beams 1, 2 and 3 at room temperature.*

Beam	Excitation	ω_n [Hz]	Loss factor [-]
1	Hammer (PP)	163.9	0.122
1	Shaker (PP)	160.3	0.131
2	Hammer (PP)	174.1	0.0890
2	Shaker (PP)	172.6	0.0856
3	Hammer (PP)	219.8	0.0528
3	Shaker (PP)	214.0	0.0267

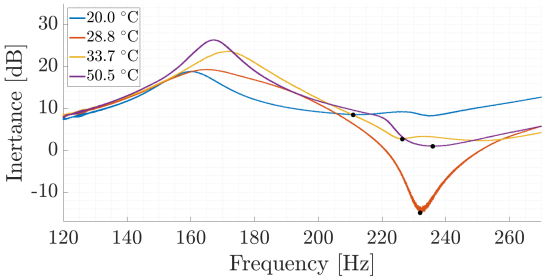

Figure 4.7: *Selected FRFs of beam 1 for different temperatures.*

Eigenfrequency

The eigenfrequency results are shown in Figure 4.8a, which presents the normalized eigenfrequency of the three beam compositions on the y-axis as a function of the mean beam temperature on the x-axis, obtained using the peak-picking method. The normalization is based on the first measurement of each beam. Beam 1 shows a pronounced increase, reaching a maximum increase of approximately 8 % (roughly 12 Hz) near 32 °C, followed by linear decline with a slope of about -0.36 Hz/°C, ending at around a 4 % increase at 50 °C. Beam 2 follows a similar trend but with a lower peak of about 5 % (roughly 9 Hz) near 29 °C and a steeper post-peak decrease of approximately -0.49 Hz/°C, resulting in eigenfrequencies that fall below their initial value at higher temperatures. In contrast, Beam 3 does not exhibit a peak. Instead, the eigenfrequency decreases linearly across the entire temperature range with a slope of -0.16 Hz/°C, corresponding to a total reduction of 2.7 %.

Beam 1, which has no wax content, shows a higher increase in eigenfrequency than beam 2 and 3. This indicates that adding wax does not increase the eigenfrequency. The silicone rubber already provides enough tunability of the eigenfrequency, adding wax seems to have a counterproductive effect. Also, adding wax seems to first shift the peak for maximum increase of eigenfrequency to the left but when the wax content is further increased this trend is not continued.

All measurements were performed in duplicate to ensure reproducibility. This resulted for beam 1, prior to the peak, in minor deviations of around 3 Hz. However, beyond the peak, the measurements converged and follow a single consistent trend. Beam 2 and 3 show identical results for the duplicate runs already from the beginning.

Loss factor

Figure 4.8b presents the temperature-dependent evolution of the loss factor, using the same temperature axis as before but now showing the normalized loss factor on the y-axis. Several observations can be made. Beam 1 shows the highest initial loss factor, which increases by approximately 50 % to a maximum of 0.118 at 29 °C. Beyond this point, the loss factor decreases linearly and drops below its initial value at around 39 °C, after which it stabilizes at roughly half of the original value. There are small differences between the duplicate measurements. Although the curves diverge slightly after the peak, they follow the same overall trend.

A similar observation is made for beam 2, in absolute terms it starts a little lower at 0.0627, but has a bigger maximum relative increase than beam 1, which is 150 % increase in loss factor at 25 °C. Next, the slope of the loss factor increases with the same rate as it decreased before, to half of the initial value at 31 °C and remains constant for the remainder of the measurement. For beam 2 all the duplicate measurements are on the exact same line.

A similar trend is observed for beam 2. The initial loss factor is slightly lower at 0.0627, but it shows a larger relative increase than beam 1, reaching a maximum of about 250 % at 25 °C. Thereafter, the loss factor decreases with approximately the same slope as during the initial rise, reaching half of the initial value at 31 °C, after which it remains constant for the rest of the measurement range. For beam 2, the duplicate measurements coincide almost perfectly.

Just like with the eigenfrequency, the loss factor of beam 3 shows behaviour distinct from that of beams 1 and 2. The initial loss factor is around 0.03 and increases only slightly over a span of 30 °C. Above 50 °C however, the slope changes and a strong increase in damping is observed, with the loss factor increasing by nearly 250 percent at 66 °C. The duplicate measurements exhibit the same overall behaviour.

In summary, beam 1 shows the highest absolute loss factor, consistent with the inherently high damping capacity of silicone rubber also reported by Flint [33]. However, the largest relative increase in damping occurs in beam 3, which has the highest wax content, followed by beam 2. These results indicate that adding wax enhances the relative damping capacity but does not increase the absolute damping level.

Upon comparing the trends of the eigenfrequency and loss factor it shows that the loss factor always peaks a three to four °C earlier than the eigenfrequency for beam 1 and 2. This can be seen as a kind of delayed response, where first the damping increases and then the eigenfrequency.

In most cases, the damping increases as the temperature approaches the glass transition tem-

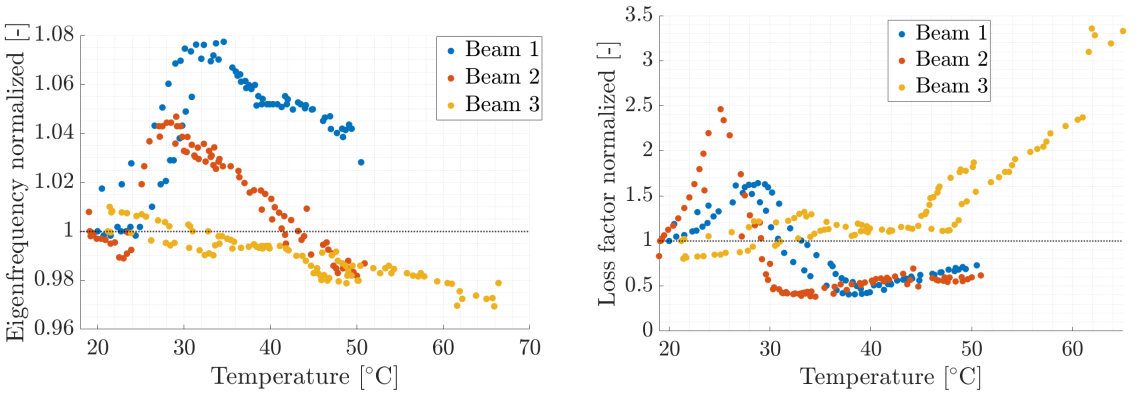

(a) *The eigenfrequency results of the modal testing for different temperatures*

(b) *The loss factor results of the modal testing for different temperatures*

Figure 4.8: *Results of the modal testing with changing temperature for beams 1, 2 and 3*

perature. Mold Max 14 NV has a glass transition temperature near -120 °C, while paraffin wax typically lies between 45 and 62 °C. In the results however, a peak appears at 31 °C for beam 1 and at 25 °C for beam 2. These temperatures do not coincide with the expected glass transition range and therefore, cannot be explained. Beam 3 shows a melting area between 55 and 65 °C which could come from the molten wax.

Verification of measurement repeatability for accelerometer mounting

During some measurements, it was found that the accelerometer did not stick properly once the beam was heated. The mounting wax used to attach it to the beam began to lose stickiness around 35–40 °C, causing poor contact and increased noise. To check whether this affected the modal parameters, a second accelerometer was installed using a high-temperature epoxy. This sensor was placed directly next to the wax mounted accelerometer, ensuring both were located on the same longitudinal 2D plane. A schematic of the sensor placements is shown in Figure 4.9a.

At high temperatures there were two types of FRFs. First, one where two sensor mounting configurations showed no difference in eigenfrequency, with a deviation of only 0.2 Hz (0.10 %) and also the loss factor also differed only marginally between the two configurations, with a maximum deviation of 0.013 (2.6 %). And second, one where the wax-mounted sensor exhibited significant noise across the entire spectrum, as illustrated by the blue FRF in Figure 4.9b.

At higher temperatures, two distinct types of FRFs were observed. In the first case, the two sensor-mounting configurations produced nearly identical results: the eigenfrequency differed by only 0.2 Hz (0.10 %) and the loss factor showed only minor variation, with a maximum deviation of 0.013 (2.6 %). In the second case, the wax-mounted sensor exhibited substantial noise across the entire spectrum, as shown by the blue FRF in Figure 4.9b. The distorted response leads to an underestimation of the damping in the synthesized FRF, visible as the sharp orange peak, whereas the FRF obtained with the epoxy-mounted sensor (yellow) shows minimal noise and produces a synthesized FRF (purple) that more accurately fits the measured data.

The results shown in Figure 4.9b apply to beam 3 and it was decided to use the epoxy-mounted sensors in the remainder of this research because the provided more consistent measurements than the wax-mounted sensor. For beam 1 and 2, the noise at high temperatures was minimal and the wax-mounted sensors were used instead.

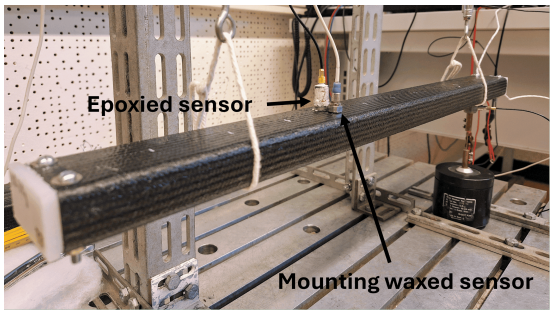

(a) *Sensor mounting on the beam with mounting wax on the right and epoxy on the left*

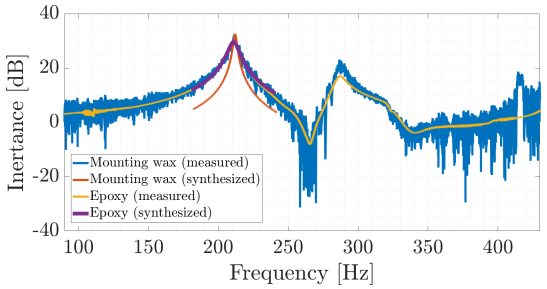

(b) *Measured and synthesized FRF at 38.4 °C for both sensor mounting types*

Figure 4.9: *Comparison between mounting wax and epoxy for sensor attachment*

Different modal identification methods

To verify the modal parameters, three methods were applied: the peak-picking (PP) and line-fit (LF) method described in Sections 3.5.1 and 3.5.2 and the Complex Mode Indicator Function (CMIF), as implemented in Femtools. The CMIF is based on singular value decomposition of the FRF matrix and is a more sophisticated but computationally heavier model than the peak picking and line fit method [30]. Figure 4.10a shows the absolute eigenfrequency against temperature for the CMIF, PP method and LF method. The eigenfrequency of the PP method matches very well with the CMIF with average difference of 0.20 Hz. Similarly to the LF method, which showed an average difference of 0.23 Hz.

Figure 4.10b shows the loss factor and it is immediately evident that the PP and LF method yield lower values for the loss factor compared with the CMIF results. On average this is 0.0075, which is equal to 16 %. This behaviour is more often observed and explained in literature. It boils down to the fact that the CMIF method evaluates the complete FRF matrix, meaning it incorporates both the diagonal and off-diagonal terms. In contrast, the PP and LF method rely on a single FRF and therefore, assume that each resonance behaves as an isolated SDOF system. This assumption breaks down when modes are not well separated or when damping is moderate. When this happens, the modal contributions from adjacent modes broaden the resonance, but this broadening is not captured by a single FRF. As a result, the resonance becomes narrower, leading to an underestimate in the damping for the PP and LF method [30].

Since the CMIF approach requires each FRF to be imported into FEMtools individually, applying it to the complete set of measurements was considered too time-consuming. Therefore, the PP method was found to be accurate enough and will be used as the modal parameter extraction method.

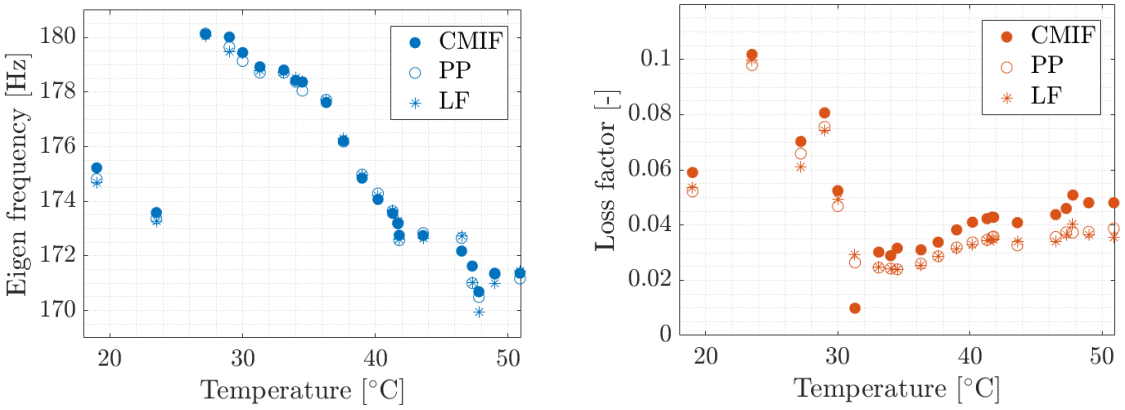

(a) *Eigenfrequency of the CMIF, PP and LF method*

(b) *Loss factor of the CMIF, PP and LF method*

Figure 4.10: *Comparison of different modal parameter extraction methods for different temperatures for beam 1*

Antiresonances

Antiresonances were shown by the black dots in Figure 4.7. It shows on the x-axis the beam length, while the y-axis shows the normalized vertical displacement. The beam is divided into 13 nodes, spaced five cm apart plus one red node for the excitation point and a blue node for the response point. The tilted FRF, plotted at the right, shows the ratio of the response of the blue node over the excitation of the red node. Each resonance peak corresponds to an eigenfrequency of the beam and is associated with a specific mode shape. The first resonance peak (top graph) represents the ideal first bending mode shape occurring at the first eigenfrequency. At this frequency, the magnitude is the highest because the excitation is high and response low. As the excitation frequency increases past the first resonance, the beam begins to vibrate in second mode shape (bottom graph). Between the resonance peaks however, a distinct dip appears; the antiresonance. At this frequency the beam does not vibrate in a single mode shape but rather in arbitrary com-

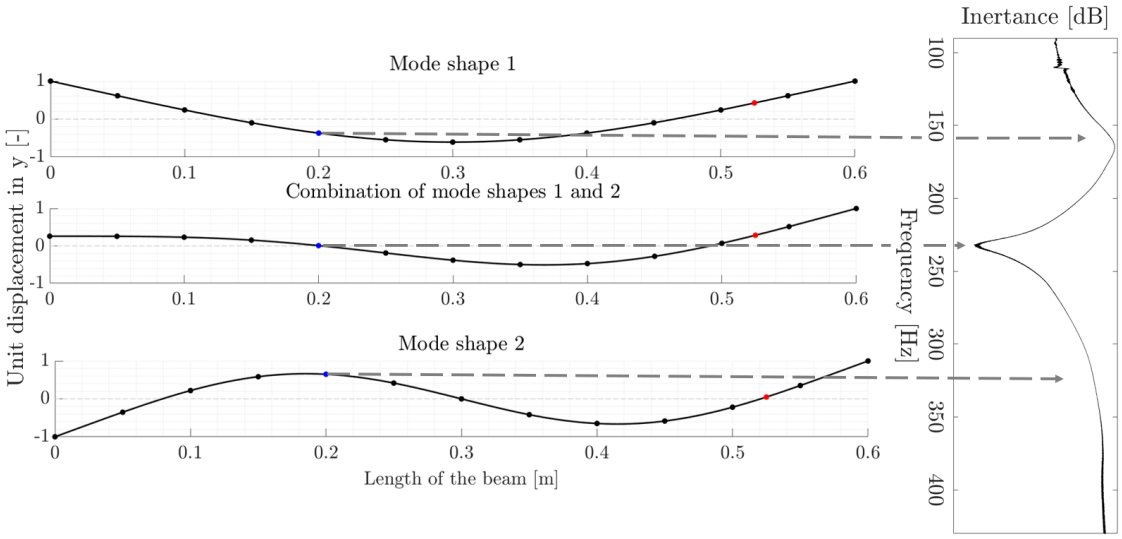

Figure 4.11: *Visual representation of antiresonances in a dynamic system*

bination of the first and second mode shape. Due to the specific amplitude relationships between these modes, the contributions at the response node cancel, resulting in nearly zero displacement. This behaviour is clearly visible in the middle graph of Figure 4.11 where the blue dot indicates near zero displacement. Mathematically, antiresonances occurs when the numerator in Equation 3.28 becomes zero, implying a cancellation of the modal contributions of the eigenvectors.

It is important to emphasize that Figure 4.11 provides an idealized, simplified representation. In practice, as shown in Figure 4.5, the measured mode shapes include contributions from higher-order modes and effects due to non-proportional damping. As a result, zero displacement of a node at an antiresonance is an idealization.

Linearity

To verify the linearity of the system, a modal hammer test was executed where three different levels of excitation were applied: soft, middle and hard. Consequently, each FRF was plotted and it was verified if there was any differnce. The results are shown in Figure 4.12a. The x-axis shows the frequency in Hz, but the y-axis displays the linear inertance in 1/kg. Using a linear scale makes it easier to directly compare two levels of excitation level. As expected, the soft excitation results in the lowest response and the hard excitation in the highest. At low and high frequencies all 3 levels of excitation have a similar response magnitude, where the inertance only differs about 0.5 1/kg. The biggest difference occurs at the eigenfrequency where the difference between the soft and hard excitation is 1.5 1/kg, due to this small difference the system is assumed to be linear. It is expected that the deviation is greatest at the resonance because non-linear effects are most pronounced when the system oscillates at large amplitudes [65]. Also, adjusting the excitation force changes only the response amplitude and not the eigenfrequency itself.

Reciprocity

Next, it is important to verify the reciprocity of the system. It helps so simplify the measurements as it allows the excitation and response locations to be interchanged. To check the system for reciprocity, beam 3 is excited using a modal hammer at node 5 and the response is measured with an accelerometer at node 6 and vice versa. The resulting two FRFs are shown in Figure 4.12b. The difference is very little even at the eigenfrequency where the maximum difference is less than 0.30 1/kg. Therefore, reciprocity for beam 3 is considered valid. Although no explicit linearity or reciprocity tests were performed for beams 1 and 2, it is assumed that the same conclusions apply to them as well, since all three beams are made from similar materials.

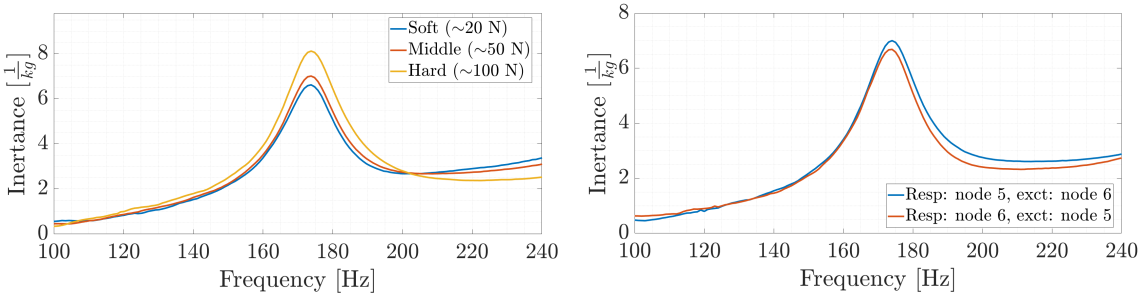

(a) *Verification of the linearity at three different levels of excitation*

(b) *Verification of the reciprocity by switching the response and excitation location*

Figure 4.12: *Verification of the linearity and reciprocity*

4.2.3 Conclusion & Discussion

The reassessment of the study of Flint demonstrated a refined testing of the modal parameters of SSPCMs. Three different silicone rubber-wax compositions have been evaluated using an impact hammer and shaker excitation test by increasing the temperature from 20 °C to 62 °C. The modal parameters were extracted using EMA, which involved 3 different methods: peak picking method, line fit method and complex modal indicator function. The results revealed that the shaker test produced lower eigenfrequencies than the hammer, due to the mass loading of the shaker. Additionally, beam 1 showed the highest relative increase of 8 % of all beams. This behaviour is unexpected, since beam 1 contained did not contain any wax, it appears that the silicone rubber already showed good tuning capabilities for the eigenfrequency. Beam 2, while containing wax, showed a limited change in frequency only about 5 %. Beam 3, did not show any tuning capabilities as the eigenfrequency only decreased with temperature.

The tested SSPCMs suggested a general trend in which higher wax content leads to a higher relative loss factor. However, no decisive conclusion can be drawn regarding the temperature at which the maximum loss factor occurs, as this behaviour is not consistent across the beams. Beam 2 exhibits an early increase in damping, whereas beam 3 shows an unusually late peak at 60 °C, which may not accurately reflect the behaviour.

This makes it essential to evaluate the findings carefully, especially for beam 3, as a 5 % increase in wax content would not normally produce such a large change in response. First, the significantly lower weight suggests that the actual composition may deviate from the intended composition, these inconsistencies limit the certainty of the measurements. It is also unexpected that the damping peak occurs at a much higher temperature than in the other beams, which may be explained by a non-homogeneous temperature distribution caused by misalignment of the kapton heaters. The thermal camera observed only one side of the beam, a heater positioned closer to that face could lead to an overestimated temperature. This was confirmed in one of the tests where a side-to-side difference of about 20 °C was found.

Secondly, the carbon fibre shell introduces extra uncertainty in the measurement, because the resin and fibres show temperature-dependent properties which are not considered in the analysis. Therefore, an improvement would be to only consider the matrix and filler system without any additional encapsulation.

Lastly, achieving thermal equilibrium turned out to be difficult because of the substantial amount of thermal mass of the beam and the uneven heat distribution caused by the internal heater, especially when it was aligned in the middle. A practical improvement would be to reduce the thermal mass and apply external heating.

Since all these limitations cannot be resolved with the current samples, they are not considered further. The next part of this work will focus on the design, manufacturing and characterization of new SSPCMs.

5 | Development & Design of SSPCMs

This section covers the manufacturing, testing and evaluation of in-house manufactured SSPCMs. The work carried out by Flint forms the foundation for this research. The proof of concept developed in the previous sections of the report serve as the basis for development and design of the SSPCMs.

To determine the fundamental properties of the SSPCMs, the focus of the report was redirected. Whereas experimental testing provides insight into the behaviour of complete structures, the objective here is to understand the behaviour of the individual constituents and their interactions. For that reason, the emphasis shifted from experimental modal testing to material characterisation at the local level.

In the research of Flint only the silicone rubber-wax composition were considered as SSPCMs. However, there are more material combinations that can be used as SSPCMs. To find these new combinations a list of requirements is made based on the literature study and the knowledge obtained from the case study. The new SSPCMs will consist of the matrix and filler material, each with its own function and set of requirements. The requirements for the matrix material are presented in Section 5.1, followed by the requirements for the filler material in Section 5.2. Section 5.3 then describes how these materials are combined to manufacture the in-house SSPCM samples. The testing procedure for evaluating the samples in the DMA machine is explained in Section 5.4, and the corresponding results are discussed in Section 5.5. Finally, Section 5.6 provides the overall conclusions.

5.1 Matrix material selection

The main goal of the matrix material is to hold the filler material. The list below elaborates on the design requirements for the matrix material, defined using the SMART formulation.

- The matrix material must remain functional within a operational temperature range of -50 - 130 °C throughout the operational lifetime of the material. The lower limit reflects the requirement for performance in cold aircraft environments, while the upper limit ensures that the matrix can retain the core material at elevated temperatures [105].
- The matrix material must have an elongation at break of at least 25 % in the operational temperature range from -50 to 130 °C, ensuring sufficient space to accommodate the thermal expansion of the filler material without breaking throughout the service life of the material [116].
- The matrix material must have a stiffness below 1 GPa at 20 °C, ensuring that the addition of the filler material results in at least a 30 % increase in stiffness over the operational temperature range.
- The matrix material must have a thermal conductivity of at least 5 W/mK, ensuring sufficient heat transfer is possible to support phase change of the filler material throughout the operating temperature range.
- The matrix material must be manufactured from a castable material. Using custom-designed moulds simplifies fabrication, allowing accurate shaping within 1 % accuracy and consistent reproduction without the need for additional machining.
- The matrix material must not cost more than 50 €/kg.

Additionally, the matrix material must not be harmful to humans (not poisonous or toxic), widely available and have low chemical reactivity with other materials.

After an investigation of the possible materials that fulfil the above-mentioned requirements, three possible materials were found: epoxy, polyurethane and silicone rubber. The material properties of epoxy will be explained in section 5.1.1 and the properties of polyurethane in Section 5.1.2. The properties of silicone rubber have already been discussed in Section 2.2 and only a summary of the material properties is shown Table 5.2.

5.1.1 Epoxy

Epoxy, is a thermosetting polymer consisting of 2 benzene rings combined by 2 methyl groups and 2 oxygen atoms, called the epoxy resin group. The resin adds stiffness and determines the viscosity of the cured epoxy. It reacts with a hardener and cures under room temperature forming a cross-linked 3-dimensional network. The hardener determines the cure speed and the ductility of the cured material. By adjusting the ratio of resin and hardener, epoxies can be tailored to achieve specific material properties for different applications. These range from surface coatings and counters to fast curing sealing epoxies and deep-pour epoxies used in marine structures. Epoxy also offers several more advantages, including low moisture absorption, high tolerance and a predictable, linear curing behaviour [88].

The service temperature refers to the range where the material can maintain its properties without significant degradation. Extended exposure to temperatures outside the regime may results in irreversible damage. For epoxy it is dependent of the exact type. The most general epoxies can serve between -50 °C and 60 °C, which does not full fill the requirement. As a results high temperature resistant epoxies are used, which can handle up to 250 °C. The maximum service temperature is limited by and typically set somewhat below the glass transition temperature.

A lower cross-linking density in the epoxy results in a reduction of the tensile strength and an increase in the elongation at break. This occurs because fewer cross-links create a more flexible polymer network with greater chain mobility, allowing the material absorb more energy before failure. So there is trade-off between tensile strength and elongation at break. In this case, the elongation at break is more important than the tensile strength therefore, an epoxy with low cross-linking density is preferred [64]. The cross-linking density is a key factor determining the Young's modulus, since a higher degree of cross-linking restricts molecular chain mobility and thereby increases the modulus [20].

The thermal conductivity of unfilled epoxies is generally very poor and do not exceed 0.2 W/mK, a proposed solution is to add heat conductive fillers, this can extend the thermal conductivity range to 35 W/mK. The thermal conductivity is also strongly influenced by the cross-linking density. A higher degree of cross-linking reduces the free volume, which results in tighter packing of the polymer chains and therefore increases thermal conductivity. This effect was also demonstrated in the work of Struzziero et al. [106].

Epoxies are suitable for casting because they are, before curing, in a low to medium viscous state, which allows them to fill moulds accurately and reproduce fine geometries. Their low curing shrinkage, typically in the range of 1–2 percent, further supports dimensional stability. However, successful casting requires control of the heat build-up as curing epoxy is a exothermic reaction. An excessive release of heat may result in cracks of internal defects in the final part [86].

A summary of all the above discussed material properties is seen in Table 5.1.

5.1.2 Polyurethane

The second option is to use polyurethane (PU) or to be more specific a thermoset polyurethane elastomer. It is manufactured from an isocyanates, called the hard component, which is composed of 2 benzene rings connected by an alkane and ($-N = C = O$) at either ends. It is mixed with a polyol group, called the soft component, which is composed of an alkene with multiple OH groups. The result is an alternating block polymer with soft and hard chain segments. By altering the ratio of hard and soft components the desired modulus, elongation and thermal expansion can be achieved [35]. Increasing the soft components increases the elongation while more hard components can be used to increase the stiffness.

The castability of PU is good, because before curing, the components show low viscosity such that the mixture can easily flow into the moulds. During the cure the PU shows limited shrinkage

of 0.5 % which is less than the shrinkage of epoxy [107]. Additionally, PU also shows an exothermic reaction, but less heat is released in comparison with the epoxy, resulting in a higher quality product.

The service temperature is between -65 °C and 110 °C. It is important that PU can withstand temperatures above service temperature without irreversible damage, but only for a short period of time [77].

PU has a very wide variety of applications some examples are the usage in seals, hoses, shoe insoles, sport equipment or rollercoaster wheels. Additionally, PU has been extensively used in applications which require damping capacity, for example PUR foam in house insulation and dampers in cars to reduce engine noise [43]. Researchers are actively tuning PU composition to enhance vibration absorption; they showed that by using different types of PU polymers the damping characteristics are additive [44]. An increase in damping is caused by increasing the amount polyol components (OH bridges), these bonds restrict the chain movement, overcoming this restriction dissipates large amount of energy and increases damping [44]. Other research showed that the narrow range of high damping, which is typical for PU, can be broadened. This is achieved by increasing the amount of imine bonds. Imine bonds are dynamic covalent bonds ($= C = N-$) which can reversibly break and reform at increasing temperature. Each time a bond breaks it absorbs energy from the system. When it reforms, some of the energy is needed to make the bond again, but the majority is dissipated as heat. This cycle starts at high temperatures, so just when the damping from the hydrogen bonds decreases due to high temperature the imine bonds start to break and reform increasing the damping. Ultimately, this results in a broadened temperature range of the damping [11, 44].

A summary of all the above-mentioned material properties are shown in the third column of Table 5.1. Considering all properties a choice has to be made about which material will function as the matrix material. After weighing all advantages and disadvantages, it was decided that silicone rubber will be used. The main reason having a very high elongation at break, so the silicone rubber can accommodate all thermal expansion and its very low shrinkage which will provide accurate shaping of the samples. The specific type used is Dragon Skin^{TM} 30 from smooth-on [101].

Table 5.1: *Comparative overview of the potential matrix materials and their key thermophysical properties*

Property	**Epoxy**	**Polyurethane**	**Silicone Rubber**
Young's modulus [MPa]	1000 – 2000 [55]	6 – 35 [26, 74]	0.5 – 5 [32, 101]
Tensile strength [MPa]	7 – 20 [55, 64]	25 – 30 [23, 26, 83]	3.5 – 10 [18, 101]
Elongation at break [%]	50 – 200 [55, 64]	300 – 700 [23, 26, 83]	300 – 1000 [18, 101]
Service temperature [°C]	-50 – 250 [19, 50]	-65 – 110 [23, 34]	-60 – 230 [24, 85]
Glass transition temperature T_g [°C]	42 – 80 [19, 75]	-46 – -35 [10, 74]	-120 – -100 [56, 81]
Thermal conductivity [w/mK]	0.1 – 35 [29, 75]	0.13 – 0.29 [21, 74, 112]	0.2 – 0.8 [54, 99, 109]
Hardness [Shore]	$>$ 60 D [73]	70 – 80 A [21, 23, 26]	10 – 30 A [101]
Cure shrinkage [%]	0.5 – 1 [4]	0.15 – 0.5 [100, 107]	$<$ 0.1 [101]

5.2 Filler material selection

The main goal of the filler material is to leverage its great thermal expansion upon phase change to alter the material properties. The points below detail the filler material requirements, each defined using the SMART framework.

- The filler material must have an average linear CTE of 300 ppm/K over a temperature range $\pm$ 15 °C of the melting point of the filler material.
- The filler material must have a thermal conductivity of at least 5 W/mK, ensuring sufficient heat transfer is possible to support phase change throughout the operating temperature range.
- The filler material must remain reversible without the loose of more than 10 % of the mechanical performance.
- The filler material must have a solid to liquid phase transition between 30 °C and 80 °C, verified by DMA measurements.
- The filler material must remain fully solid at standard atmospheric conditions with no detectable softening.
- The filler material must not cost more than 30 €/kg.

Additionally, the filler material must not be harmful to humans (not poisonous or toxic), widely available and have low chemical reactivity with other materials.

After considering the requirements for the filler materials, two possible groups of candidates were found: inorganic metallics and paraffin waxes. The inorganic metallics are discussed in Section 5.2.1, the properties of paraffin waxes have been extensively discussed in Section 2.1 and therefore, section 5.2.1 will only provide the material properties in Table 5.3 and a comparison with inorganic metallics.

5.2.1 Inorganic metallics

An inorganic metallic is a mixture of two or more materials which have a lower melting point than the individual components. There is a ratio of the two materials where the lowest possible melting point occurs, this is called the eutectic point. At this point the individual components of the metallic do not separate into individual components and are still miscible. A table with possible inorganic metallics is shown in Table 5.2 and will be compared with the material properties in Table 5.3 of possible paraffin waxes. Comparing the two material classes reveals several clear distinctions. The metallics show densities that are roughly an order of magnitude higher than those of the paraffin waxes, when applied in aircraft applications a higher mass is undesired. Melt temperature is also an important factor. Most inorganic metallics fall outside the desired melting range, with only Field's metal meeting the requirement, whereas both paraffin waxes show suitable melting areas satisfying the requirements. A major advantage of the inorganic metallics is their much higher thermal conductivity compared with the waxes, often by a factor of 50 to 100. This eliminates the issue of poor heat conduction typically associated with SSPCms. Despite this, the thermal expansion of the metallics remains lower than that of the waxes, but still great enough to generate useful thermal expansion. The primary drawback of most inorganic metallics is their toxicity. Several of the shown composition's present health risks, where prolonged exposure to fumes can irritate the skin and eyes. LM95, in particular, contains lead, which can cause neurological damage. Finally, inorganic metallics are substantially more expensive than paraffin waxes, which further reduces their suitability for large-scale SSPCM implementation.

After evaluating all relevant material properties, the benefits of paraffin waxes were found to outweigh those of the inorganic metallics. In particular, the health risks associated with several metallics and the lower thermal expansion were important factors. The high thermal conductivity of the alloys was not sufficient to compensate for these drawbacks. Hard paraffin wax was selected as the preferred PCM [14], as it provides a higher CTE, greater volumetric expansion and is easier to process and mix than soft paraffin wax.

Table 5.2: *Overview of potential inorganic metallics and their key thermophysical properties*

Property	**LM95** [28]	**LM138** [27]	**Field's metal** [66]	**Galinstan** [82, 90]
Composition [wt%]	52.5 Bi / 32 Pb / 15.5 Sn	58 Bi / 42 Sn	32.5 Bi / 51 In / 16.5 Sn	67 Ga / 20.5 In / 12.5 Sn
ρ **[kg/m^3]**	9.7E3	8.6E3	7.9E3 [89]	6.36E3 [22]
T_m **[°C]**	95	138	62	10
λ **[W/mK]**	∼19	∼21	19–28	∼24
α_v **[ppm/K]**	∼500	∼400	∼286 [67]	∼13.1
Health risks	Contains Pb (toxic)	No	May cause burns	Corrosive to Al
Price [€/kg]	∼55	∼69	>50	∼640
Application	Soldering and moulding	Soldering and moulding	Die casting [49]	Heat transfer fluids

Table 5.3: *Overview of paraffin wax and their key thermophysical properties*

Property	**Soft paraffin wax** [114]	**Hard paraffin wax** [114]
Composition [wt%]	Mix of C20–C30	Mix of C30–C40
ρ **[kg/m^3**	0.79E3–0.91E3 [16]	0.88E3–0.95E3 [16]
T_m **[°C]**	45–55	52–62
λ **[W/mK]**	0.19–0.35* [16, 37, 38, 58, 72, 92]	
α_v **[ppm/K]**	400–2000* [58, 71, 108, 111]	
Health risks	Flammable	Flammable
Price [€/kg]	10–15	10–15
Application	Cosmetics	Candles

*Temperature dependent

5.3 SSPCMs sample manufacturing

After the materials for the matrix and filler have been selected, it was time to manufacture the SSPCMs required for the DMA. It was initially unknown which geometry would yield the most reliable results in the DMA, so three different sample types were produced: tensile, compression and three-point bending specimens. The corresponding dimensions for each type were determined based on the manufacturer's specifications of the DMA instrument provided in Appendix A.4. A fourth sample was also manufactured for testing in the TMA machine; however, the machine was later found to be out of service and no measurements could be performed.

Casting was selected as the manufacturing technique due to its simplicity and efficiency, despite the need for a dedicated mould. A custom mould capable of producing all four sample types at once was therefore, designed and 3D printed. PET-G filament was used instead of standard PLA because the mould needed to withstand temperatures up to approximately 60 °C, which corresponds to the glass-transition temperature of PLA. The final design is shown in Figure 5.1a, it also shows the corresponding samples for each test configuration.

Following the work of Flint, the range of wax contents in the samples was extended to further investigate the influence of wax concentration on the overall material properties. Flint tested three silicone rubber-wax compositions of 100/0 %, 85/15 %, and 80/20 wt%. In this study, an

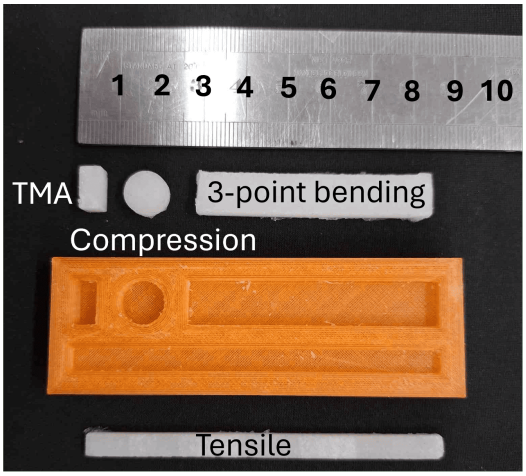

(a) *3D printed mould with the corresponding samples*

(b) *Au-bain-marie setup used to melt the wax. The large pan contains hot water; the smaller pan contains the liquid paraffin wax*

Figure 5.1: *Preparation steps for manufacturing the silicone rubber–wax samples*

additional composition of 70/30 % and 50/50 % was included to broaden the range, the 80/20 % composition was removed. Increasing the wax content to 70 % or higher resulted in samples with poorly defined geometries and unstable composition, also samples consisting of 100 % wax were found not viable for testing because they were too brittle to remove from the mould and would completely melt when tested above melting temperature. Table 5.4 show a summary of the composition, in the remainder of this work, these compositions will be referred to as sample S1, S2, S3 and S4.

The S1 samples were manufactured by mixing the A and B component of the Dragon Skin silicone rubber in a 1:1 ratio to form the final elastomer. The mixture was poured into the moulds and levelled at the surface, after which any excess material was removed.

For samples S2, S3 and S4 an additional step was required. Since the wax must be in a liquid state to mix with the silicone rubber, it was melted using an au-bain-marie construction to prevent the wax from burning, see Figure 5.1b. The temperature was monitored with a thermometer throughout the process to find melting area. Once fully melted, the wax was combined with the liquid silicone in the prescribed ratios in Table 5.4 using scales and syringes and mixed for at least two minutes to obtain an uniform suspension. Each composition was then poured into separate moulds. In total, four moulds were printed so that all samples could cure simultaneously. The curing procedure consisted of 16 hours at 23 °C, followed by a post-cure at 23 °C for 7 days to ensure optimal material properties. After curing, the samples were carefully demoulded using a small knife.

The final results of the sample manufacturing is four different samples with four different compositions.

Name	Silicone composition [wt%]	Wax composition [wt%]
S1	100	0
S2	85	15
S3	70	30
S4	50	50

Table 5.4: *Overview of the composition of the manufactured SSPCMs*

5.4 DMA testing procedure

Before the DMA test can begin, the LVE region must be identified, as explained in Section 5.4.1. It is also essential to understand how the DMA machine computes the viscoelastic properties from the measurements, which is described in Section 5.4.2 and 5.4.3. The selection and use of the clamps are discussed in Section 5.4.4 and finally, the machine specifications are provided in Section 5.4.5.

5.4.1 Linear viscoelastic regime

For each test the machine was calibrated using the 20 mm calibration block, to ensure consistent measurements. As explained in Section 2.3.3, the interest lies in testing the material within the LVE regime. Two tests were performed, one with a static strain of 5 % and varying linear dynamic strain of 0.1 % to 4 % and a second test where the static strain was set at 10 % with a varying linear dynamic strain between 0.1 % and 9 %. The results showed a consistent modulus throughout the complete dynamic strain range. It was not recommended to test on higher static/dynamic strains therefore, it was decided to keep the static strain at 5 % and the dynamic strain at 2 %. All the other settings can be found in Appendix A.2.

5.4.2 Measurement type

After the LVE region has been defined, the setup on for the actual test can be performed. A temperature-frequency sweep has been chosen, as it can be used to construct the master curve of the material. A frequency range from 1 Hz to 81 Hz with a linear frequency increment of 5 Hz has been selected and repeated at different temperatures from -25 °C to 55 °C with a temperature increment of 5 °C. Between two different temperature measurements, after the material reached the target temperature, 300 seconds of dwell time was added to ensure thermal equilibrium.

5.4.3 Measurement definition

During the sweep measurements, the change in sample length is recorded. These length measurements are converted into the storage modulus using Equation 5.1, following the recommended method by the DMA manufacturer. The first fraction term is a correction for the static preload as this already deforms the sample. This correction method assumes that the volume before (A_0 and L_0) and after the test (A_m and L_m) remains constant. The second term (k) is the stiffness simply defined as the dynamic force over the dynamic displacement and the last term represents the measured phase lag, as explained in Section 2.4. Using similar expressions, the loss modulus and loss factor can be defined for each temperature and frequency [84].

$$E' = \frac{L_m^2}{L_0 A_0} k \, cos(\delta) \tag{5.1}$$

5.4.4 Clamp selection

A key advantage of DMA is its ability to characterize a wide range of material properties, which requires different clamp configurations. Tensile clamps enable uniaxial tension tests, three-point bending fixtures are used to determine flexural behaviour and compression clamps allow the measurement of compressive modulus. Initially, tensile clamps were considered, but the samples were too soft for reliable characterization. The DMA could not apply a stable static preload, preventing consistent measurements of the initial length. Clamping was also problematic as the torque wrench used for tightening the grips applied too much force, causing the sample to be squeezed effectively increasing the length and more importantly damaging the sample. Three-point bending clamps were tested next, but the samples sagged noticeably under their own weight before any load was applied. This made the setup impractical for accurate measurements. As a result, only the compression clamps are left for testing and will be used to examine the behaviour of SSPCM. Another check that was performed is weighing all samples before and after testing to verify that no material leakage occurred.

5.4.5 Machine specifications

The DMA used in this study is a DMA 523 Eplexor® 2000 N, shown in Figure 2.4b. The instrument operates over a temperature range of -160 °C to 500 °C, allows testing frequencies from 0.0001 to 100 Hz and accommodates static deformations up to 45 mm with a dynamic amplitude of ±6 mm [36].

5.5 Results

This section presents the results of the DMA tests. Section 5.5.1 discusses the dependence of the storage modulus on temperature and frequency, followed by the analysis of the loss factor in Section 5.5.2. Finally, the data from these measurements are combined to construct master curves for all viscoelastic properties of each sample, as shown in Section 5.5.3.

5.5.1 Storage modulus

Figure 5.2 presents the relationship between the temperature and storage modulus over a temperature range from -25 °C to 55 °C for the four different compositions. The figure also displays the storage modulus in relation with the excitation frequency indicated by the colormap, spanning from low frequencies (1 Hz, red) to high frequencies (81 Hz, blue). The same dataset can also be visualised with frequency on the x-axis and temperature as the varying parameter. This alternative representation is provided in Appendix A.1 and displays the identical data shown in Figure 5.2.

The S1 sample is investigated first. From Figure 5.2a it becomes evident that the storage modulus increases with frequency, but only with a small amount of ≈17 % or 0.4 MPa. This behaviour is also observed in other research from Ouis and Lei [68, 87] and corresponds with the explanation in Section 2.3.2. It is also observed that most isotherms do not intersect, implying that the material behaves consistent and no external effects such as phase change are present, which is in line with expectations, because S1 does not contain any wax. The most interesting result is that as the temperature increases the modulus increases as well, on average ≈11 % or 0.26 MPa, this is unexpected and was only seen for the S1 sample. It also conflicts with the theory presented in Section 2.3.1, which states that the storage modulus should decease with increasing temperature. Based on the above-mentioned results, it can be concluded that the increase in frequency had a greater influence on the storage modulus than increasing the temperature.

The S2 sample in Figure 5.2b demonstrates a different effect than sample S1. Rather than increasing, the storage modulus decreases with increasing temperature, showing a decrease of about 43 % or 1.7 MPa across the full temperature range. Increasing the frequency has the opposite effect and increases the storage modulus by 40 % or 1 MPa, similar to the behaviour in S1. Another interesting observation is that the slope of Figure 5.2b becomes noticeably steeper beyond 35 °C, before returning to its original slope once the temperature exceeds 45 °C. This intermediate region likely corresponds to the melting area of the wax, as discussed in Section 5.3. In this sample, the wax content is too low to increase the storage modulus by thermal expansion. Instead, the wax starts to act as a plasticizer reducing the slope of the storage modulus, as explained in Section 2.5.1.

For the sample S3, the same general behaviour as observed for the second composition is present. The data in Figure 5.2c shows that the modulus decreases with increasing temperature. The relative change is comparable to sample S2, with a reduction of approximately 46 %, corresponding to about 2.6 MPa. Increasing the frequency again leads to a higher storage modulus, showing an increase of roughly 48 %, or 1.6 MPa, which is slightly higher than the effect measured for sample S2. As shown in Figure 5.2c, the curve begins to flatten at approximately 35 °C, suggesting that the high thermal expansion of the wax starts to influence the storage modulus. In the second composition, the plasticizer effect dominated over the thermal expansion effect, whereas in sample S3 the thermal expansion of the wax becomes strong enough to locally increase the modulus. Because the great increase in thermal expansion is limited to the melting range, the slope decreases once this interval is passed and the plasticizer effect becomes the dominant con-

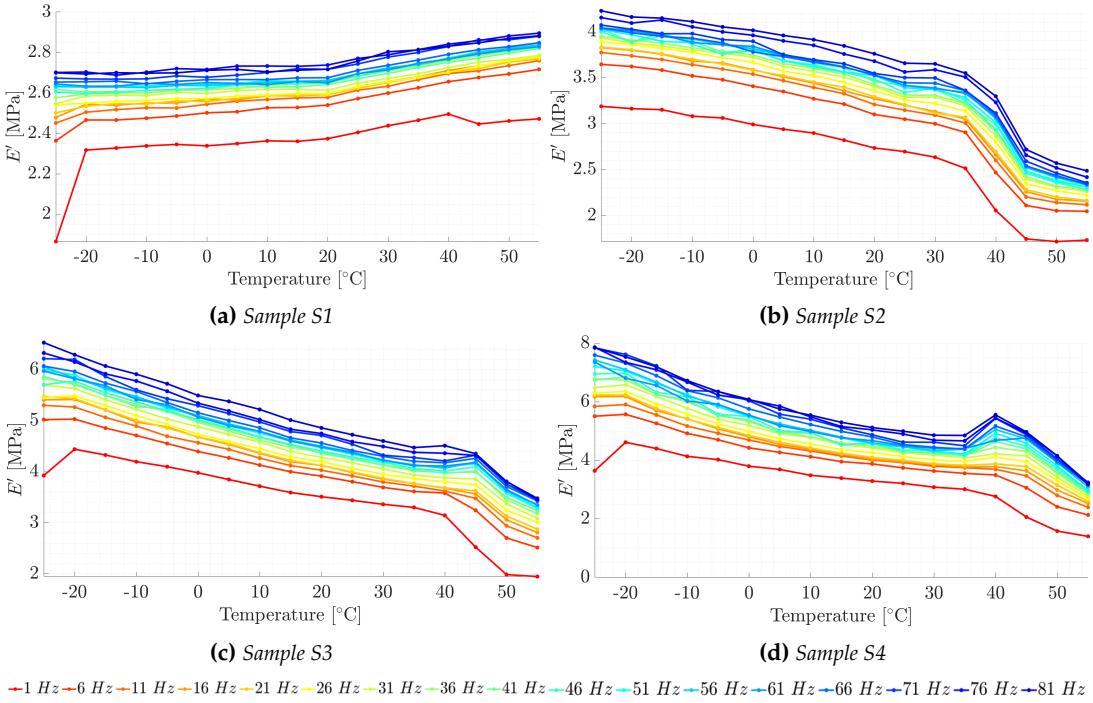

(a) *Sample S1* **(b)** *Sample S2*

(c) *Sample S3* **(d)** *Sample S4*

Figure 5.2: *Storage modulus as a function of temperature for different frequencies for the four SSPCM compositions*

tribution again. When the was content increases, the stiffness reduction caused by the plasticizer effect is compensated more strongly. This will be showcased in the last sample with the highest wax content.

The last sample S4 with the highest wax content is depicted in Figure 5.2d. The initial part of the curve matches that of sample S3. Once the melting area is reached, the higher wax content amplifies the thermal expansion. While this effect was limited in sample S3, it clearly outweighs the plasticizer effect in sample S4, leading to a local increase in storage modulus of about 23 % or 1.5 MPa at 40 °C for the high frequencies only. After this local peak the storage modulus decreases again, but with a steeper slope as in sample S3, the decrease of the complete range is on average around 58 % or 3.9 MPa, which is the highest drop of all samples. This is likely due to increased plasticizer effect of the added wax. The trend with increase frequency and increasing modulus was again consistent resulting in a 80 % or 2.4 MPa increase in modulus.

A general trend observed with increasing wax content is the linear rise in the initial storage modulus measured at -25 °C. The data suggests that each additional 10 % of wax, increases the initial storage modulus by approximately 0.85 MPa. When this is linearly extrapolated, it would result in a storage modulus of around 11 MPa for a 100 % wax content, which is in the same order of magnitude of other paraffin waxes [80].

5.5.2 Loss factor

Figure 5.3 presents the dependence of the loss factor on the temperature for the four different compositions. The figure shows the same temperature x-axis as for the storage modulus and also colormap for the frequency is the same. The only difference is that the y-axis now displays the loss factor instead of the storage modulus. The plots where the frequency is on the x-axis and the temperature is in the colormap are included in Appendix A.1.

The S1 sample is evaluated first. Inspection of Figure 5.3a shows that the loss factor decreases with increasing temperature, the average decrease is around 33 % or 0.028. This is because the storage modulus increases more than the loss modulus decreases, resulting in a decrease in the loss factor, as defined according to Equation 2.2. An increase in frequency however, results in a decrease in the loss factor by 59 % or 0.032. All the isofrequency lines are all monotonically de-

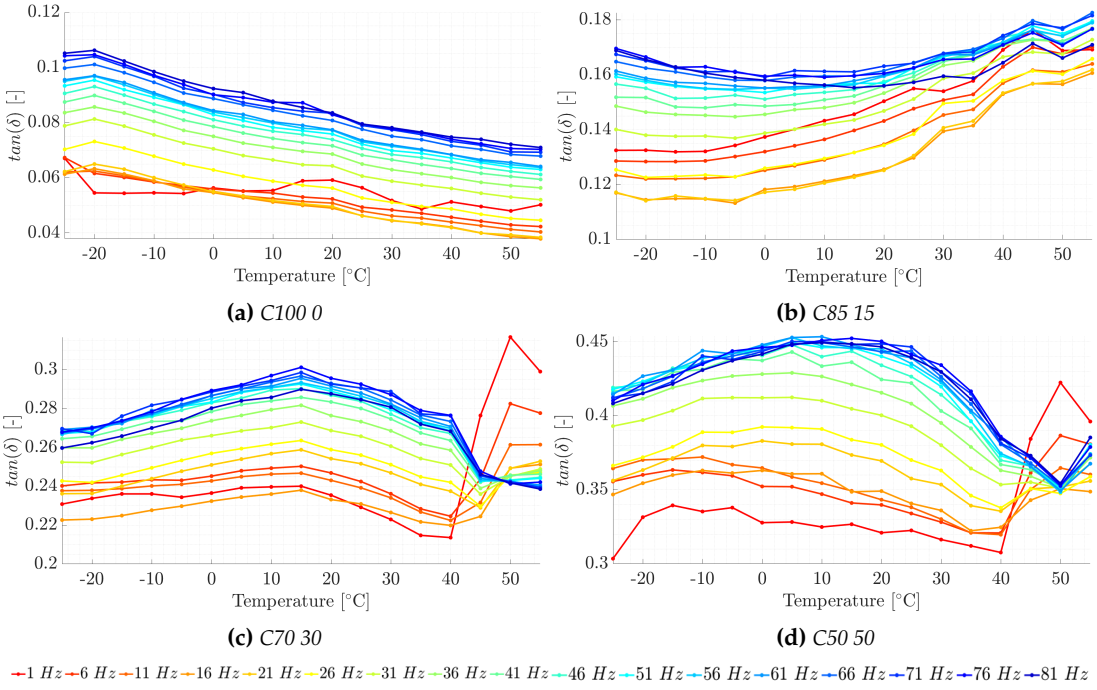

(a) *C100 0* **(b)** *C85 15*

(c) *C70 30* **(d)** *C50 50*

Figure 5.3: *Loss factor as a function of temperature for the four SSPCM compositions*

creasing with temperature except the frequency at 1 Hz, which shows different behaviour than the other lines. This phenomenon was also observed in Figure 5.2a, where the 1 Hz isofrequency line showed significantly lower storage modulus values. It was also observed that most isofrequencies do not cross each other which implies that the material behaves consistent and no external effects such as phase change are present. Lastly, Figure 5.3a shows no distinct peak in the storage modulus, which is as expected, because the peak of the loss factor occurs at way higher frequencies, as explained in Section 2.3.2.

The data in Figure 5.3b for sample S2 shows that the loss factor increases slightly with temperature, by approximately 9.5 % or 0.0128. This trend is in contrast with sample S1, where the loss factor decreased with temperature. The storage modulus increased by roughly 20 % or 0.027 when the frequency was increased. However, this increase is not monotonic. Initially, the loss factor decreases from 1 Hz up to 21 Hz before rising again above the initial value. No clear explanation for this non-monotonic trend could be identified. Finally, a small peak appears at around 45 °C for all frequencies, suggesting that the thermal expansion of the wax starts to play a role.

The behaviour of sample S3 differs noticeably from that of samples S1 and S2. The loss factor, shown in Figure 5.3c, initially rises up to approximately 15 °C, after which it gradually decreases back towards the starting value around 40 °C. Beyond this temperature several of the lower-frequency curves show a pronounced increase in loss factor. This rise can be attributed to wax expansion within the melting interval, which generates additional free volume and enhances the materials damping capacity. The maximum increase in loss factor is observed at low frequency and high temperature. In particular, 1 Hz and 50 °C, where the loss factor grows by roughly 50 % or 0.10. In contrast, the higher frequencies do not exhibit this increase. Instead, their curves converge to a lower value and cluster at around 55 °C.

Inspection of Figure 5.3d for sample S4 reveals behaviour that is largely comparable to the sample S3. The main difference is that the additional wax increases the overall loss factor. As in sample S3, only the lower frequencies show a pronounced peak in the loss factor at elevated temperatures. This peak results in an increase of about 37 %, or 0.12. Although the absolute increase is larger than in sample S3, the relative increase is smaller. Nevertheless, this local peak remains lower than the maximum loss factor observed around 15 °C for all high-frequencies.

A consistent trend across all samples is that the four lowest frequencies (1, 6, 11, and 16 Hz) show behaviour that differs from the higher frequencies. No definitive explanation was identified,

although it is may be possible that the DMA did not fully capture the loss factor at these low frequencies.

Another general observation is that the loss factor increases linearly with wax content when evaluated at -25 °C. The data indicates that each additional 10 % of wax raises the initial loss factor by approximately 0.062. A linear extrapolation to 100 % wax yields a value of about 0.69, which is high damping for a material. Finally, the measured loss factors align with the values reported in the literature.

5.5.3 Master curves

The shift factors used to construct the master curves were determined with both the RMSE and CFS methods, as described in Section 2.4.3. Each method provides a set of temperature-dependent shift factors, which can subsequently be fitted using either the WLF or Arrhenius model, introduced in Sections 2.4.3 and 2.4.3. For each sample, the results of both models are examined, and the master curve obtained from the RMSE method is presented. The master curves derived from the RMSE and CFS methods are than compared, followed by an evaluation of the validity of the WLF and Arrhenius fits.

To construct the master curve, first the unshifted isotherms for a fixed frequency range are considered on the left side of Figure 5.4. This plot presents the storage modulus as a function of the logarithmic frequency, with high temperatures indicated in red and low temperatures in blue. After selecting a reference temperature, the isotherms are shifted horizontally according to Equation 2.4, yielding the master curve shown on the right side of Figure 5.4. Curves are shifted to the left by subtracting the corresponding logarithmic shift factor and to the right by adding it, while the shift factor at the reference temperature is zero. The same procedure is used to generate the remaining master curves. Therefore, to avoid redundancy, only the final shifted plots are presented in the subsequent figures. It is worth noting that each sample uses the same shift factors to construct the master curves of the storage modulus, loss modulus and loss factor. Because the loss modulus can be derived directly from the storage modulus and the loss factor, it is not discussed in detail in the results. It is included only for completeness in the corresponding figures.

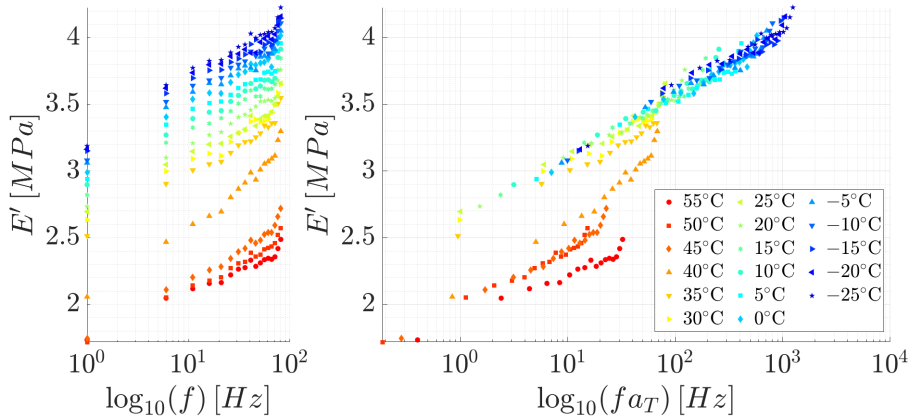

Figure 5.4: *Isotherms of the storage modulus of sample S2 at various temperatures (left) and the corresponding master curve (right) for the RMSE method*

Sample S1

The shift factors obtained from the RMSE method for sample S1 are shown in Figure 5.5a. It presents the shift factors obtained from the RMSE and CFS method in separate plots, along with their corresponding WLF and Arrhenius model fits. The WLF model is shown as a solid blue curve, representing the best fit for the free volume parameters (C_1 and C_2). The Arrhenius model is shown as a dashed red curve, characterised by the activation energy (E_a). The temperature is

plotted on the x-axis and the logarithmic shift factor on the y-axis. The reference temperature is indicated by a green marker.

The behaviour of the shift curves immediately stands out from the other samples. Unlike the silicone rubber–wax compositions, where the shift factors decrease with temperature, sample S1 shows an increase. This aligns with the observations in Section 5.5.1, where the storage modulus was found to increase with temperature. However, the assumptions of the TTSP breaks down when the storage modulus increases with temperature. As a result, the shift factors become invalid for both the WLF and Arrhenius models, which return negative invariants for the fits. This behaviour is reflected in the low R^2 value. Although a mathematical fit can still be obtained, since the invariants are not constrained, the results lack physical meaning and the corresponding R^2 values do not provide any meaningful insight.

The shift factors obtained using the CFS method, shown in Figure 5.5b, show similar behaviour to the RMSE method. Both the WLF and Arrhenius models again yield negative invariants and although the R^2 values are high, these results are not physically meaningful and should be interpreted with caution.

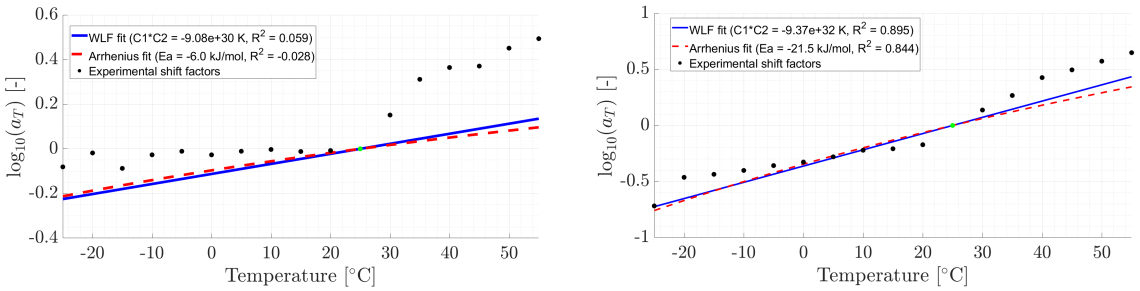

(a) *RMSE method* **(b)** *CFS method*

Figure 5.5: *Determination of the shift factors using the RMSE and CFS method, fitted by the WLF and Arrhenius model. Shown is the S1 sample with a reference temperature of 25 °C*

Because the shift factors are not physically plausible, poor master curves were expected. This was confirmed by the three master curves in Figure 5.12. The storage modulus showed some correlation, but the master curves for the loss modulus and factor show very poor correlation. The data does not collapse onto a single curve, indicating that the frequency cannot be related reliably to the viscoelastic behaviour.

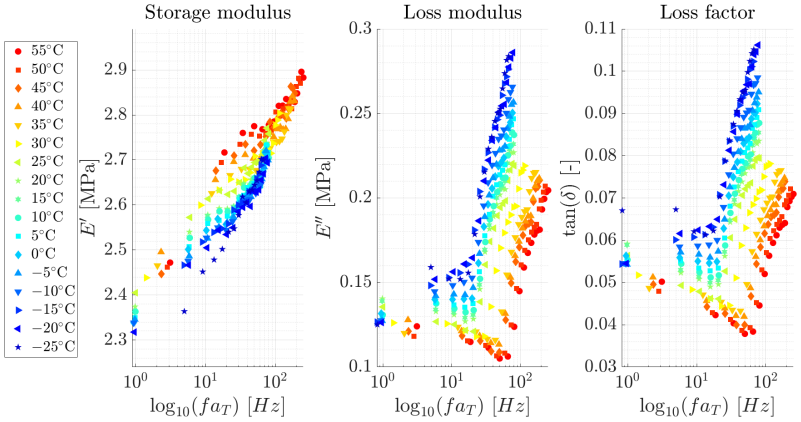

Figure 5.6: *The master curves of the viscoelastic properties of sample S1 using the RMSE method*

Sample S2

The shift factors for the RMSE method are shown in Figure 5.7a. The WLF and Arrhenius model turned out to be a good predictor for the shift factors, each achieving a R^2 of 0.93. The two curves are almost identical in shape and quality, indicating that both models can be used to represent the RMSE produced shift factors. In contrast, the WLF fit obtained with the CFS method is worse, as shown in Figure 5.7b. It shows that free volume coefficients become unrealistically large, implying that the WLF model is unable to follow the shift factor trend obtained from the CFS method. This is reflected in a lower R^2 value compared to WLF model of the RMSE method. When the Arrhenius model is applied to the shift factors from the CFS method, it shows the same overall trend as with the RMSE method, although the resulting R^2 value is lower than that obtained using the RMSE-based shift factors. Despite the lower fit quality, it still results in a physically relevant activation energy. The main reason for the poor fit is the change in shift factor trend above approximately 35 °C. This change directly corresponds to the reduction in slope observed in Figure 5.2b. Once the wax begins to play a role, the assumptions of TTSP are violated. The material changes morphology and undergoes a phase change, preventing the CFS method from capturing the behaviour correctly.

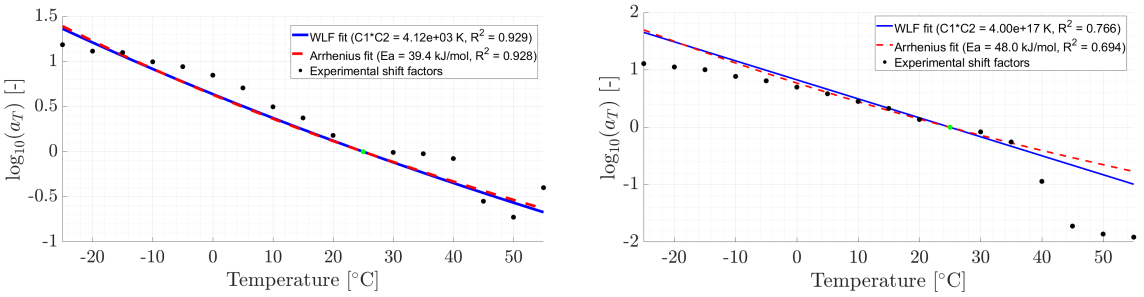

(a) *RMSE method* **(b)** *CFS method*

Figure 5.7: *Determination of the shift factors using the RMSE and CFS method, fitted by the WLF and Arrhenius model. Shown is the S2 sample with a reference temperature of 25 °C*

Figure 5.8 shows that the low-temperature isotherms for the storage modulus collapse into a single consistent master curve, while the four highest-temperature curves do not. These curves, all above 35 °C, deviate because the phase change begins in this range, violating the TTSP assumptions and preventing them from collapsing onto the same line.

The master curve for the loss factor shows very poor correlation, with the data points widely scattered, and therefore no reliable conclusions can be drawn. This behaviour is expected, as the loss factor trends in Figure 5.3 are non-monotonic and exhibit temperature-dependent changes in slope, violating the assumptions required for TTSP to be valid.

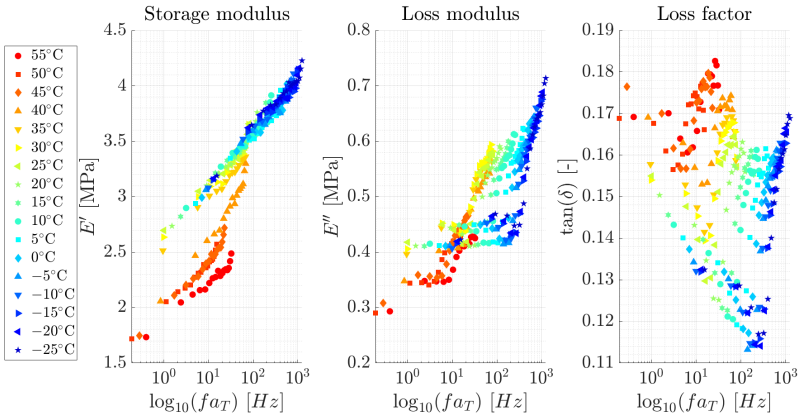

Figure 5.8: *The master curves of the viscoelastic properties of sample S2 using the RMSE method*

Sample S3

The next sample evaluated is S3, with the RMSE-based shift factors shown in Figure 5.9a. The shapes of model fits look similar to sample S2. Both the WLF and Arrhenius models yield comparable R^2 values of approximately 0.80. What is different however, is that the shift factors of the four highest temperatures (40 to 55 °C) are now above the trend instead of below. This is directly linked the to the phase change and increase of wax content, as was seen in the slight increase in storage modulus between 35 °C and 45 °C in Figure 5.2c.

The shift factors obtained using the CFS method are shown in Figure 5.9b. The data points lie nearly on a straight line, which makes it difficult to fit either the WLF or Arrhenius model, as these show hyperbolic and exponential behaviour. Consequently, the WLF fit yields unrealistically large coefficients that are not physically meaningful. In contrast, the Arrhenius model produces a reasonable value for the activation energy.

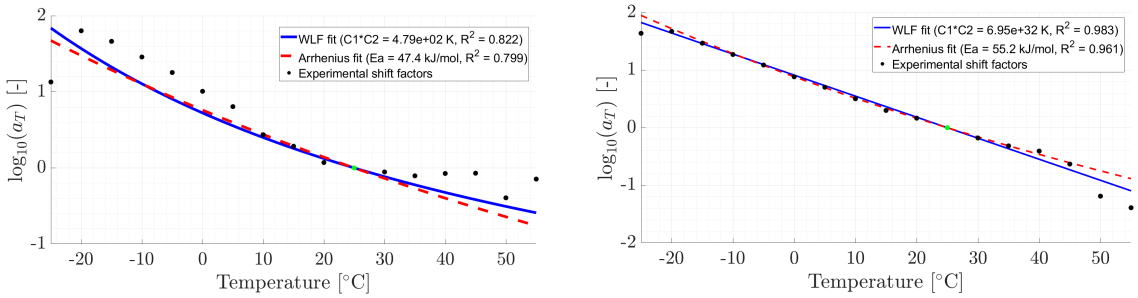

(a) *RMSE method* **(b)** *CFS method*

Figure 5.9: *Determination of the shift factors using the RMSE and CFS method, fitted by the WLF and Arrhenius model. Shown is the S3 sample with a reference temperature of 25 °C*

The master curves for the viscoelastic properties of sample S3 were obtained in a similar fashion as before and are shown in Figure 5.10. The master curve for the storage modulus is more dispersed compared with that of sample S2. Similar to sample S2 the highest temperatures deviate from the main trend for the same underlying reasons. The master curve of the loss factor shows strong temperature dependence, as reflected by the large dispersion of data points. This behaviour is directly linked to the sudden increase in loss factor at 35 °C shown in Figure 5.3c. Introducing wax alters the morphology at elevated temperatures, which ultimately causes the assumptions underlying TTSP to break down. This behaviour is inherent to the addition of wax and is, in fact, a central focus of this study.

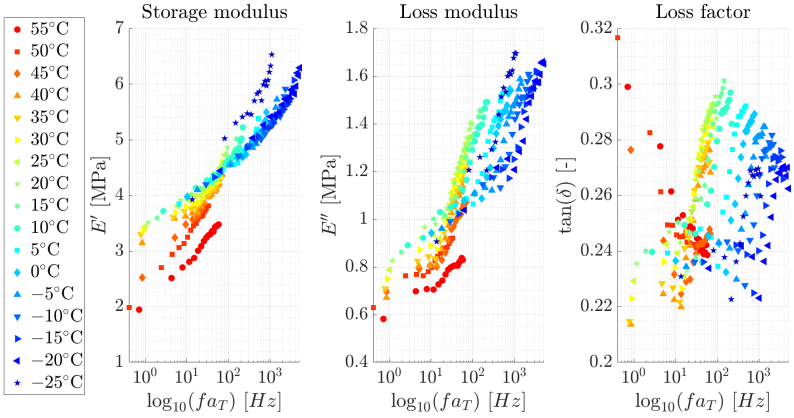

Figure 5.10: *The master curves of the viscoelastic properties of sample S3 using the RMSE method*

Sample S4

The shift factors and corresponding fits for sample S4 are presented in Figure 5.11b. For the RMSE method, the WLF and Arrhenius models have a comparable goodness of the fit, but the quality is lower than for the samples with less wax. The fit quality worsens as the wax content increases. Moreover, the shift factors of the four highest temperatures are larger than those of sample S3, indicating that a higher wax content has a bigger influence on the shift factors than the low wax contents.

The CFS method results in a similar curve, for the first time the free volume coefficients produced realistic values at a reference temperature of 25 °C. The Arrhenius model had a similar R^2 value as the WLF model, as was also the case in the other compositions.

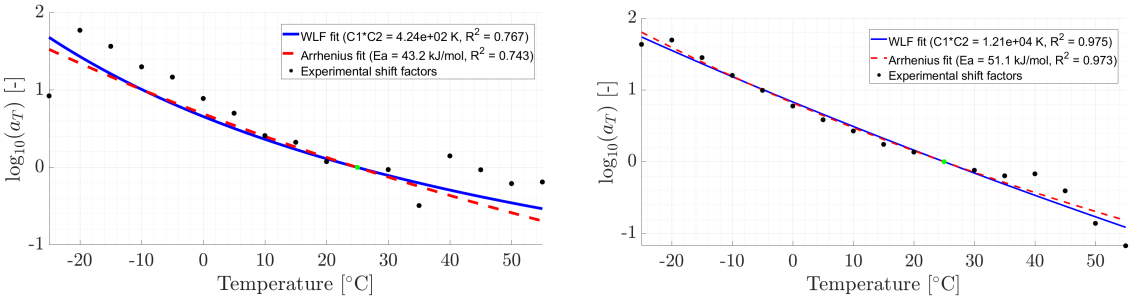

(a) *RMSE method* **(b)** *CFS method*

Figure 5.11: *Determination of the shift factors using the RMSE and CFS method, fitted by the WLF and Arrhenius model. Shown is the S4 sample with a reference temperature of 25 °C*

The master curves of sample S4, shown in Figure 5.12, display behaviour that is nearly identical to that of sample S3. The storage and loss modulus collapse reasonably well into one curve, while the loss factor shows extremely poor correlation. This can be attributed to the strongly non-monotonic behaviour, which is visible implicitly in Figure 5.3d and explicitly in Figure A.7b in appendix A.1.

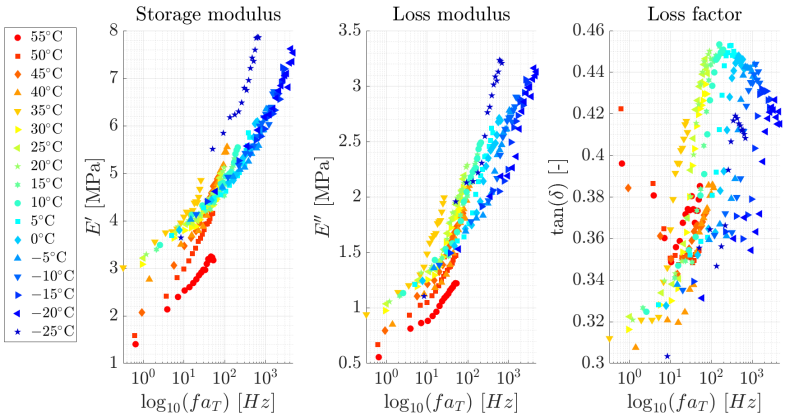

Figure 5.12: *The master curves of the viscoelastic properties of sample S4 using the RMSE method*

Comparison of the RMSE and CFS method

For each sample, both the RMSE and CFS method were applied to determine the shift factors used to construct the master curve. This section compares the results of the two approaches. Since the master curves of the different samples show similar trends, a direct comparison is presented only for sample S2 and the same observations apply to the other samples.

The results of the master curve for sample S2 for the CFS method is shown in Figure 5.8. The storage modulus plot produced by the CFS method collapses into an almost perfect straight line. At first glance this seems as a significant improvement compared with the RMSE model, even the four high temperature isotherms collapsed into a single curve. However, this outcome should be interpreted with caution. Mathematically, any set of isotherms can be shifted to appear perfectly in one line however, the underlying shift factors may be all over the place and do not follow a physical trend. In such cases, fitting a model like WLF or Arrhenius becomes impossible, because the shift factors do not show actual material behaviour. The result is a master curve with shift factors that do not reflect any material properties. This is precisely what occurs with the CFS method. The opposite situation is also possible: ensuring that the shift factors follow a smooth, model-consistent trend may lead to master curves that fit less accurately into one line. This behaviour is characterised by the RMSE method, which yields shift factors that can be reasonably fitted by a model, but produces a less coherent master curve. In summary, the CFS method enforces a well-collapsed master curve at the expense of physically meaningful shift factors, whereas the RMSE method delivers shift factors that can be fit with a model but results in a less ideal master curve.

The master curves of the loss factor in Figure 5.13 shows behaviour similar to the results obtained with the RMSE method. Comparing the RMSE and CFS master curves across all samples lead to the same conclusion: the CFS method does not perform better than the RMSE method. This is emphasized by the loss factor data in particular, because of the poor correlation when the CFS method is applied. In addition, the CFS method is significantly more computationally intensive than the RMSE method and may become unstable for larger datasets. For those reasons, the RMSE method was selected for further use.

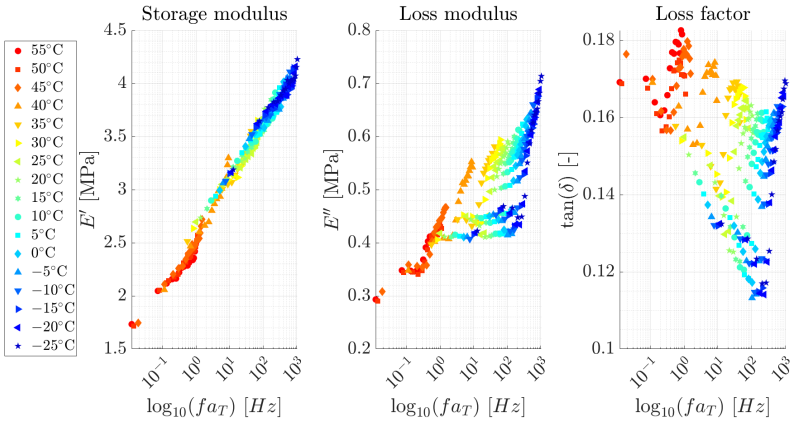

Figure 5.13: *The master curves of the viscoelastic properties of sample S2 using the CFS method*

Verification of the WLF and Arrhenius models

The shift factors and master curves already suggested that the TTSP may not hold. To examine this in more detail, the invariants of each model were evaluated at several reference temperatures. If these invariants remain constant, the TTSP is satisfied or if they vary too much, the principle fails. The results for the RMSE method of Sample S2 are shown in Table 5.5 and presents the results for different reference temperatures. The first columns shows the different reference temperatures. The second column lists the invariants for the WLF model, together with the R^2 value and standard deviation of the fit in the third and fourth column. The invariant for the Arrhenius model, the activation energy, is shown in the fifth column also followed by the R^2 value and standard deviation. The table showed that the WLF invariants are not constant, even for the few cases where the model produced physically reasonable values. These invariants range from 160 K to 4100 K, while typical WLF constants generally lie between 900 and 1100 K [68]. Such results were excluded from further consideration. The Arrhenius invariants exhibit more mathematically stable results across the complete temperature range, but the fitted activation energies reduce with varying reference temperature, varying from 11 to 72 kJ/mol. Moreover, the corresponding fits are poor, with correlation coefficients below 0.20. Because both sets of invariants depend strongly on the chosen reference temperature, it can be concluded that sample S2 violates the assumptions of TTSP. As a result, any master curve constructed for this sample must be interpreted with caution.

To verify the TTSP for the remaining samples, the same procedure was applied. The invariants, together with the corresponding R^2 values and standard deviations for the WLF and Arrhenius models, are provided in Appendix A.1. The results show that none of the other samples exhibit constant invariants, meaning their master curves must be interpreted with caution.

Table 5.5: *Overview of WLF and Arrhenius invariants and fit parameters as a function of reference temperature for sample S2 for the RMSE method*

$T_{\mathbf{ref}}$ [°C]	C_1C_2 [K]	$R^2_{\mathbf{WLF}}$ [-]	$\mathbf{STD_{WLF}}$ [-]	E_a [kJ/mol]	$R^2_{\mathbf{Arr}}$ [-]	$\mathbf{STD_{Arr}}$ [-]
55	1.29×10^{33}	0.53444	0.63450	68.388	0.35605	0.67361
50	2.68×10^{33}	0.48594	0.67789	70.742	0.32182	0.68820
45	5.45×10^{33}	0.44539	0.70377	71.570	0.30635	0.67605
40	2.74×10^{32}	0.80380	0.38194	55.184	0.73978	0.40091
35	3.14×10^{33}	0.95276	0.15377	40.825	0.92580	0.18659
30	5.43×10^{31}	0.95410	0.14196	38.566	0.93946	0.15784
25	4124.1	0.92907	0.17029	39.371	0.92807	0.14936
20	721.79	0.90991	0.17357	35.483	0.90540	0.13683
15	311.05	0.89995	0.15970	29.639	0.88149	0.13402
10	160.51	0.85490	0.17560	25.223	0.81328	0.14358
5	3835.9	0.47192	0.52504	28.853	0.47130	0.50602
0	1.51×10^{29}	0.39248	0.52074	23.858	0.38698	0.50532
-5	7.24×10^{29}	0.34883	0.52432	20.581	0.34157	0.50774
-10	1.95×10^{30}	0.30868	0.52519	17.644	0.29792	0.50917
-15	3.33×10^{29}	0.25602	0.52322	15.169	0.24067	0.51026
-20	1.30×10^{30}	0.23509	0.52535	13.282	0.21760	0.51244
-25	1.86×10^{30}	0.20530	0.52499	11.744	0.18615	0.51297

When fitting the WLF and Arrhenius model to the shift factors, it is essential to consider not only the invariants but also the underlying assumptions. The WLF model is applicable from T_g to approximately T_g+100 °C, where free volume effects dominate. Since silicone rubber has a T_g of about -125 °C, the lowest temperatures in the dataset already fall outside this valid range. Moreover, the WLF formulation assumes a linear relationship with free volume and temperature, an assumption that no longer holds once wax is introduced and a phase change occurs. These factors limit the applicability of the WLF model. In contrast, the Arrhenius model is generally applicable only below T_g, where the free volume is effectively frozen and relaxation is controlled by activation energy. Because the measurements span -25 to 55 °C, well above the T_g of silicone rubber, the model does not strictly apply. Consequently, both models must be interpreted with

caution when used for SSPCMs.

A potential way to address the violation of the TTSP is to divide the data into two segments. The first segment includes the temperatures up to onset of the phase change and the second segment covers the area in which the phase change occurs. The shift factors produced by the RMSE and CFS method will remain constant for both segments, only the reference temperature will change. Therefore, this will only result in an improvement for the fits of the WLF and Arrhenius model. When the temperature range is extended also a third segment could be introduced and fitted using either model.

5.6 Conclusion & Discussion

The design, development and characterisation of in-house manufactured SSPCMs were evaluated. Suitable matrix and filler materials were identified using SMART-based requirements, leading to the selection of Dragon Skin^{TM} 30 and hard paraffin wax. Four SSPCMs were manufactured using a controlled casting process, after which the viscoelastic properties of these materials were characterised within the LVE region using the DMA machine. A combined temperature–frequency sweep and compression test was performed to construct master curves and determine the temperature dependence of the viscoelastic behaviour for each sample. The results showed that the storage modulus generally decreased with increasing temperature, but this reduction could be compensated by adding more wax. Only at high wax contents, around 50 %, the storage modulus actually increased, reaching a maximum increase of 23 % in the wax melting area. The loss factor was also strongly affected by wax content: higher wax content produced an overall increase in damping for all samples, as well as a local rise of around 37 % near the melting area, particularly at low frequencies for s 50 % wax content. These findings demonstrate that wax expansion around the phase transition can partially compensate for the reduction in damping with temperature.

The shift factors required to construct the master curves were determined using either the RMSE or CFS method and subsequently fitted with the WLF or Arrhenius model. The results indicated that the RMSE method yielded more physic-based results, while the CFS method is more mathematical oriented. A comparison of the WLF and Arrhenius models further demonstrated that neither model adequately describes the shift factor behaviour, because the experimental temperature range lies outside the validity domain of both formulations.

Lastly, the master curves were evaluated. While the master curves for samples for the storage modulus showed reasonable correlation, the loss modulus and loss factor displayed very poor correlation. This outcome is expected, as the TTS assumptions are violated: the data is non-monotonic, strongly temperature dependent, thermorheologically complex and influenced by morphological changes such as the wax phase transition. A potential improvement could be to split the temperature data in a part before and after the phase transition or fit the data with different models.

For the DMA tests, several improvements are possible. The DMA manual recommends a logarithmic sweep rate with at least 11 points per decade over two decades, while this study used a linear sweep rate from 1 to 81 Hz with 5 Hz spacing. Using a logarithmic frequency distribution would provide more evenly spaced data on the log scale and may improve the quality of the constructed master curves.

Most figures showed unexplained behaviour in the measurements at 1 Hz. To determine whether this behaviour reflects the true material response or is the result of an artefact, three approaches can be considered. The first is to perform a temperature sweep from -25 ° to 55 °C at a fixed frequency of 1 Hz. The second is to run a frequency sweep from 1 to 81 Hz at a constant temperature of 25 °C, the third is to reverse the frequency sweep direction, measuring from 81 Hz down to 1 Hz.

Lastly, the assessment of how well the master curve collapses remains subjective. In this work, the quality was judged visually by evaluating whether the data points aligned along a smooth, continuous curve. A more objective way to evaluate the validity of a master curve is to use a Van Gurp-Palmen (vGP) plot, which shows the complex modulus as a function of the phase angle. When the data points form a smooth line, the master curve can be considered reliable [68].

6 | Conclusion & Recommendations

The goal of this work was to characterize, design and develop state-of-the-art SSPCMs capable of adjusting stiffness and damping through controlled temperature changes. The literature study showed that behaviour of SSPCMs is governed by two opposing mechanisms: silicone rubber softens with temperature due to increased molecular mobility, while paraffin wax expands strongly near its melting area, generating internal pressure that can counteract stiffness loss.

The theoretical reassessment of Flints work confirmed this conceptual mechanism but also revealed substantial experimental limitations. It was found that, compared with the beam containing the 100/0 % composition, the 85/15 % composition compensated the 10 % drop in stiffness due to this mechanism. Next, the damping for 100/0 % composition, without wax, showed 15 % higher damping than the 85/15 % composition, indicating that adding wax reduces the total damping. However, non-uniform heating, limited sensor usage, inconsistent boundary conditions, small datasets and deviations in composition introduced significant uncertainty. Therefore, the results prevented drawing definite conclusions about the damping across compositions.

The next part focused on experimentally validating Flints beams under improved testing conditions. The normalized eigenfrequency of the 100/0 % composition unexpectedly increased by 8 % with temperature, which was the highest across all temperatures. Since no wax was present that could thermally expand, it suggests that silicone rubber alone already introduces eigenfrequency tunability. The 85/15 % composition, although containing wax, showed a smaller increase of about 5 %, while beam 3 exhibited no tuning capability, with its eigenfrequency decreasing monotonically over the full temperature range.

The analysis was shifted from dynamic to material-level characterization. Using the DMA machine allowed precise control of temperature, standardized sample geometry and direct extraction of viscoelastic properties without modal parameter estimation. The newly in-house manufactured SSPCMs samples, with a wax content ranging from 0 % to 50 %, showed clear trends. The storage modulus generally decreased with temperature but this reduction could be counteracted by adding more wax. Only at the high wax content of 50 %, the storage modulus in the melting area increased by 23 %. The loss factor followed a similar trend: higher wax contents increased overall damping and produced a local increase of about 37 % near the phase transition, particularly at low frequencies. These results confirm that wax expansion during melting can tune the stiffness and damping.

In conclusion, this work demonstrated that silicone rubber-wax compositions can adopt their properties based on different composition by changing the temperature. The work established a validated methodology for the testing and development of SSPCM.

Future research should focus more on the material science aspect of SSPCMs, ensuring that the fundamental properties of the individual constituents are well understood before they are combined into SSPCMs. The composition of silicone rubber and paraffin wax can be determined using a spectrometry, while the T_g and T_m of both materials can be determined through Differential Scanning Calorimetry (DSC). Since thermal expansion plays a key role in the behaviour of SSPCMs, it should be characterised using a TMA. Once these properties are known, the location and extent of the wax phase transition can be assessed more accurately, allowing a clearer understanding of how the eigenfrequency and damping can be tuned. With this foundation established, future work should focus more closely on the behaviour within the melting area.

Other classes of materials that can modify their properties in response to an external stimulus include non-Newtonian fluids such as shear-thickening fluids (STFs), electrorheological (ER) materials, magnetorheological (MR) materials and shape memory alloys (SMAs). Those types of materials can be explored in the future as SSPCMs.

Acknowledgement

I would like to express my thank to Dr. D. Di Maio for his guidance and supervision during my Master Thesis. Also, I would like to thank Ed Habtour for his valuable input to my research. Additionally, I would like to express my sincere gratitude to the ETE group for allowing me to use their DMA machine. In particular, I want to thank E. Uzun and A. Tskhay for their support and guidance during the measurements. Lastly, I would like to thank A. Lok from the DBM department for his support with helping me to set up the experimental modal testing.

During the writing process, the author declares to have used Google Gemini and OpenAI's ChatGPT to refine, rewrite and enhance the clarity and coherence of this work. All generated content was carefully reviewed and edited as necessary and the author assumes full responsibility for this work.

References

[1] R. G. K. M. Aarts, G. R. B. E. Römer, and C. van Keulen. Modeling & analysis of dynamic systems: Exercises 2020–2021, with answers. Technical report, University of Twente, Faculty of Engineering Technology, Enschede, The Netherlands, 2020.

[2] A Abhat. Low temperature latent heat thermal energy storage: heat storage materials. *Solar energy*, 30:313–332, 1983. URL https://doi.org/10.1016/0038-092X(83)90186-X.

[3] Jillian Cathleen Adams, Joseph Angelo Torres, Heather Michelle Volz, Jennifer Marie Gallegos, and Dali Yang. Anisotropic thermal behavior of silicone polymer, dc 745. Technical report, Los Alamos National Laboratory, 2016. URL https://doi.org/10.2172/1312621.

[4] *Flex-Tec HV Technical Data Sheet*. Advanced Repair Technology Inc, USA, Cherry Valley, NY 13320, 2012. URL https://shorturl.at/eitdU. Accessed:2025-18-10.

[5] Wacker Chemie AG. Solid and liquid silicone rubber material and processing guidelines, 2011. URL https://www.wacker.com/h/medias/6709-EN.pdf. Technical Information 6709 EN.

[6] Wacker Chemie AG. Room-temperature vulcanizing (rtv) silicones: Material and processing guidelines, 2018. URL https://www.wacker.com/h/en-us/medias/7461-EN.pdf.

[7] Wacker Chemie AG. Silicone rubbers: Processing and properties guide, 2021. URL https://www.wacker.com/h/medias/6709-EN.pdf.

[8] Reema Alasfar, Said Ahzi, Nicolas Barth, Viktor Kochkodan, Marwan Khraisheh, and Muammer Koç. A review on the modeling of the elastic modulus and yield stress of polymers and polymer nanocomposites: Effect of temperature, loading rate and porosity. *Polymers*, 14(3):360, 2022. URL https://doi.org/10.3390/polym14030360.

[9] Adrián Álvarez-Vázquez, Alfonso Fernández-Canteli, Enrique Castillo Ron, Pelayo Fernandez Fernandez, Miguel Muñiz-Calvente, and Maria Jesus Lamela Rey. A novel approach to describe the time–temperature conversion among relaxation curves of viscoelastic materials. *Materials*, 13(8):1809, 2020. URL https://doi.org/10.3390/ma13081809.

[10] Angreen. Thermoplastic polyurethane (tpu) melting point and glass transition temperature, 2024. URL https://www.angreen.com/news/tpu-melting-point.html. Accessed: 2025-4-10.

[11] Natalia Babkina, Oksana Antonenko, Ludmila Kosyanchuk, Liubov Vorontsova, Oleg Babich, and Olexander Brovko. Effect of polyurethane material design on damping ability. *Polymers for Advanced Technologies*, 34:3426–3437, 07 2023. URL https://doi.org/10.1002/pat.6156.

[12] P Bharadwaj Reddy, C Gunasekar, Atul Shalikrao Mhaske, and Mr N Vijay Krishna. Enhancement of thermal conductivity of pcm using filler graphite powder materials. In *IOP Conference Series: Materials Science and Engineering*, volume 402, page 012173. IOP Publishing, aug 2018. URL https://doi.org/10.1088/1757-899X/402/1/012173.

[13] Manfred A Bohn. The connection between the parameters of wlf equation and of arrhenius equation. *Propellants, Explosives, Pyrotechnics*, 44(6):696–705, 2019. URL https://doi.org/10.1002/prep.201800329.

[14] Bol.com. Zoezo design paraffine was 1 kg korrels (laag oliegehalte), 2025. URL https://shorturl.at/owDqK. Accessed: 2025-5-6.

[15] MW Boomstra, MWJ van Asseldonk, BJ Geurts, VM Nazarychev, and AV Lyulin. Effects of branching and polydispersity on thermal conductivity of paraffin waxes. *International Journal of Heat and Mass Transfer*, 195:123192, 2022. URL https://doi.org/10.1016/j.ijheatmasstransfer.2022.123192.

[16] Alpha Wax BV. Paraffin wax structure: Molecular chains & properties. Alpha Wax blog, 3 2025. URL https://www.alphawax.com/blog/paraffin-wax-structure. Accessed on 2025-10-21.

[17] Yuyang Chai, Wei Gao, Benjamin Ankay, Fengming Li, and Chuanzeng Zhang. Aeroelastic analysis and flutter control of wings and panels: a review. *International Journal of Mechanical System Dynamics*, 1(1):5–34, 2021. URL https://doi.org/10.1002/msd2.12015.

[18] Nagase ChemteX. Comparison of silicone rubber and other materials, 2024. URL https://shorturl.at/amhtz. Accessed: 2025-10-15.

[19] Chill Epoxy. Epoxy resin temperature resistance, 2024. URL https://chillepoxy.com/epoxy-resin-temperature-resistance/. Accessed: 2025-10-15.

[20] Thomas C Clancy, SJV Frankland, JA Hinkley, and TS Gates. Molecular modeling for calculation of mechanical properties of epoxies with moisture ingress. *Polymer*, 50(12):2736–2742, 2009. URL https://doi.org/10.1016/j.polymer.2009.04.021.

[21] Ian Rex Clemitson. *Castable polyurethane elastomers*. CRC Press, 2008. URL https://doi.org/10.1201/9781420065770.

[22] Changsha Rich Nonferrous Metals Co. Ga-in-sn melting point 10 °c / 50 °f — gallium-indium-tin eutectic heat transfer liquid metal, 2025. URL https://shorturl.at/8lKin. Accessed: 2025-7-10.

[23] GBSA Rubber Company. Polyurethane rubber (au-eu), 2025. URL https://www.gbsa.com.

[24] Dow Corning Corporation. *Dow Corning 732 Multi-Purpose Sealant Technical Data Sheet*, 2015. URL https://aviooil.com/wp-content/uploads/2015/03/Dow-Corning-732-TDS.pdf. Accessed: 2025-10-15.

[25] Julen Cortazar-Noguerol, Fernando Cortés, Imanol Sarría, and María Jesús Elejabarrieta. Preload influence on the dynamic properties of a polyurethane elastomeric foam. *Polymers*, 16(13), 2024. URL https://doi.org/10.3390/polym16131844.

[26] DesignerData. Polyurethane rubber material properties, 2024. URL https://designerdata.nl/materials/plastics/rubbers/polyurethane-rubber. Accessed: 2025-10-15.

[27] *Technical Datasheet: LM138 – 138 °C Low Melt Moulding Alloy*. Easy Composites Ltd, Stoke-on-Trent, UK, version 1.0 edition, 2025. URL https://shorturl.at/CfWvq. Accessed: 2025-4-10.

[28] *Technical Datasheet: LM95 – 95 °C Low Melt Moulding Alloy*. Easy Composites Ltd, Stoke-on-Trent, UK, version 1.0 edition, 1 2025. URL https://shorturl.at/3XQTb. Accessed: 2025-4-10.

[29] Epoxy Technology. Tech tip 30: Understanding how to choose an appropriate thermally conductive epoxy, 2019. URL https://shorturl.at/UO6ps. Accessed: 2025-10-15.

[30] David J Ewins. *Modal testing: theory, practice and application*. John Wiley & Sons, 2009.

[31] Zhanpeng Fang and Ling Zheng. Topology optimization for minimizing the resonant response of plates with constrained layer damping treatment. *Shock and Vibration*, 2015(1): 376854, 2015. URL https://doi.org/10.1155/2015/376854.

[32] Linglong Feng, Shusheng Li, and Shengyu Feng. Preparation and characterization of silicone rubber with high modulus via tension spring-type crosslinking. *RSC advances*, 7(22): 13130–13137, 2017. URL https://doi.org/10.1039/C7RA00293A.

[33] Spencer Flint, Bart Boom, Thijs Masmeijer, Dario Di Maio, and Ed Habtour. Tunable aeroelasticity with self-tunable composite materials. In *AIAA SCITECH 2024 Forum*. American Institute of Aeronautics and Astronautics, 2024. URL https://doi.org/10.2514/6.2024-0026.

[34] Gallagher Corporation. Polyurethane temperature range, 2024. URL https://gallaghercorp.com/polyurethane-temperature-range/. Accessed: 2025-10-15.

[35] Nuno V Gama, Artur Ferreira, and Ana Barros-Timmons. Polyurethane foams: Past, present, and future. *Materials*, 11(10):1841, 2018. URL https://doi.org/10.3390/ma11101841.

[36] NETZSCH-Gerätebau GmbH. Dma 503 eplexor® series – high-force dynamic mechanical testing systems. Technical brochure, 2024. URL https://shorturl.at/BbmJB. accessed: 2025-11-14).

[37] Rubitherm Technologies GmbH. *Technical Data Sheet: RUBITHERM RT47 Pure Phase-Change Material*. Imhoffweg 6, D-12307 Berlin, Germany, 09 2020. URL https://www.rubitherm.eu/media/products/datasheets/Techdata_-RT47_EN_09102020.PDF. Accessed: 2025-09-15.

[38] Rubitherm Technologies GmbH. *Technical Data Sheet: RUBITHERM RT60 Pure Phase-Change Material*. Imhoffweg 6, D-12307 Berlin, Germany, 09 2020. URL https://www.rubitherm.eu/media/products/datasheets/Techdata_-RT60_EN_09102020.PDF. Accessed: 2025-09-15.

[39] Rubitherm Technologies GmbH. Pcm rt-line – versatile organic pcm for your application, 2025. URL https://www.rubitherm.eu/en/productcategory/organische-pcm-rt. Accessed: 2025-09-15.

[40] M Golzar, J Sinke, and M Abouhamzeh. Novel thermomechanical characterization for shrinkage evolution of unidirectional semi-crystalline thermoplastic prepregs (pps/cf) in melt, rubbery and glassy states. *Composites Part A: Applied Science and Manufacturing*, 156: 106879, 2022. URL https://doi.org/10.1016/j.compositesa.2022.106879.

[41] Leon E Govaert, Anne K van der Vegt, and Martin van Drongelen. *Polymers: from structure to properties*. Delft Academic Press, 2019.

[42] Tieneng Guo, Yunchao Gu, Shiming Ma, and Li Wang. Dynamic mechanical properties of zn-35 silicone rubber materials based on hn model. In *2016 4th International Conference on Machinery, Materials and Computing Technology*, pages 1073–1079. Atlantis Press, 2016. URL https://doi.org/10.2991/icmmct-16.2016.212.

[43] Jae Gyoung Gwon, Seok Kyeong Kim, and Jung Hyeun Kim. Sound absorption behavior of flexible polyurethane foams with distinct cellular structures. *Materials & Design*, 89:448–454, 2016. URL https://doi.org/10.1016/j.matdes.2015.10.017.

[44] Xiang Han, Di Wang, Xudong Chen, Shuai Nie, Chenxi Huyan, Dong Liu, and Fei Chen. High damping polyurethane elastomers with wide temperature ranges. *Polymer*, 325: 128307, 2025. URL https://doi.org/10.3390/polym15143005.

[45] Holger Hennings. Active flutter suppression: Are we reactive enough?, 2024. URL https://www.dlr.de/en/ae/latest/technical-articles/active-flutter-suppression-are-we-reactive-enough. Accesed on: 10-10-2025.

[46] Dewey H Hodges and G Alvin Pierce. *Introduction to structural dynamics and aeroelasticity*, volume 15. cambridge university press, 2011.

[47] Norman R Horn. A critical review of free volume and occupied volume calculation methods. *Journal of Membrane Science*, 518:289–294, 2016. URL https://doi.org/10.1016/j.memsci.2016.07.014.

[48] M Enamul Hossain, Chefi Ketata, and M Rafiqul Islam. Experimental study of physical and mechanical properties of natural and synthetic waxes using uniaxial compressive strength test. In *Third International Conference on Modeling, Simulations and Applied Optimization, Sharjah, United Arab Emirates*, pages 1–5, 2009. URL https://shorturl.at/57md8.

[49] Belmont Metals Inc. Field's metal, 144 °f / 62 °c low melting alloy. Online product page, 12 2018. URL https://www.belmontmetals.com/product/fields-metal/. Accessed: 2025-1-10.

[50] Incurelab. The heat resistance of epoxy: A key consideration for professionals, 2025. URL https://shorturl.at/9Czwt. Accessed: 2025-10-16.

[51] TA Instruments. Determining the linear viscoelastic region in oscillatory measurements. Technical report, TA Instruments, 2019. URL https://www.tainstruments.com/pdf/literature/RH107.pdf. Accessed: 2025-11-13.

[52] TA Instruments. Dynamic mechanical analysis: Basic theory & applications — online training part 1. Online training document, 2020. URL https://shorturl.at/xkLXA. accessed: 2025-11-14.

[53] *Plastics – Thermomechanical analysis (TMA) – Part 2: Determination of coefficient of linear thermal expansion and glass transition temperature*. International Organization for Standardization, Geneva, Switzerland, 2nd edition, 11 2021.

[54] Intertronics. Tb2007-12 thermally conductive silicones, 2007. URL https://shorturl.at/6spti. Accessed: 2025-10-15.

[55] Hanieh Kargarzadeh, Ishak Ahmad, and Ibrahim Abdullah. Mechanical properties of epoxy–rubber blends. In *Handbook of epoxy blends*, pages 1–36. Springer, 2015. URL https://doi.org/10.1007/978-3-319-40043-3_11.

[56] Sari Katz, Noa Lachman, Nir Hafif, Lilach Rosh, Alexander Pevzner, Amir Lybman, Tal Amitay-Rosen, Ido Nir, and Hadar Rotter. Studying the physical and chemical properties of polydimethylsiloxane matrix reinforced by nanostructured tio2 supported on mesoporous silica. *Polymers*, 15(1):81, 2022. URL https://doi.org/10.3390/polym15010081.

[57] SM Kong, M Mariatti, and JJC Busfield. Effects of types of fillers and filler loading on the properties of silicone rubber composites. *Journal of reinforced plastics and composites*, 30(13): 1087–1096, 2011. URL https://doi.org/10.1177/0731684411416267.

[58] Manel Kraiem, Mustapha Karkri, Magali Fois, and Patrik Sobolciak. Thermophysical characterization of paraffins versus temperature for thermal energy storage. *Buildings*, 13(4): 877, 2023. URL https://doi.org/10.3390/buildings13040877.

[59] Rheology Lab. (dma) dynamic mechanical analysis: Tension, torsion, compression, 2025. URL https://www.rheologylab.com/services/dynamic-mechanical-analysis-dma/. Accessed: 2025-11-12.

[60] Robert F Landel and Lawrence E Nielsen. *Mechanical properties of polymers and composites*. CRC press, 1993. URL https://doi.org/10.1201/b16929.

[61] Kent Larson. Low temperature characteristics of silicones. *Electronics Global Application Engineering Center, Dow Corning Corporation*, 2005. URL https://www.electronics.org/system/files/technical_resource/E14%26S05-04.pdf.

[62] Clemens J. M. Lasance. The thermal conductivity of rubbers/elastomers, 11 2001. URL https://shorturl.at/0IUQu. Accessed: 2025-10-11.

[63] Tae-Ik Lee, Min Sung Kim, and Taek-Soo Kim. Contact-free thermal expansion measurement of very soft elastomers using digital image correlation. *Polymer Testing*, 51:181–189, 2016. URL https://doi.org/10.1016/j.polymertesting.2016.03.014.

[64] Wenbo Li et al. Study on epoxy resin with high elongation-at-break using polyamide and polyether amine as a two-component curing agent, 2022. URL https://doi.org/10.1515/epoly-2017-0252.

[65] Michael Link, Marc Boeswald, Sebastien Laborde, Matthias Weiland, and Adriano Calvi. An approach to non-linear experimental modal analysis. In *Nonlinear Modeling and Applications, Volume 2: Proceedings of the 28th IMAC, A Conference on Structural Dynamics, 2010*, pages 119–128. Springer, 2011. URL https://doi.org/10.1007/978-1-4419-9719-7_11.

[66] Adam Lipchitz, Glenn Harvel, and Takeyoshi Sunagawa. Experimental investigation of the thermal conductivity and viscosity of liquid in–bi–sn eutectic alloy (field's metal) for use in a natural circulation experimental loop. In *Proceedings of the 23rd International Conference on Nuclear Engineering*, 5 2015. URL https://shorturl.at/vm4OA.

[67] Adam Lipchitz, Glenn Harvel, and Takeyoshi Sunagawa. Thermophysical characteristics of liquid metal in-bi-sn eutectic (field's metal) as a similarity coolant. *Journal of Nuclear Engineering and Radiation Science*, 8(3):031301, 2022. URL https://doi.org/10.1115/1.4053632.

[68] Xiu Liu, Dingxiang Zhu, Jianguo Lin, and Yongjun Zhang. Temperature and frequency dependence of the dynamic viscoelastic properties of silicone rubber. *Polymers*, 15(14):3005, 2023. URL https://doi.org/10.3390/polym15143005.

[69] Peter Lunkenheimer, Alois Loidl, Birte Riechers, Alessio Zaccone, and Konrad Samwer. Thermal expansion and the glass transition. *Nature Physics*, 19(5):694–699, 2023. URL https://doi.org/10.1038/s41567-022-01920-5.

[70] David W. C. MacMillan. *Fundamental Concepts of Organic Chemistry*. Wiley, Hoboken, NJ, 2011.

[71] Arne Mann, Christoph Maria Bürgel, and Peter Groche. A modeling strategy for predicting the properties of paraffin wax actuators. *Actuators*, 7(4), 2018. URL https://doi.org/10.3390/act7040081.

[72] Arne Mann, Thiemo Germann, Mats Ruiter, and Peter Groche. The challenge of upscaling paraffin wax actuators. *Materials & Design*, 190, 2020. URL https://doi.org/10.1016/j.matdes.2020.108580.

[73] Azo materials. Ep21tp-2: Thermal cycling resistant epoxy polysulfide hybrid compound offers outstanding toughness, 2024. URL https://shorturl.at/Wm0kF. Accessed: 2025-11-11.

[74] MatWeb. Overview of materials for thermoset polyurethane, elastomer, unreinforced, 2025. URL https://shorturl.at/PLzPe. Accessed: 2025-10-16.

[75] MatWeb. Overview of materials for epoxy adhesive, flexible, 2025. URL https://shorturl.at/BRNHa. Accessed: 2025-10-16.

[76] Alan D McNaught. *Compendium of chemical terminology*, volume 1669. Blackwell Science Oxford, 1997. URL https://publications.iupac.org/publications/compendium/index.html.

[77] Mearthane Products Corporation. Polyurethane temperature range, 2025. URL https://knowledgecenter.mearthane.com/polyurethanetemperaturerange. Accessed: 2025-11-23.

[78] Kevin P Menard and Noah Menard. *Dynamic mechanical analysis*. CRC press, 2020. URL https://doi.org/10.1201/9780429190308.

[79] Mokgaotsa J Mochane, Teboho C Mokhena, Tshwafo E Motaung, and Linda Z Linganiso. Shape-stabilized phase change materials of polyolefin/wax blends and their composites: A systematic review. *Journal of Thermal Analysis and Calorimetry*, 139(5):2951–2963, 2020. URL https://doi.org/10.1016/j.apenergy.2015.10.030.

[80] S. Mondal. Phase change materials for smart textiles – an overview. *Applied Thermal Engineering*, 28(11):1536–1550, 2008. URL https://doi.org/10.1016/J.APPLTHERMALENG.2007.08.009.

[81] Anna Morawska-Chochół, Magdalena Szumera, Andrzej Młyniec, and Kinga Pielichowska. The effect of aging process conditions on the thermal properties of poly (dimethylsiloxane)-based silicone rubber. *Materials*, 17(22):5608, 2024. URL https://doi.org/10.3390/ma17225608.

[82] NB Morley, J Burris, LC Cadwallader, and MD Nornberg. Ga-in-sn usage in the research laboratory. *Review of Scientific Instruments*, 79(5), 2008. URL https://doi.org/10.1063/1.2930813.

[83] Nagase ChemteX. Comparison of urethane rubber and other materials, 2024. URL https://shorturl.at/qo4z5. Accessed: 2025-10-15.

[84] *Eplexor 9 Operating Manual, Software Version 9.1600*. NETZSCH GABO Instruments GmbH, Schulstrasse 6, 29693 Ahlden, Germany, 11 2017. accessed: 2025-11-14.

[85] Smartech Online. What is the temperature range of silicone rubber?, 2024. URL https://shorturl.at/zDK6A. Accessed: 2025-10-15.

[86] Ken Oota and Masumi Saka. Cure shrinkage analysis of epoxy molding compound. *Polymer Engineering & Science*, 41(8):1373–1379, 2001. URL https://doi.org/10.1002/pen.10837.

[87] D Ouis. On the frequency dependence of the modulus of elasticity of wood. *Wood science and technology*, 36(4):335–346, 2002. URL https://doi.org/10.1007/s00226-002-0145-5.

[88] Ha Q. Pham and Maurice J. Marks. Epoxy resins. In *Encyclopedia of Polymer Science and Technology*, volume 9, pages 454–573. John Wiley & Sons, Inc., 2004. URL https://doi.org/10.1002/0471440264.pst119.

[89] Findel International PLC. Field's metal smart material, 1.3 ml, 2025. URL https://shorturl.at/a82u8. Accessed: 2025-15-10.

[90] Yuriy Plevachuk, Vasyl Sklyarchuk, Sven Eckert, Gunter Gerbeth, and Rada Novakovic. Thermophysical properties of the liquid ga-in-sn eutectic alloy. *Journal of Chemical & Engineering Data*, 59(3):757–763, 2014. URL https://doi.org/10.1021/je400882q.

[91] Yuqing Qiao. Effect of wing flexibility on aircraft flight dynamics. Master's thesis, Cranfield University, 2012. URL http://dspace.lib.cranfield.ac.uk/handle/1826/7280.

[92] Gulfam Raza, Saqib Iqbal, and Abdul Samad Farooq. Paraffin wax-based thermal composites. *Paraffin: thermal energy storage applications*, 19, 2022. URL https://doi.org/10.5772/intechopen.97195.

[93] *silicone rubber VTN6001*. Renishaw, 2013. URL https://shorturl.at/sw8wc. Accessed: 2025-9-16.

[94] Pieter Samyn and Vibhore K Rastogi. Stabilization of an aqueous bio-based wax nanoemulsion through encapsulation. *Nanomaterials*, 12(23):4329, 2022. URL https://doi.org/10.3390/nano12234329.

[95] Jurnan Schilder. Mechanical vibrations, 04 2021.

[96] Tony L Schmitz and K. Scott Smith. *Measurement Techniques*, pages 255–282. Springer International, 2021. URL https://doi.org/10.1007/978-3-030-52344-2_7.

[97] Atul Sharma, V Veer Tyagi, Carl R Chen, and Dharam Buddhi. Review on thermal energy storage with phase change materials and applications. *Renewable and Sustainable energy reviews*, 13(2):318–345, 2009. URL https://doi.org/10.1016/j.rser.2007.10.005.

[98] Yingli Shi, Min Hu, Yufeng Xing, and Yuhang Li. Temperature-dependent thermal and mechanical properties of flexible functional pdms/paraffin composites. *Materials & Design*, 185, 2020. URL https://doi.org/10.1016/j.matdes.2019.108219.

[99] Shin-Etsu Chemical Co., Ltd. Thermal interface silicone rubber, 2024. URL https://www.shinetsusilicone-global.com/products/type/heat_rubb/index.shtml. Accessed: 2025-10-15.

[100] Silpak. Silpak ru-320 flexible polyurethane rubber — technical data sheet, 2025. URL https://silpak.com/content/pdf/Silpak_RU-320-25A_FlexiblePolyurethane_TDB.pdf. Accessed: 2025-10-16.

[101] Inc. Smooth-On. Dragon skin series, addition cure silicone rubber compounds, 2014. URL https://www.smooth-on.com/tb/files/DRAGON_SKIN_SERIES_TB.pdf. Accessed: 2025-10-11.

[102] Inc. Smooth-On. Mold max 14nv and 29nv: Tin-catalyzed silicone rubber compounds – technical bulletin, 2024. URL https://www.smooth-on.com/tb/files/MOLD_MAX_14NV_29NV_TB.pdf. Accessed: 2025-11-10.

[103] N Soares, T Matias, L Durães, PN Simões, and JJ Costa. Thermophysical characterization of paraffin-based pcms for low temperature thermal energy storage applications for buildings. *Energy*, 269:126745, 2023. URL https://doi.org/10.1016/j.energy.2023.126745.

[104] ME Sotomayor, I Krupa, A Varez, and B Levenfeld. Thermal and mechanical characterization of injection moulded high density polyethylene/paraffin wax blends as phase change materials. *Renewable Energy*, 68:140–145, 2014. URL https://doi.org/10.1016/j.renene.2014.01.036.

[105] Steal88. Concorde – airframe temperatures during mach 2 flight. Wikimedia Commons image file, 2010. URL https://shorturl.at/JNwfH. Registered under Creative Commons BY-SA 4.0 licence.

[106] Giacomo Struzziero, Berenice Remy, and Alexandros A Skordos. Measurement of thermal conductivity of epoxy resins during cure. *Journal of Applied Polymer Science*, 136(5):47015, 2019. URL https://doi.org/10.1002/app.47015.

[107] Sybridge. Five design tips for urethane casted parts, 2023. URL https://sybridge.com/five-design-tips-for-urethane-casted-parts/. Accessed: 2025-10-15.

[108] Istven Szergenyi. A method for determining the coefficient of volume thermal expansion of petroleum paraffins. *Periodica Polytechnica Chemical Engineering*, 18(3):217–227, 1974. URL https://shorturl.at/kUtVL.

[109] The Engineering ToolBox. Thermal conductivity of common materials - solids, liquids and gases, 2003. URL https://www.engineeringtoolbox.com/thermal-conductivity-d_429.html. Accessed: 2025-19-6.

[110] The Engineering ToolBox. Solids - volume temperature expansion coefficients, 2014. URL https://www.engineeringtoolbox.com/volum-expansion-coefficients-solids-d_1894.html. Accessed: 2025-09-15.

[111] Neven Ukrainczyk, Stanislav Kurajica, and Juraj Sipusic. Thermophysical comparison of five commercial paraffin waxes as latent heat storage materials. *Chemical and biochemical engineering quarterly*, 24(2):129–137, 2010. URL https://hrcak.srce.hr/en/55015.

[112] Kinga Uram et al. Thermal stability and heat transfer of polyurethanes for mining applications, 2022. URL https://doi.org/10.3390/molecules29143337.

[113] Saul Utrera-Barrios, Liyun Yu, and Anne Ladegaard Skov. Revisiting the thermal transitions of polydimethylsiloxane (pdms) elastomers: Addressing common misconceptions with comprehensive data. *Macromolecular Materials and Engineering*, page 2500075, 2025. URL https://doi.org/10.1002/mame.202500075.

[114] Amir Reza Vakhshouri. Paraffin as phase change material. In Fathi Samir Soliman, editor, *Paraffin - an Overview*, chapter 5. IntechOpen, London, 2019. URL https://doi.org/10.5772/intechopen.90487.

[115] H Vinson. What is silicone rubber? properties, applications, and benefits explained, 4 2025. URL https://www.kinsoe.com/silicone-rubber-properties-applications/. Acccessed: 2025-11-27.

[116] David Walsh and Paul Zoller. *Standard pressure volume temperature data for polymers*. CRC press, 1995. URL https://doi.org/10.1002/pola.1996.827.

[117] Yu Yampolskii. *Fractional Free Volume (FFV)*, pages 818–819. Encyclopedia of Membranes, 01 2016. URL https://doi.org/10.1007/978-3-662-44324-8_243.

[118] XK Yu and YB Tao. Preparation and characterization of paraffin/expanded graphite composite phase change materials with high thermal conductivity. *International Journal of Heat and Mass Transfer*, 198:123433, 2022. URL https://doi.org/10.1016/j.ijheatmasstransfer.2022.123433.

[119] Ping Zhang, Yuan Hu, Lei Song, Jianxiong Ni, Weiyi Xing, and Jian Wang. Effect of expanded graphite on properties of high-density polyethylene/paraffin composite with intumescent flame retardant as a shape-stabilized phase change material. *Solar Energy Materials and Solar Cells*, 94(2):360–365, 2010. URL https://doi.org/10.1016/j.solmat.2009.10.014.

[120] Thomas J Zolper, Manfred Jungk, Tobin J Marks, Yip-Wah Chung, and Qian Wang. Modeling polysiloxane volume and viscosity variations with molecular structure and thermodynamic state. *Journal of Tribology*, 136(1), 2014. URL https://doi.org/10.1115/1.4025301.

A | Appendix

A.1 DMA data

This Section covers the additional data of the samples S1 until S4.

A.1.1 Sample S1

This section covers the additional plots from the DMA test of sample S1. Shown is in Figure A.1a the relationship between frequency and storage modulus for different temperatures. Figure A.1b shows the relationship between the frequency and loss factor. The master curves using the CFS of all the viscoelastic properties are shown in Figure A.2. Lastly, the invariant for different reference temperatures of the WLF and Arrhenius model are shown in table A.1

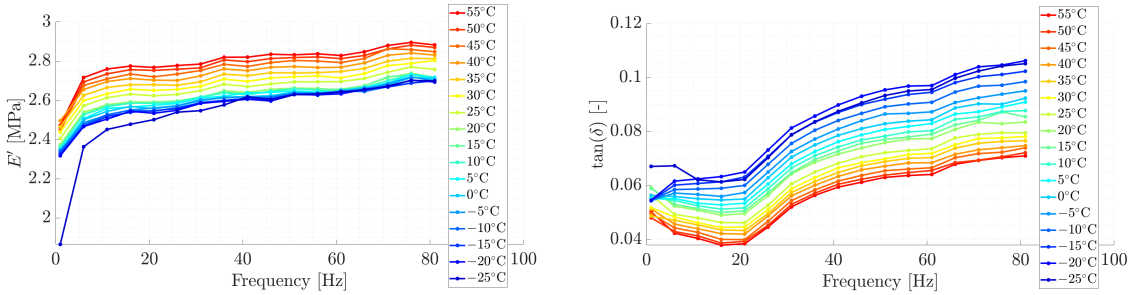

(a) *Frequency–storage modulus curve for sample S1*

(b) *Frequency–loss factor curve for sample S1*

Figure A.1: *Frequency-dependent viscoelastic properties of sample S1*

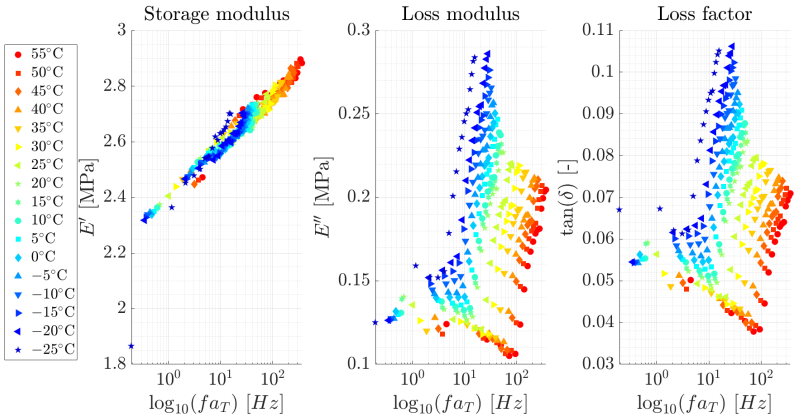

Figure A.2: *The master curves of the viscoelastic properties of sample S1 using the CFS method*

Table A.1: *Overview of WLF and Arrhenius parameters for different reference temperatures for the S1 sample composition*

T_{ref} [°C]	C_1C_2 [K]	R^2_{WLF} [-]	$\mathbf{STD}_{\mathrm{WLF}}$ [-]	E_a [kJ/mol]	R^2_{Arr} [-]	$\mathbf{STD}_{\mathrm{Arr}}$ [-]
55	-3.6201×10^{29}	-0.24158	0.07002	-1.5877	-0.27858	0.066442
50	-2.9662×10^{28}	-0.0039673	0.054868	-1.3809	-0.019928	0.052921
45	-1.1191×10^{29}	0.14709	0.071524	-1.7183	0.12535	0.070123
40	-7.9243×10^{29}	0.26296	0.073947	-1.8851	0.23809	0.071009
35	-8.0908×10^{29}	0.15125	0.11280	-2.3291	0.12043	0.094751
30	-1.3185×10^{31}	0.060847	0.16075	-3.5757	0.011148	0.12032
25	-9.0828×10^{30}	0.058658	0.20205	-6.0126	-0.027941	0.12901
20	-7.7295×10^{31}	0.081907	0.30024	-11.591	-0.041407	0.17264
15	-5.0214×10^{31}	0.32241	0.26897	-15.517	0.17537	0.16508
10	-1.6726×10^{33}	0.44054	0.28649	-17.569	0.34165	0.25946
5	-4.0681×10^{32}	0.67951	0.19856	-21.092	0.57123	0.17432
0	-2.1719×10^{32}	0.79142	0.16890	-22.816	0.71808	0.16823
-5	-6.9015×10^{31}	0.84389	0.14829	-21.923	0.79895	0.15934
-10	-3.2108×10^{32}	0.87104	0.13701	-20.820	0.83835	0.14851
-15	-1.5453×10^{32}	0.85763	0.14571	-18.899	0.82397	0.15405
-20	-2.3305×10^{32}	0.83762	0.15684	-17.037	0.79743	0.16279
-25	-3.9096×10^{2}	0.94033	0.10068	-25.299	0.93251	0.10290

A.1.2 Sample S2

This section covers the additional plots from the DMA test of sample S2. Shown is in Figure A.3a the relationship between frequency and storage modulus for different temperatures. Figure A.3b shows the relationship between the frequency and loss factor. The master curves using the CFS of all the viscoelastic properties are shown in Figure A.4. Lastly, the invariant for different reference temperatures of the WLF and Arrhenius model were already shown in the results section in figure 5.5

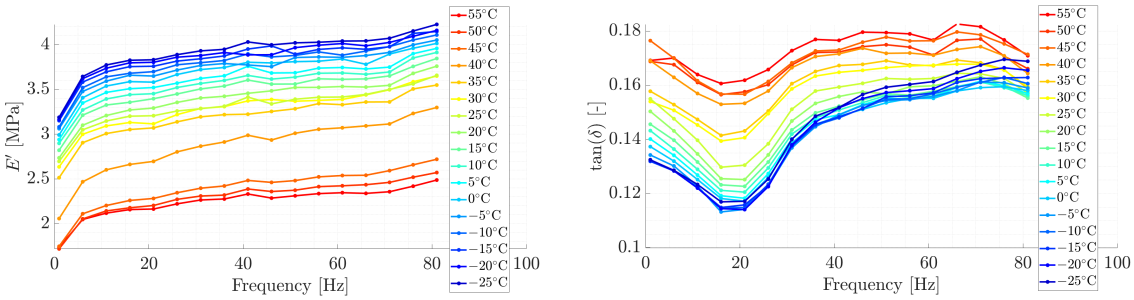

(a) *Frequency–storage modulus curve for sample S2*

(b) *Frequency–loss factor curve for sample S2*

Figure A.3: *Frequency-dependent viscoelastic properties of sample S2*

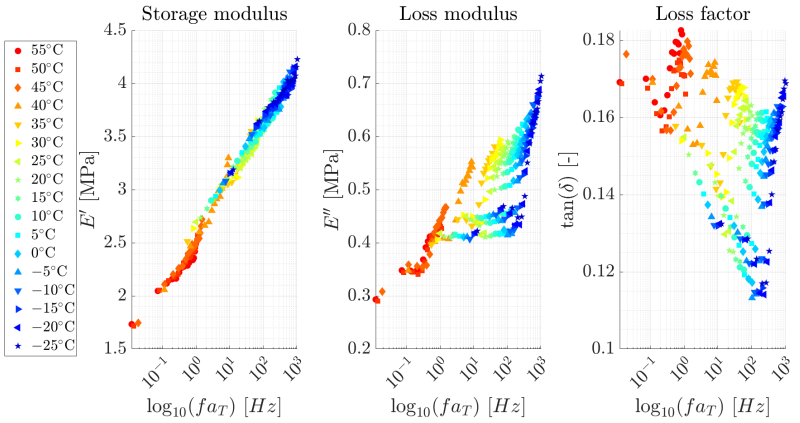

Figure A.4: *The master curves of the viscoelastic properties of sample S2 using the CFS method*

A.1.3 Sample S3

This section covers the additional plots from the DMA test of sample S3. Shown is in Figure A.5a the relationship between frequency and storage modulus for different temperatures. Figure A.5b shows the relationship between the frequency and loss factor. The master curves using the CFS of all the viscoelastic properties are shown in Figure A.6. Lastly, the invariant for different reference temperatures of the WLF and Arrhenius model were already shown in the results section in figure A.2

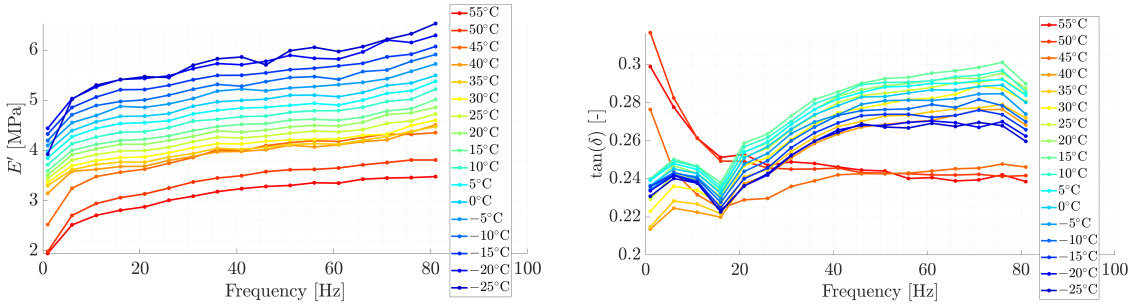

(a) *Frequency–storage modulus curve for sample S3*

(b) *Frequency–loss factor curve for sample S3*

Figure A.5: *Frequency-dependent viscoelastic properties of sample S3*

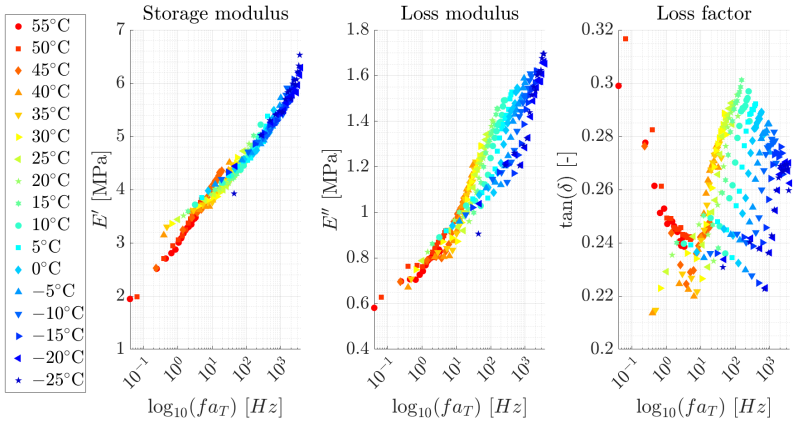

Figure A.6: *The master curves of the viscoelastic properties of sample S3 using the CFS method*

Table A.2: *Overview of WLF and Arrhenius fit parameters as a function of reference temperature for the RMS method for the S3 sample*

$T_{\mathbf{ref}}$ [°C]	C_1C_2 [-]	$R^2_{\mathbf{WLF}}$ [-]	$\mathbf{STD_{WLF}}$ [-]	E_a [kJ/mol]	$R^2_{\mathbf{Arr}}$ [-]	$\mathbf{STD_{Arr}}$ [-]
55	1.78×10^{33}	0.29395	0.77675	69.731	0.08106	0.79374
50	1.87×10^{33}	0.53246	0.60221	65.114	0.38240	0.61397
45	1.60×10^{31}	0.90325	0.26288	48.079	0.88257	0.28034
40	1.95×10^{31}	0.89633	0.27731	50.927	0.88043	0.28584
35	27520	0.87056	0.30657	52.638	0.86544	0.28934
30	1702.1	0.84036	0.32138	51.369	0.83951	0.27615
25	479.08	0.82208	0.31361	47.369	0.79902	0.26223
20	416.74	0.76846	0.38506	45.388	0.74447	0.35814
15	202.03	0.74486	0.37161	39.940	0.67876	0.33911
10	114.24	0.72006	0.34463	31.925	0.61409	0.32304
5	68.436	0.67942	0.32254	24.319	0.54896	0.31433
0	44.804	0.61771	0.31402	18.708	0.49238	0.31067
-5	16.534	0.68870	0.17464	10.457	0.49053	0.19002
-10	11.316	0.60848	0.16182	8.4433	0.49270	0.16951
-15	25.946	0.39780	0.18121	7.4919	0.39136	0.17540
-20	516.41	0.21862	0.21494	7.2149	0.21857	0.20808
-25	2.2742	0.05921	0.32689	7.3091	0.00234	0.32452

A.1.4 Sample S4

This section covers the additional plots from the DMA test of sample S4. Shown is in Figure A.7a the relationship between frequency and storage modulus for different temperatures. Figure A.7b shows the relationship between the frequency and loss factor. The master curves using the CFS of all the viscoelastic properties are shown in Figure A.8. Lastly, the invariant for different reference temperatures of the WLF and Arrhenius model were already shown in the results section in figure A.3

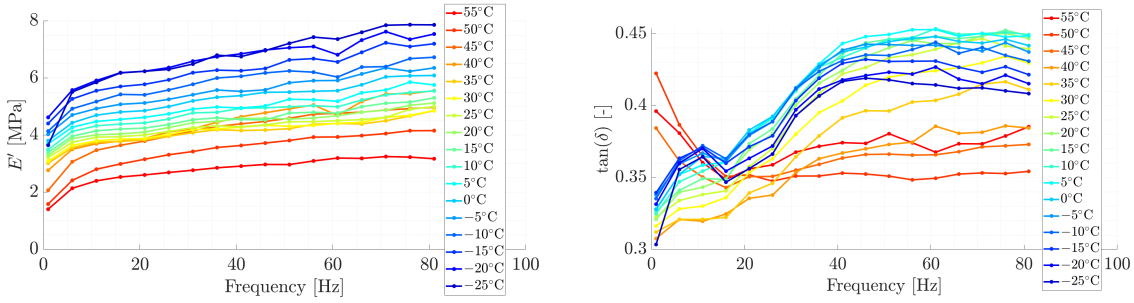

(a) *Frequency–storage modulus curve for sample S4*

(b) *Frequency–loss factor curve for sample S4*

Figure A.7: *Frequency-dependent viscoelastic properties of sample S4*

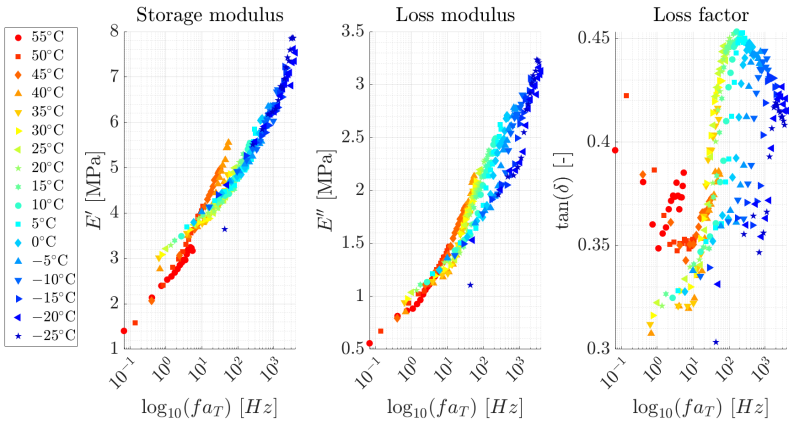

Figure A.8: *The master curves of the viscoelastic properties of sample S4 using the CFS method*

Table A.3: *Overview of WLF and Arrhenius parameters for different reference temperatures for the S4 sample*

T_{ref} [°C]	C_1C_2 [K]	R^2_{WLF} [-]	STD_{WLF} [-]	E_a [kJ/mol]	R^2_{Arr} [-]	STD_{Arr} [-]
55	1.2553×10^{33}	0.35637	0.71999	68.609	0.15963	0.73550
50	1.3138×10^{32}	0.74576	0.39608	53.921	0.65627	0.41898
45	709.34	0.84751	0.27374	34.762	0.84466	0.26108
40	185.83	0.81999	0.26374	28.850	0.79756	0.25757
35	2533.8	0.83138	0.29168	42.884	0.83135	0.27348
30	818.52	0.79260	0.31462	43.643	0.78690	0.27701
25	423.93	0.76682	0.33745	43.166	0.74318	0.29486
20	524.52	0.71282	0.42538	43.044	0.70015	0.39920
15	231.20	0.68464	0.41779	39.049	0.63723	0.37881
10	117.66	0.67211	0.37596	31.407	0.58128	0.34587
5	37.744	0.71572	0.24997	19.654	0.42188	0.22320
0	25.801	0.70715	0.21303	14.329	0.46532	0.21683
-5	18.839	0.64174	0.20566	11.374	0.48275	0.21008
-10	15.055	0.49964	0.22096	9.6633	0.44584	0.21552
-15	5.3309×10^{25}	0.29609	0.24267	8.4705	0.29521	0.23473
-20	1.7977×10^{30}	0.27694	0.22639	7.3503	0.26182	0.22128
-25	9.4378×10^{29}	0.26234	0.22123	6.3831	0.24442	0.21641

A.2 Linear viscoelastic regime

Table A.4 shows the settings of the DMA for the LVE test. Two tests were performed to identify the LVE region. In the first test the dynamic strain up to 5 % was tested, the results are shown in Figure A.9a. For the second test the machine was not able to perform a dynamic strain upto 9 % and stagnated at about 5 % dynamic strain as can be seen in Figure A.9b.

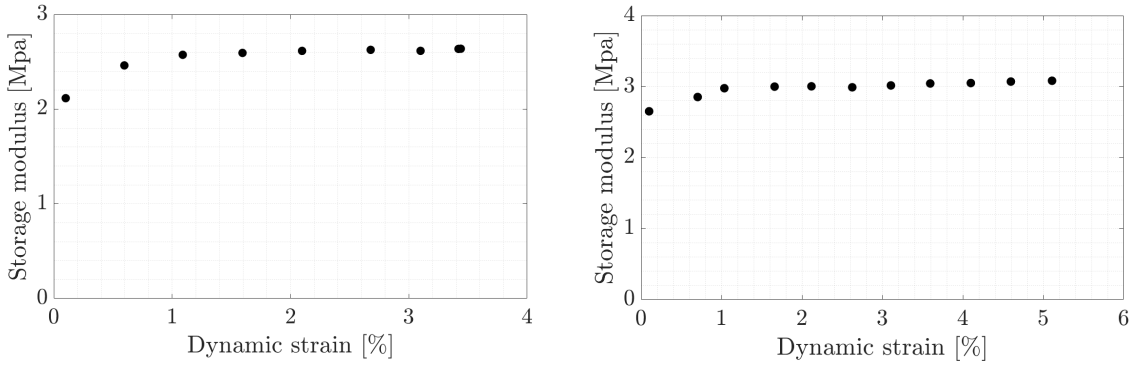

(a) *First test results of the LVE region*

(b) *Second test results of the LVE region*

Figure A.9: *Overview of the two LVE region tests*

Parameter	**Test 1**	**Test 2**
Static load (strain)	5.00 %	10.00 %
Dynamic load range (strain)	0.10 - 4.00 %	0.10 - 9.00 %
Dynamic increment	0.50 %	0.5 %
Contact force	0.50 N	0.50 N
Temperature	25.0 °C	25.0 °C
Soak time	300 s	300 s
Frequency	1.0 Hz	1.0 Hz
Limits (static load)	30 N	30 N
Limits (dynamic load)	20 N	20 N

Table A.4: *Overview of DMA test settings for the two LVE tests*

A.3 Eigenfrequency of beams

The eigenfrequency of a beam in 2D can be determined analytically under the following assumptions

- The beam is a slender member ($L > 10w$)
- The beam is only subjected to bending loads
- The beam is prismatic
- The beam is symmetric
- The beam is homogeneous

Without any further derivation the EOM of a beam is shown in Equation A.1 [95], where it is assumed that there are no external forces applied, because the free vibration response is of interest.

$$\rho A \frac{\partial^2 v}{\partial t^2} + EI \frac{\partial^4 v}{\partial x^4} = 0 \tag{A.1}$$

Next, this homogeneous partial differential equation can be solved using the separation of variables technique. This technique assumes that the solution for the displacement field can be written as a multiplication of a functions only depending on x and t, Equation A.2.

$$v(x,t) = V(x)T(t) \tag{A.2}$$

Upon substitution of Equation A.2 into Equation A.1 and rewriting results in Equation A.3. It is observed that the LHS is a function of T only and the RMSE an function of x only and they are equal. This implies both must be equal to the same constant, called the separation constant. It was found, that it is convenient to use $-\omega^2$ [95].

$$\frac{1}{T}\frac{d^2T}{dt^2} = \frac{EI}{\rho A}\frac{1}{V}\frac{d^4V}{dx^4} = -\omega^2 \tag{A.3}$$

The equations for $T(t)$ and $V(x)$ can be solved separately. The goal is to find the eigenfrequency of the beam which is related to the displacement, therefore, only the solution of the RHS of Equation A.3 is considered. Upon rewriting, the wave number β is introduced in Equation A.4.

$$\beta = \sqrt[4]{\frac{\rho A \omega^2}{EI}} \tag{A.4}$$

When β is substituted in Equation A.3 a fourth order linear differential equation is obtained, as shown in equation A.5.

$$\frac{d^4V}{dx^4} + \frac{\rho A \omega^2}{EI} V = 0 \rightarrow \frac{d^4V}{dx^4} + \beta^4 V = 0 \tag{A.5}$$

The solution to this differential equation can be written as a combination of (hyperbolic) sine and cosines, as shown in Equation A.6.

$$V(x) = c_1 cos(\beta x) + c_2 sin(\beta x) + c_3 cosh(\beta x) + c_4 sinh(\beta x) \tag{A.6}$$

The exact solution to determine the coefficients c_1 to c_4 are dependent on the applied boundary conditions. There are four unknowns, so there are four boundary conditions needed. In the case of a free-free beam those are the curvature and the change of curvature are 0 at the start and end of the beam. Substituting these boundary conditions in Equation A.6 yields a linear set of equations, these can be put in matrix vector format. To solve the linear set, it is assumed that the determinant of that matrix is zero. This yields the characteristic equation shown in Equation A.7.

$$cosh(\beta_n L)\, cos(\beta_n L) - 1 = 0 \tag{A.7}$$

This equation can not be solved analytically, therefore, the numerical solution for $\beta_n L$ is shown. For n is 1, 2 and 3, $\beta_n L$ is 4.730, 7.853, 10.995. These numbers can substituted in Equation A.8 to find the eigenfrequencies of the first three bending modes. This expression can be interpreted as a measure for the bending stiffness ($\frac{EI}{L^3}$) over a mass term (ρA) [95]. Therefore, this expression is equivalent to $\sqrt{\frac{k}{m}}$ as shown in Section 3.2.

$$\omega_n = (\beta_n L)^2 \sqrt{\frac{EI}{\rho A L^4}} = (\beta_n L)^2 \sqrt{\frac{EI}{mL^3}} \tag{A.8}$$

Equation A.8 is derived for a homogeneous beam, which assumes uniform stiffness, inertia and density. However, the scope of the research covers SSPCMs which consists of multiple materials. To obtain one uniform value for the stiffness and second moment of area, the rule of mixtures is applied. This approach assumes that the effective property of the SSPCMs can be expressed as a weighted combination of the properties of the individual constituents based on their volume (or mass) fractions. For the eigenfrequency calculation, the contributions of the carbon fibre shell and the SSPCM core are combined linearly, resulting in one effective stiffness and inertia, as defined in Equation A.9. The required input parameters are given in Table A.5a.

$$EI = E_{CF} I_{CF} + E_{SSPCM} I_{SSPCM} \tag{A.9}$$

The total mass is obtained directly by weighing each beam and the effective length used in the analytical model is 0.60 m. Substituting these values into Equation A.8 yields the first two eigenfrequencies, listed in Table A.5b. These analytical predictions are used both to define the relevant frequency range for testing and to serve as a reference for comparison with the experimental results.

Material	**E [MPa]**	**I [m^4]**
Carbon fibre	84.1E3 [33]	2.84E-8
Silicone rubber	3.38 [102]	3.67E-8
Paraffin wax	55.7 [48]	3.67E-8

(a) *Material properties*

Sample	**si/wax [%]**	**Mass [kg]**	ω_1 **[Hz]**	ω_2 **[Hz]**
Beam 1	100/0	1.024	370	1020
Beam 2	85/15	0.978	379	1044
Beam 3	80/20	0.570	495	1365

(b) *Beam compositions and eigenfrequencies*

Table A.5: *Overview of material and beam properties*

A.4 Specimen dimensions

The information below specifies the dimensions and requirements for each compression, tensile and 3-point bending test for the Netzsch Eplexor 2000.
Typical compression sample dimensions

- Diameter: 10 mm ($\pm$0.1 mm)
- Thickness: 4 mm ($\pm$0.2 mm)
- Surface: Must be flat and parallel
- Material: Typically disk-shaped; suitable for rubber, elastomers, or plastics

Typical tensile sample dimensions

- Length: min 50 mm (generally 100 mm is used)
- Width: 5 mm
- Thickness: 1-2 mm (depends on material type)
- Shape: Rectangular strip or mini dog-bone, with flat ends
- Surface: Smooth and flat to ensure good clamping
- Material: Suitable for films, plastics, rubbers, elastomers

Typical 3-point bending sample dimensions

- Length: 55 mm
- Width: 10 mm
- Thickness: 3 mm
- Support Span: 40 mm (set on instrument)

A.5 TMA

Initially measuring the linear CTE using a TMA machine, was also part of the research. However, only one set of measurement could be performed of the S1 sample, because the TMA machine was broken. The section below will briefly highlight the analysis technique and will show the results for this sample.

A.5.1 Data analysis

The TMA machine used is the Linesis TMA PT 1600, which has a working temperature of up to 1600 °C and a resolution of 0.125 nm. To find the CTE first the initial length at room temperature is measured next the samples are exposed to to a specific temperature cycle as shown in Figure A.10. First the temperature is cooled with a rate of 2 $°C\ /min$ to -20 °C and dwelled for 20 minutes. Then, the sample is heated with 2 $°C\ /min$ to 70 °C and dwelled for 10 minutes. Next the temple is reduced to -20 °C and the cycle is repeated. The second cycle is present to remove the shape memory effect.

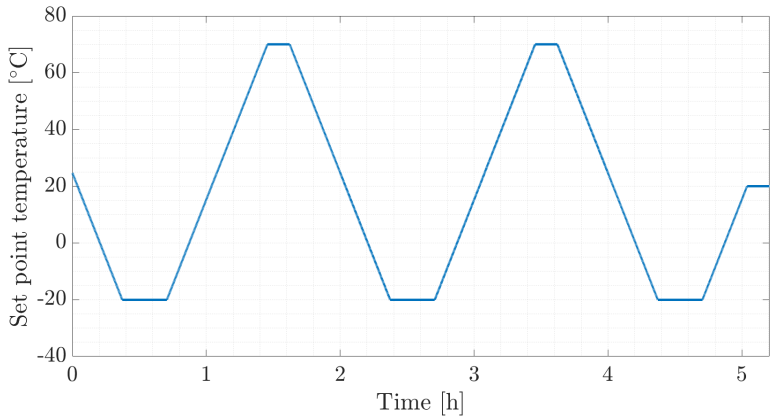

Figure A.10: *Heating cycle of the samples in the TMA machine*

The CTE is determined using the ISO 11359-2 standard, which defines Equation A.10 to calculate the CTE [53]. The initial length of the specimen is represented by L_0. Physically, the CTE is interpreted as the slope of the elongation-temperature graph ($\frac{dL}{dT}$). However, calculating this slope via differentiation introduces additional noise into the measurements. To mitigate this issue, it is suggested to use regression analysis for the length of the specimen plotted against temperature. Next a fit can be found according to equation A.11, where the CTE is dependent on the temperature [40].

$$\alpha = \frac{dL}{dT} \times \frac{1}{L_0} \tag{A.10}$$

$$L(T) = \alpha(T) * T + L \tag{A.11}$$

A.5.2 Results

The same sample has been measured five times under the exact same conditions. The results of the shrinkage curve of one measurement is shown on the left of Figure A.11. The graph starts at the initial length at 10.112 mm, it undergoes the heating cycle described above. There are 2 heating and 2 cooling cycles so the shrinkage curves goes back and forth 4 times. The graph on the right in Figure A.11 shows the cropped version which only uses the second cycle and cuts the data at 15 and 60 °C. The linear fit is shown in orange, which results in a CTE that is constant over temperature. The result of these fits are shown in Table A.6. In the first columns it shows the equation for the length of each measurement, the second column the CTE and in the last column

the R^2 value for each fit. The last row shows the average of all the measurements. It can be seen that the data for the CTE relatively consistent is averaging at a value around 324 ppm/K, corresponding to a very good fit of 0.95. This corresponds with literature as the value found were in the range of 200 to 400 ppm/K.

The same sample was measured five times under identical conditions. The shrinkage curve of one representative measurement is shown on the left side of Figure A.11. The graph begins at the initial length of 10.112 mm and follows the heating cycle described above. Because the procedure contains two heating and two cooling segments, the shrinkage curve goed back and forth four complete cycles. The right side of Figure A.11 presents the cropped dataset, which isolates the second cycle and only keeps the temperature range from 15 to 60 °C.

The linear fit, shown in orange, yields a constant CTE over the selected temperature interval. The results of all five fits are summarised in Table A.6. The first column lists the fitted length–temperature relations, the second column reports the corresponding CTE values and the final column provides the associated R^2 values. The last row shows the mean of all measurements. The CTE values are relatively consistent, averaging around 324 ppm/K, with an average goodness of fit of approximately 0.95. These values align well with literature, where reported CTEs for similar materials range from 200 to 400 ppm/K.

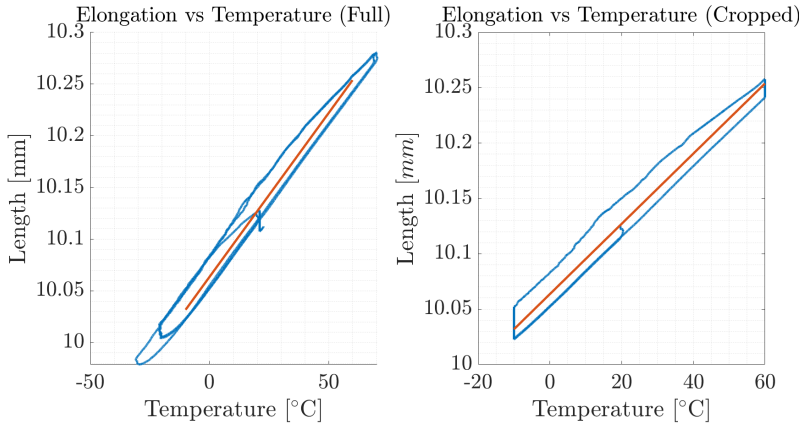

Figure A.11: *The length-temperature curve for sample S1*

Measurement	Fit	CTE [ppm/K]	CoD (R^2-value)
1	$L_1 = 3.1566 \times 10^{-3} * T + 10.1234$	311.5438	0.95282
2	$L_2 = 3.1730 \times 10^{-3} * T + 10.0635$	313.7842	0.94539
3	$L_3 = 3.2442 \times 10^{-3} * T + 10.1172$	320.6409	0.96488
4	$L_4 = 3.3498 \times 10^{-3} * T + 10.1853$	330.8739	0.95357
5	$L_5 = 3.5311 \times 10^{-3} * T + 10.2530$	346.1555	0.94091
Mean	$L_{\text{mean}} = 3.290\,94 \times 10^{-3} * T + 10.14848$	324.1997	0.95111

Table A.6: *Regression analysis for thermal expansion measurements of sample S1*